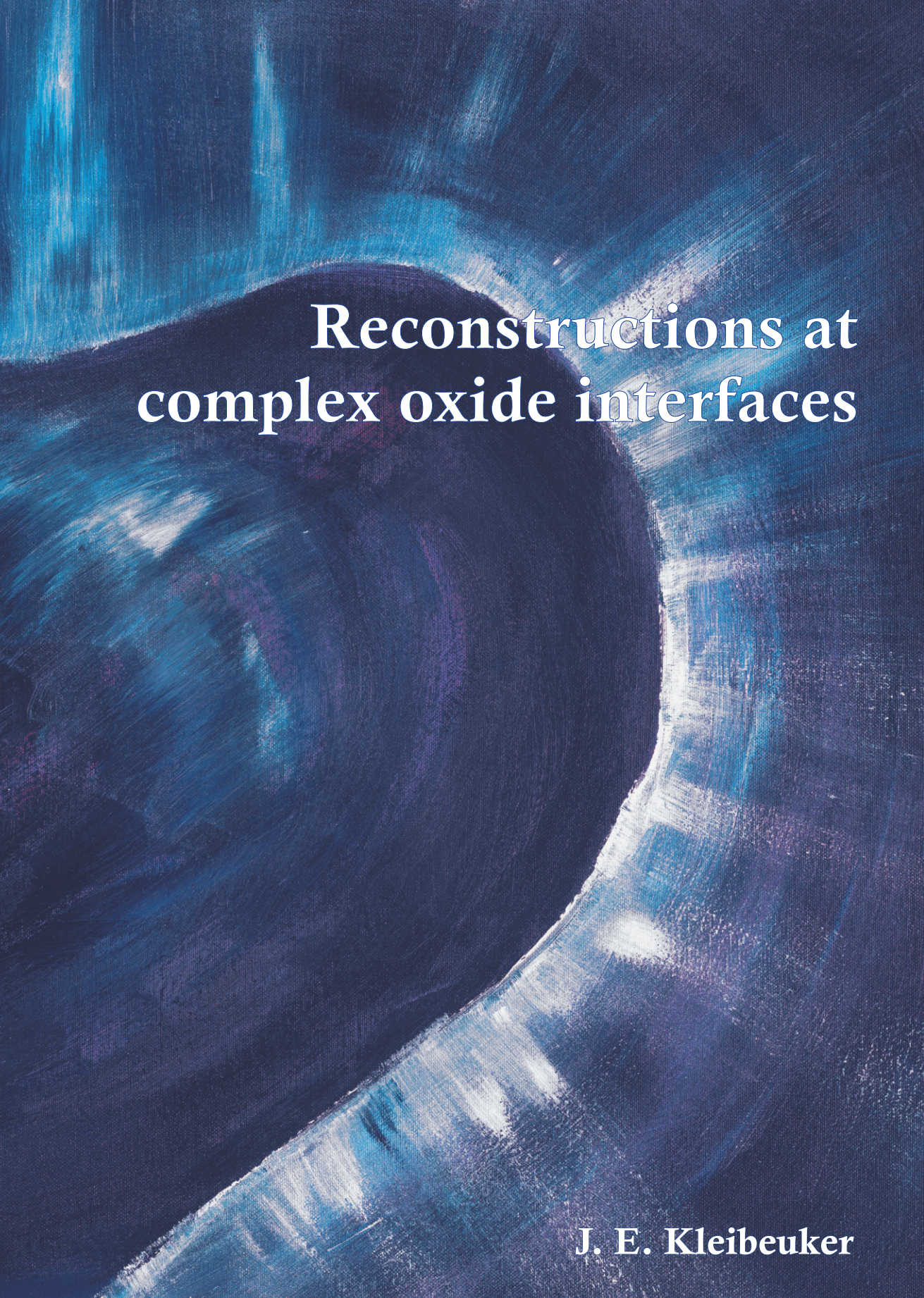
Reconstructions at complex oxide interfaces
J. E. Kleibeuker

Reconstructions at Complex Oxide Interfaces

by

Josée Elisabeth Kleibeuker

Cover
The cover is an artist impression of the research presented in this thesis. The painting is made by M. Vos.

Ph.D. Committee

Chairman and Secretary

Prof. dr. G. van der Steenhoven (University of Twente, The Netherlands)

Promotor

Prof. dr. ing. A. J. H. M. Rijnders (University of Twente, The Netherlands)
Prof. dr. ing. D. H. A. Blank (University of Twente, The Netherlands)

Assistent-promotor

Dr. ir. G. Koster (University of Twente, The Netherlands)

Members

Prof. dr. ir. A. Brinkman (University of Twente, The Netherlands)

Prof. dr. R. Claessen (University of Würzburg, Germany)

Prof. dr. P. J. Kelly (University of Twente, The Netherlands)

Prof. dr. T. T. M. Palstra (University of Groningen, The Netherlands)

Dr. N. Pryds (Risø National Laboratory for Sustainable Energy, Denmark)

The research presented in this thesis was carried out within the Inorganic Materials Science group, Department of Science and Technology, MESA$^+$ Institute of Nanotechnology at the University of Twente, The Netherlands, and within the Experimental Physics 4 group at the University of Würzburg, Germany. The research was financially supported by The Netherlands Organization for Scientific Research (NWO).

Ph.D. thesis, Univeristy of Twente, Enschede, The Netherlands

ISBN: 978-90-365-3320-1
Printed by Wöhrmann Print Service, Zutphen, The Netherlands

Reconstructions at Complex Oxide Interfaces

Proefschrift

ter verkrijging van
de graad van doctor aan de Universiteit Twente,
op gezag van de rector magnificus,
Prof. dr. H. Brinksma,
volgens besluit van het College voor Promoties
in het openbaar te verdedigen
op vrijdag 23 maart 2012 om 16.45 uur

door

Josée Elisabeth Kleibeuker

geboren op 29 augustus 1984
te Groningen

Dit proefschrift is goedgekeurd door de promotoren

Prof. dr. ing. A. J. H. M. Rijnders
Prof. dr. ing. D. H. A. Blank

en de assistent-promotor

Dr. ir. G. Koster

Contents

Chapter 1

Reconstructions at Complex Oxide Interfaces

1.1 Introduction

"*The ages of civilization are designated by reference to a prominent material that could be fashioned by the prevailing state of technology. For example the Stone Age, the Bronze Age and the Iron Age. Now we are at the threshold of an age in which materials can be fashioned atom by atom.*" Eddie Bernice Johnson, member of US House of Representatives, was referring to the evolution of nanoscience and nanotechnology.[1] The idea of nanotechnology goes back to 1959, when Feynman gave a talk during a meeting of the American Physical Society, entitled *There's plenty of room at the bottom.*[2] During his talk, he described how direct manipulation of individual atoms may be accomplished. However, it took thirty years before his vision was realized. Scientists of IBM spelled out the name of their company by using single xenon atoms on a nickel surface.[3]

In nanotechnology, matter is manipulated at the atomic or molecular level. As a result, materials with fundamental new atomic arrangements and functionalities can be fabricated. Nature already shows that the arrangement of atoms is crucial for the properties of the material. To give an example, diamond and graphite, both natural materials, consist solely of carbon atoms, but have different physical properties. Diamond has a three dimensional C-C network and is optically transparent, hard and electronically insulating, while graphite has a two dimensional C-C network and is black, brittle and an electrical conductor.

Nanotechnology is a very diverse field of research, ranging from device physics to molecular biology. In this thesis, the focus is on the manipulation of condensed matter at an atomic level. With the high interest in epitaxial heterostructures, development of thin film deposition techniques, such as pulsed laser deposition, reached the fabrication of materials with atomic precision. Epitaxial heterostructures consist of a crystalline substrate with at least one structurally ordered film of another material on top. The perfect control of the creation of new crystalline

materials resulted in the discovery of new, sometimes unexpected, properties.

An interesting example is the behavior of $LaFeO_3$-$LaCrO_3$ superlattices. Both materials are G-type antiferromagnets, but ferromagnetic order was predicted in the combined material as a result of superexchange interaction between Fe^{3+}-O-Cr^{3+}.[4] Experimentally, random positioning of Fe^{3+} and Cr^{3+} ions had frustrated the observation of ferromagnetic properties. To achieve an ordered Cr-Fe mixture, Ueda *et al.* fabricated [1×1] $LaFeO_3$-$LaCrO_3$ superlattices along the [111] direction.[5] As a result, Fe and Cr were alternately ordered along the [001] and [100] directions at an atomic level. Due to this precise arrangement of Cr and Fe atoms, ferromagnetic order in these superlattices was achieved, as predicted.

$LaFeO_3$ and $LaCrO_3$ are both perovskite-type oxides. This class of materials is very suitable for the study of epitaxial heterostructures.[6] The wide variety of cations results in a rich spectrum of physical properties, among others, ferromagnetism, superconductivity and ferroelectricity. On the other hand, their similar oxygen backbone structure and lattice parameters allow stacking of crystalline perovskite-type oxides with atomic precision.

In perovskite-type oxide heterostructures, the properties of the materials can be manipulated in several ways. First of all, the thin film has a lower dimensionality than the bulk material. Therefore, surface and interface effects may have a clear influence on the behavior of the material. To give an example, bulk $SrRuO_3$ is a ferromagnetic bad metal, but a three unit cell thin $SrRuO_3$ film on $SrTiO_3$ is insulating.[7] Secondly, the unit cell structure of a perovskite-type oxide can be deformed by epitaxial growth. For instance, $SrTiO_3$ is paraelectric in bulk, but a $SrTiO_3$ film can become ferroelectric by inducing biaxial strain, even at room temperature.[8] Furthermore, interplay between different materials can enhance their properties or induce new functionalities. For example, the dielectric constant of $PbTiO_3$ is enhanced in short period $SrTiO_3$-$PbTiO_3$ superlattices as a result of structural reconstructions near the interface.[9]

In this thesis, the interplay between materials at the interface is explored. With the current thin film deposition techniques, it is possible to achieve atomically sharp interfaces, leading to abrupt transitions in composition and structure at the interface. As a result of these transitions, structural, electronic or ionic reconstructions are likely to occur at the interface and new functionalities can arise near the interface. However, the origin of the new properties are not always well understood, yet.

Here, the interface behavior of complex oxide heterostructures is studied in a variety of cases. In each chapter, an important aspect for the understanding of the interfaces is highlighted. Ionic, electronic and structural reconstructions are taken into account. For specific material systems, the presence of several reconstructions are suggested to be diminished, while other reconstructions are still expected to be able to occur. As a consequence, the origin of the existing reconstructions can be studied in more detail, which also gives rise to a better understanding of complex oxide interfaces in general.

The thesis is constructed the following: *Chapter 2* concerns the interface between crystal surface and vacuum. Therefore, no interplay between different crys-

talline materials can occur. *Chapter 3* involves the interface between a crystalline and an amorphous oxide. As a result, electronic and structural reconstructions are expected to be negligible. In *chapter 4*, crystalline heterostructures with a polar discontinuity at the interface are presented. To overcome a potential build-up, electronic reconstruction has been proposed to occur at the interface, but has not been observed experimentally.[10, 11] Structural and ionic reconstructions have been observed at this interface.[12, 13] In *chapter 5*, electronic reconstruction in an iso-polar material system is discussed. As a result of the structural compatibility, alignment of oxygen bands is suggested to occur. The band alignment is proposed to induce charge transfer near the interface.

1.2 Outline

Below, each chapter is shortly described in more detail.

Well-defined, singly terminated surfaces are essential for thin film growth and interface studies of complex oxide heterostructures. In *chapter 2*, the study on rare earth scandate ($REScO_3$) (110) surfaces is described. A selective wet etching surface treatment is presented resulting in ScO_2 terminated surfaces. Furthermore, a powerful method is presented, which combines the determination of the predominant surface termination and verification of complete single termination. In the [110] direction, the bulk $REScO_3$ atomic planes are polar which results in a polar discontinuity at the surface. This is energetically unfavorable and therefore surface reconstructions are likely to occur. In this chapter, the surface structure of Sc terminated $DyScO_3$ has been investigated.

Chapter 3 gives insight in the chemical driving forces at oxide interfaces during fabrication. The chemical driving forces have been explored for heterostructures of crystalline $SrTiO_3$ and various amorphous oxide films. Their interfaces can be tuned from insulating to metallic by varying the growth pressure, film material and film thickness. X-ray photoelectron spectroscopy measurements indicate oxygen vacancy formation in $SrTiO_3$ near the interface during deposition. Here, it has been proposed that redox reactions between the $SrTiO_3$ substrate surface and the amorphous film play an important role in the formation of oxygen vacancies and, as a result, in the interfacial behavior.

Chapter 4 discusses the interface between a polar and a non-polar wide band gap insulator. Depending on the exact atomic stacking, the interface between $LaAlO_3$ (polar) and $SrTiO_3$ (non-polar) can become metallic.[10] At the atomic level, a polar discontinuity is present at the interface. To avoid a potential build-up, electronic, ionic or structural reconstructions have to occur at the interface. Here, the influence of the $SrTiO_3$ template on the electronic properties of the interface is investigated. Using several deposition techniques, the defect state of $SrTiO_3$ was varied. Furthermore, the unit cell structure of $SrTiO_3$ was tuned by applying biaxial strain. It is suggested that the interface behavior depends on crystal structure as well as on the defect state of $SrTiO_3$.

Chapter 5 describes the interface between two iso-polar insulators, $LaTiO_3$ and $LaFeO_3$. $LaFeO_3$ is a charge transfer (CT) insulator and $LaTiO_3$ is a Mott-

Hubbard (MH) insulator. Here, it is proposed that their oxygen p bands align near the interface of a MH-CT heterostructure. As a result, the empty upper Hubbard band of the CT insulator is pulled below the energy level of the partially filled lower Hubbard band of the MH insulator. Subsequently, in $LaFeO_3$-$LaTiO_3$ heterostructures, electron transfer from Ti^{3+} to Fe^{3+} is expected to occur. The $LaTiO_3$-$LaFeO_3$ heterostructures were studied by X-ray photoelectron spectroscopy. Reduction of Fe was clearly observed and depended strongly on the $[LaTiO_3]/[LaFeO_3]$ ratio.

Chapter 2

Atomically defined rare earth scandate crystal surfaces

Abstract

In this chapter, the fabrication of well-defined, atomically smooth substrate surfaces over a wide range of lattice parameters is reported, which is crucial for atomically controlled epitaxial growth of complex oxide heterostructures. Here, the large chemical sensitivity of basic solutions on rare earth scandates ($REScO_3$) is exploited, resulting in singly terminated (110) surfaces. By introducing an etching step that increases the step edge density at the surface, the influence of the surface morphology after annealing is reduced. Angle resolved mass spectroscopy of recoiled ions (AR-MSRI) measurements show that the surfaces are predominantly ScO_2 terminated after selective wet etching. The morphology study of $SrRuO_3$ thin film growth gives no evidence for mixed termination. Therefore, it is concluded that the $REScO_3$ surfaces are complete ScO_2 terminated.

The structure of polar $DyScO_3$ (110) surfaces was studied by reflection high energy electron diffraction, surface X-ray diffraction (SXRD) and AR-MSRI. It is shown that the $DyScO_3$ (110) surfaces are (1×1) reconstructed, which points to the absence of ordered cation vacancies at the surface. Moreover, the SXRD data indicate that cation displacements in relation to the bulk plane are unlikely to be present. Here, it is suggested that the polarity difference between the bulk crystal and vacuum is most likely overcome by the presence of oxygen vacancies in the topmost Sc layer, while preserving the orthorhomic unit cell.[1]

2.1 Introduction

Perovskite-type oxides, ABO_3, are an interesting class of materials as they exhibit diverse properties, such as superconductivity, magnetism and ferroelectricity.[15–

[1] Parts of this chapter are reproduced with permission from ref. [14].

17] Their similar oxygen backbone structure allows the formation of strained heteroepitaxial structures of high complexity, resulting in advanced materials with enhanced functionality.[5, 6, 10, 18, 19] The formation of conducting interfaces between $SrTiO_3$ and $LaAlO_3$, both wide bandgap insulators, is an example where the functionality is determined at an atomic level.[10] For well controlled growth of epitaxial heterostructures, it is essential to start with defined, crystalline substrates with a singly terminated atomic plane.[20, 21] However, two important aspects limit the availability of singly terminated surfaces: 1) Established techniques to obtain single termination are currently limited to one material, $SrTiO_3$, and 2) Proof of complete single termination has been difficult.

The (pseudo)cubic unit cell of a perovskite-type oxide can be seen as a stack of alternating layers of AO and BO_2 in the [001] direction (Fig. 2.1a). After creating a surface by, for instance, cleaving a single crystal, both layers are expected at the surface in equal proportion, resulting in mixed terminated surfaces with steps of half or one unit cell height (0.2 and 0.4 nm respectively) (Fig. 2.1b). However, single termination, only 0.4 nm high steps (Fig. 2.1c), is desirable for controlled growth at an atomic level.[2] Therefore, it is crucial to treat the surface before growing complex heterostructures. The typical surface treatment of perovskite-type oxides is high temperature annealing which results in ordered, well-defined, crystalline surfaces. Nonetheless, it is inadequate to obtain single termination, i.e., half a unit cell steps are still present. Kawasaki *et al.* introduced wet etching of $SrTiO_3$ (001), which was the first serious step towards singly terminated perovskite-type surfaces.[20] By etching the surface with an acidic NH_4F buffered HF solution (BHF), they obtained a TiO_2 terminated surface, as confirmed by ion scattering spectroscopy. To obtain single termination, the pH of the etchant is claimed to be crucial to achieve selectivity. However, since the treatment severely depends on the $SrTiO_3$ surface quality[3] prior to etching, this method often leads to uncontrolled wet etching. To etch $SrTiO_3$ in a controlled manner, Koster *et al.* introduced the formation of an intermediate Sr-hydroxide complex at the topmost surface by immersion in water.[21] By subsequent short BHF etching, reproducible TiO_2 terminated surfaces were obtained. Currently, this method is expanded to $SrTiO_3$ (111) by removing SrO_3^{4-}, giving a Ti terminated surface.[22, 23] Unfortunately, the success of this technique to create singly terminated surfaces is limited to $SrTiO_3$ and is not suitable for other perovskite-type oxides. Note that Ngai *et al.* obtained predominant A-site terminated $La_{0.18}Sr_{0.82}Al_{0.59}Ta_{0.41}O_3$ (LSAT) surfaces by tuning the vapor pressure of La near the LSAT surface during annealing.[24] This is an important step towards controlling the surface termination of LSAT.

To study the effects of strain and symmetry variations on the physical behavior of complex heterostructures, it is essential that controllable single termination can be achieved on different perovskite-type oxide surfaces with a wide range of lattice parameters, as it is currently limited to $SrTiO_3$.[8, 25–28] Moreover, an increase

[2]Surfaces with terraces seperated by steps of atomic height result from the small miscut angle between the crystal axis and the cleaving axis. These surfaces are also called vicinal surfaces.

[3]The quality of the $SrTiO_3$ surface is mainly determined by surface roughness and point defects.

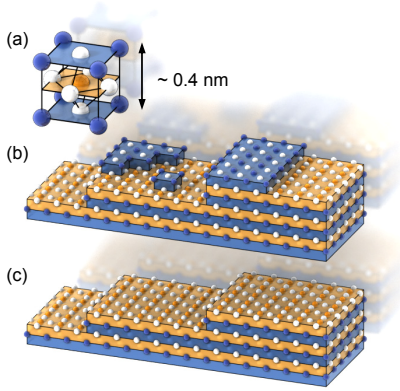

Figure 2.1: (a) The ABO_3 unit cell, where A is typically a rare earth, alkaline earth or alkali metal ion, and B is often a transition metal ion. (b) A schematic representation of a mixed terminated surface with steps of 0.2, 0.4 and 0.6 nm high. (c) A singly terminated BO_2 surface with steps of 0.4 nm high. The blue blocks correspond to the AO layer and the yellow blocks to the BO_2 layer with blue, yellow and white circles corresponding to A, B and O ions, respectively.

of singly terminated perovskite-type oxides expands the research possibilities on interface effects in oxide heterostructures, which is useful for the research studies presented in this thesis. An overview of substrates which are often used for complex oxide heterostructures, is shown in Figure 2.2. The substrates are ordered by their pseudocubic lattice parameter.

High quality perovskite-type scandates are frequently used to create strained heterostructures, as they have a relatively large lattice parameter (0.394 - 0.404 nm) and can be grown without twinning.[8, 28–30] However, surface treatments for perovskite-type scandates have hardly been addressed in literature.[31–33] Recently, Dirsyte *et al.* showed that annealing of $DyScO_3$ at high temperatures in

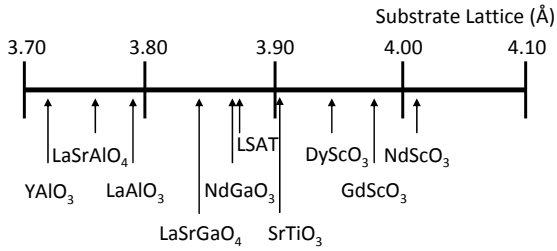

Figure 2.2: An overview of commercially available and often used perovskite-type oxide substrates ordered by their pseudocubic lattice parameter.

an O_2 flow leads initially to an increase of Dy at the surface.[33] By prolongating the annealing time to more than 100 minutes, they observed a change of the predominant cation at the topmost surface layer. Annealing $DyScO_3$ substrates in an Ar flow resulted in surfaces with mainly Sc termination, independent of the annealing time. In spite of the possibility to control the predominant cation at the topmost layer by choosing the right annealing parameters, no complete single termination of rare-earth scandate ($REScO_3$) surfaces is achieved yet.

In this chapter, a framework for controlled selective wet etching of perovskite-type oxides is introduced and applied on the $REScO_3$. $DyScO_3$ (110) crystals were taken as a model system. The influence of the etchant as well as morphology of the crystal surface were taken into account to achieve a proper selective etching method. Subsequently, angle resolved mass spectroscopy of recoiled ions (AR-MSRI) was used to determine the dominant termination of the surfaces. Despite the capability of chemical probe techniques, like AR-MSRI, to establish the dominant termination, these techniques are not capable of proving complete single termination of perovskite-type surfaces. To overcome this difficulty, the high sensitivity of $SrRuO_3$ nucleation on the atomic composition of the surface was introduced to prove complete single termination. Finally, the surface structure of $DyScO_3$ (110) has been studied by reflection high energy electron diffraction (RHEED), AR-MSRI and surface X-ray diffraction (SXRD). The $DyScO_3$ (110) bulk surface planes are polar (DyO^+ and ScO_2^-) and, therefore, reconstructions are likely to occur.

2.1.1 Properties of bulk $REScO_3$

The $REScO_3$ have an orthorhombic unit cell, isostructural with $GdFeO_3$ (*Pbnm*). This means that the ideal cubic perovskite structure is distorted. The scandium cation is centered in the oxygen octahedron, where the typical Sc-O bond length is in the range of 0.2090 - 0.2116 nm.[34] This points to a rather small distortion on the B-site, giving Sc a six-fold coordination. On the other hand, the RE-O bond length is in the range of 0.2233 - 0.3722 nm. This indicates a high distortion and makes the assignment of the coordination number (CN) of the rare-earth cation difficult. By Veličkov *et al.*, it is mentioned that a CN of 8 can be assumed for the A-site cations.[34] The orthorhombic as well as the pseudocubic lattice parameters of commercially available $REScO_3$ crystals are given in Table 2.1. The single crystals are grown by the conventional Czochralski technique, as reported by Uecker *et al.*.[30]

The Czochralski growth technique does not tend to produce crystals with high internal strain, in contrast to the Verneuil growth technique which is used to obtain $SrTiO_3$ single crystals. In general, this results in less defects for Czochralski grown crystals. The increased crystal quality has been shown by XRD rocking curves of $SrTiO_3$ and $DyScO_3$. The FWHM of the XRD rocking curve along the (002) of $SrTiO_3$ is five times larger than that of $DyScO_3$, implying more defects in the $SrTiO_3$.[35]

The lattice parameters shown in Table 2.1 are the ones at room temperature. Biegalski *et al.* have studied the thermal expansion of $DyScO_3$ and $GdScO_3$.[36] No

Table 2.1: Lattice constants of $RE ScO_3$. Data are taken from [30, 34].

Crystal	a (nm)	b (nm)	c (nm)	$0.5\sqrt{a^2+b^2}$ (nm)	$0.5c$ (nm)
$DyScO_3$	0.5440	0.5717	0.7903	0.3946	0.3952
$TbScO_3$	0.5466	0.5731	0.7917	0.3960	0.3959
$GdScO_3$	0.5480	0.5746	0.7932	0.3970	0.3966
$SmScO_3$	0.5527	0.5758	0.7965	0.3991	0.3983
$NdScO_3$	0.5575	0.5776	0.8003	0.4014	0.4002

structural phase transitions were observed between room temperature and 1000 °C, though the orthorhombicity decreased with increasing temperature. The thermal expansion (8.4 ppmK^{-1} for $DyScO_3$ and 10.9 ppmK^{-1} for $GdScO_3$)[4] were found to be anisotropic, which was attributed to the rotation of the ScO_6 octahedra. As the thermal expansion coefficients are comparable to other oxide perovskites, like $SrTiO_3$ and $BaTiO_3$, these crystals are promising for studies on heteroepitaxial films.[37]

Besides the structural properties of the substrate, the physical properties of the substrate may influence the behavior of the heterostructure. $RE ScO_3$ are highly insulating, with an optical bandgap > 5.5 eV.[38] The scandates are paramagnetic at room temperature and have a magnetic phase transition to antiferromagnetic long range order at low temperatures; for $DyScO_3$ at 3.1 K.[38, 39] A strong magnetic anisotropy was observed with an easy axis along the [100] direction and a hard axis along the [001] direction.[39] It is also suggested that $RE ScO_3$ have high dielectric constants, but this is only reported for $RE ScO_3$ thin films.[40]

2.1.2 Selective wet etching framework

To develop a selective wet etching framework for perovskite-type oxides, wet etching was considered as a combination of two steps, as also shown in Figure 2.3:

1) Forming a hydroxide
2) Dissolving the hydroxide

Perovskite-type oxides can be viewed as a combination of two simple oxides along the [001] direction: AO and BO_2. To establish single termination, selectivity has to be achieved by controlling both etching steps, for AO as well as for BO_2. This control can be achieved by selecting the right etching solution(s), temperature and duration. When the difference in overall etching rates of AO, K_A, and BO_2, K_B, is significant, both steps can be performed simultaneously. Another approach is to separate the steps in time, exploiting the differences between the two etching processes. The latter approach was introduced by Koster *et al.* for $SrTiO_3$ (001).[21] Immersing $SrTiO_3$ in water, forming $Sr(OH)_2$, increased the solubility of the Sr layer. By this, the difference between k_{Sr_2} and k_{Ti_2} was increased significantly,

[4]The given values are the average thermal expansion coefficients.

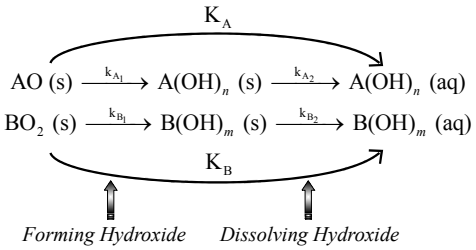

Figure 2.3: Framework for controlled selective wet etching of perovskite-type oxides, where k_{A_1}, k_{A_2}, k_{B_1} and k_{B_2} are the etching rate constants of the separate steps and k_A and k_B are the overall etching rate constants of the AO and BO_2 layer, respectively. n and m depend on the valence of the cation.

resulting in reproducible TiO_2 terminated $SrTiO_3$ surfaces. Creating singly terminated surfaces on other perovskite-type oxides can be achieved by controlling the rates of the two etching steps.

2.1.3 Chemistry of Dy and Sc

To obtain a suitable chemical method resulting in singly terminated $DyScO_3$, the chemistry of the elements, Dy and Sc, and their stable oxides, Dy_2O_3 and Sc_2O_3, is discussed. Dysprosium (atomic number (Z) = 66, [Xe] $4f^{10}6s^2$) is part of the lanthanoids. Scandium (Z = 21, [Ar] $3d^14s^2$), a $3d$ element, is often considered as a lanthanoid, since its chemical behavior is similar to them. Both elements react vigorously with air, forming a sesquioxide (A_2O_3). The reaction with acids, like HNO_3 and HCl, is mild, forming $Sc(NO_3)_3$ ($Dy(NO_3)_3$) and $ScCl_3$ ($DyCl_3$) respectively. On the other hand, no reaction with alkaline solvents, like NaOH (aq), is observed. The stable oxidation state of both cations is 3+. Other oxidation states are rarely observed and, therefore, are not taken into account.

The sesquioxides, the stable oxides of Dy and Sc, are readily soluble in acidic solutions. As a consequence, it is expected that selectivity for one of the $DyScO_3$ atomic planes is minimal in acidic solutions.[41] In basic solutions, like NaOH (aq), both sesquioxides are insoluble.[42] However, small modifications, e.g. in the crystal structure, may be sufficient to induce significant solubility of Sc and/or Dy in basic solutions. Selectivity for one of the cations may be induced through the difference in electrostatic bond strength (e.b.s.) of Sc and Dy towards the oxygen ions.[42] The e.b.s. of the cations is defined as

$$e.b.s. = n/CN \tag{2.1}$$

where n is the valence state of the cation.[42] Applying equation 2.1 on the sesquioxides, Dy as well as Sc have an e.b.s. of $\frac{1}{2}$ (n=3+, CN=6). In the distorted perovskite structure, Dy and Sc have different coordination numbers: the e.b.s. of Dy is $\frac{3}{8}$ (n=3+, CN=8) while the e.b.s. of Sc is $\frac{1}{2}$ (n=3+, CN=6). This could induce an increased reactivity of Dy versus Sc in basic solutions. Therefore,

it is expected that the following reaction with $DyScO_3$ in basic solutions dominates the etching process:

$$Dy_2O_3\ (s)\ +\ 3\ H_2O\ (l) \xrightarrow{6\ OH^-\ (aq)} 2\ Dy(OH)_3\ (aq) \tag{2.2}$$

where OH^- acts as a catalyst. This should result in ScO_2 terminated surfaces. Moreover, this methodology can be extrapolated to other $REScO_3$ since the lanthanoids behave chemically similar.

2.2 Experimental Setup

Selective wet etching: $DyScO_3$ (110) substrates (CrysTec GmbH, Germany) of $5\times5\times0.5$ mm^3 were annealed at 1000 °C for 30 minutes to 12 hours under flowing O_2. After cleaning with ethanol, the annealed substrates were successively immersed in 12 M NaOH (aq) solution[5] (etching) and in 1 M NaOH (aq) solution (preventing precipitation[6]). Both immersion steps were carried out in an ultrasonic bath for 10 minutes to 1 hour. Finally, the samples were rinsed with water (three times) and ethanol. $NdScO_3$ (110) and $GdScO_3$ (110) (CrysTec GmbH, Germany) of $5\times5\times0.5$ mm^3 were annealed at 1000 °C for 4 hours under flowing O_2. The annealed substrates were successively immersed for 1 hour in 12 M NaOH (aq) solution and 30 minutes in 1 M NaOH (aq) solution. Both immersion steps were carried out in an ultrasonic bath. Finally, the samples were rinsed with water (three times) and ethanol. $SrTiO_3$ (001) substrates (CrysTec GmbH, Germany) of $5\times5\times0.5$ mm^3 were treated in accordance with the method described by Koster *et al.* and Ohnishi *et al.*.[21, 43]

Surface morphology analysis: The surface morphology was characterized *ex situ* using tapping mode atomic force microscopy (AFM) (Veeco's Dimension Icon, United Kingdom). Scanning tunneling microscopy (STM) was performed *in situ* on a variable-temperature scanning probe microscope (VT-SPM; Omicron NanoTechnology GmbH, Germany).

Angle resolved mass spectroscopy of recoiled ions: Before the AR-MSRI measurements, the substrates were cleaned in trichloroethene, acetone and isopropanol in turn. All cleaning steps were carried out in an ultrasonic bath. Inside the high vacuum AR-MSRI chamber (below 10^{-6} mbar), the substrates were heated to 500-600 °C with 0.07-0.13 mbar O_2 to remove hydrocarbons on the substrates. AR-MSRI measurements (Ionwerks' time-of-flight mass spectrometer, USA) were performed using potassium ions ^{39}K accelerated to 10 keV. The incoming angle, α, was fixed at 15°, while the azimuthal angle, δ, was varied. Ion collection was done in shadowing mode, i.e. ions were collected at 60°, an angle much larger than the incident angle. Ions with masses up to 200 amu could be detected. The measurements were performed at room temperature to 150 °C. Note that $DyScO_3$ has no structural phase transition in this temperature range, as mentioned in

[5]Deionized water was always used to make the NaOH (aq) solutions

[6]Precipitation may occur due to the large difference in pH between 12 M NaOH (aq) (pH > 14) and water (pH $\sim$ 7).

section 2.1.1.

$SrRuO_3$ growth: Using specific growth conditions, the nucleation and growth of $SrRuO_3$ is very sensitive to the atomic composition of the surface.[14, 44] $SrRuO_3$ was grown using pulsed laser deposition (PLD) at a pressure of 0.3 mbar, 50%-50% O_2-Ar. The substrate temperature was approximately 600-640 °C. $SrRuO_3$ was deposited with a repetition rate of 1 Hz and a fluence of 2.1 J cm^{-2}, using a KrF laser ($\lambda = 248$ nm). The growth was studied *in situ* using RHEED. It has to be mentioned that the sensitivity to selective nucleation depends on the growth conditions.

Enhancement of selective etching rate: The morphology of the $DyScO_3$ (110) surface prior to selective etching influences the selective etching rate.[45] To control the etching rate, the number of step edges was increased at the atomic level. The substrates were immersed in water for 30 minutes, and, subsequently, in a BHF solution (NH_4F:HF = 87.5:12.5, pH=5.5) for 30-60 seconds. Both steps were performed in an ultrasonic bath. To rinse the samples, they were immersed in water (three times) and ethanol. Subsequently, the selective wet etching was performed, as described above.

Surface X-ray diffraction: The SXRD measurements were done using the (2+3) axis diffractometer on BM26 (DUBBLE) beamline at the ESRF (Grenoble, France) at an energy of 16 k*e*V.[46] The substrates were heated up to 250 °C under a constant flow of dry nitrogen in order to eliminate the influence of adsorbed water at the surface. The recorded data were processed and analyzed with the ANA-ROD package using χ^2 as goodness-of-fit criterion for the models presented.[47] For each sample, a minimum of six crystal truncation rods (CTR) plus the specular rod are measured.

2.3 Achievement of Single Termination

2.3.1 Selective wet etching

To study the effect of the surface treatment, AFM was used to determine the surface morphology after various steps of the treatment (see Figure 2.4). As received $DyScO_3$ substrates have a mixed terminated surface as they show disordered step edges and islands on terraces with typical height differences of 0.2 and 0.4 nm (inset of Fig. 2.4a). High temperature annealing at 1000 °C resulted in recrystallization of the surface, leading to regularly spaced steps with a height of 0.4 nm (Fig. 2.4a), appearing to be single termination. However, this is not a sufficient observation to conclude the existence of a complete singly terminated surface, as will be demonstrated below. The minimum duration of high temperature annealing depends on the miscut. For substrates with a miscut of approximately 0.1°, 4 hours annealing at 1000 °C resulted in well-defined, ordered steps after etching. $DyScO_3$ (110) with a lower miscut required longer annealing time.[7]

To obtain singly terminated $DyScO_3$ (110) surfaces, controlled selective wet etching was applied using 12 M NaOH (aq) solution. An annealed $DyScO_3$ sub-

[7]Note that longer annealing may influence the minimum required etching time.

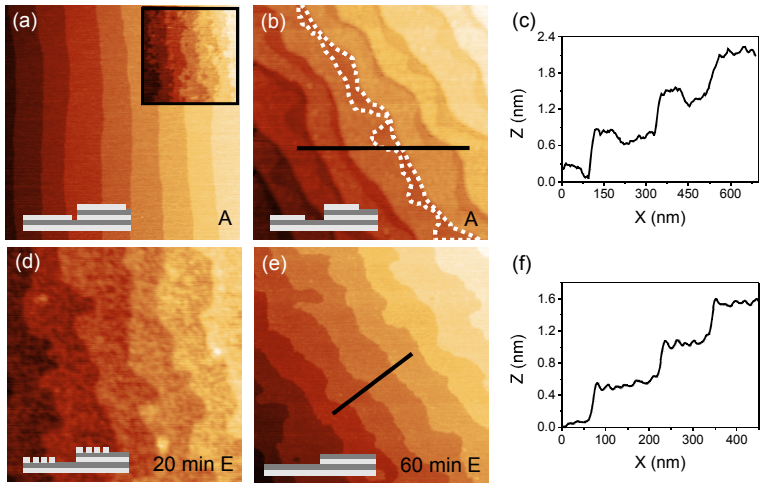

Figure 2.4: (a) AFM height images of $DyScO_3$ (110) substrate after 4 hours annealing at 1000 °C with steps of one unit cell high. AFM height images of $DyScO_3$ after annealing (b) after 30 minutes annealing at 1000 °C with clear mixed termination having steps of 0.2, 0.4 and 0.6 nm high, marked by the dashed line and also shown in its corresponding line profile (c), and subsequently after (d) 20 minutes immersion in 12 M NaOH (aq) and after (e) 1 hour immersion in 12 M NaOH (aq) with its corresponding line profile showing only 0.4 nm steps (f). The labels A and E denote substrates after Annealing and after wet Etching respectively. The inset of (a) shows an AFM height image of an as received $DyScO_3$ (110). The sketches give a schematic representation of the surface layer. All AFM images are $1 \times 1\ \mu m^2$.

strate with a clear mixed terminated surface was etched for different lengths of time to examine the required etching duration (Fig. 2.4b and its corresponding line profile, Fig. 2.4c). Figure 2.4d and 2.4e show the results after 20 minutes and 1 hour immersion in 12 M NaOH (aq), respectively. After 20 minutes, the top layer is partly removed, as schematically depicted in Figure 2.4d. Elongating the etching time to one hour for the same sample, steps of only one unit cell high (0.4 nm) were observed (Fig. 2.4f). The lack of half unit cell steps after immersing in 12 M NaOH (aq) suggests that one of the atomic planes (DyO or ScO_2) is selectively removed, pointing to single termination. Further exposure to 12 M NaOH (aq) appeared not to damage the surface since no etch pits were observed. The $DyScO_3$ surface remained stable after etching.

In addition to obtaining single termination, the treatment has to result in ordered, well-defined surfaces. To achieve well-defined surfaces with straight steps, it is common to anneal the surface after etching, allowing recrystallization.[20, 21] However, the order of treatments is the opposite for $DyScO_3$, which consists of first annealing and then etching. This order is important; when annealing at 1000 °C is performed after wet etching, the $DyScO_3$ surface termination became mixed

due to major bulk diffusion. This is consistent with the observations of Dirsyte *et al.*.[33] Note that the temperature during thin film growth is typically below the temperature where major bulk diffusion occurs and, therefore, should not result in unintended mixed termination of the surface. Since only one of the atomic layers seemed to be removed by 12 M NaOH (aq) (illustrated in Fig. 2.4), the overall vicinal morphology is preserved after selective etching.

2.3.2 Determination of surface termination

The changes in surface morphology at different time steps during etching pointed to the selective removal of one of the atomic planes. Taking the chemistry of Dy and Sc into account, it was suggested that Dy can be removed by immersing in NaOH (aq) (see eq. 2.2). As a result, ScO_2 terminated surfaces are expected after the chemical treatment. The predominant surface termination has been determined by AR-MSRI measurements (Fig. 2.5a). AR-MSRI measurements were performed on three differently treated $DyScO_3$ surfaces: as received, annealed and selectively wet etched (Fig. 2.5b).[48]

Full range mass spectra of the three samples were collected at different azimuthal angles and normalized with respect to the integrated intensity of the Sc peak. Figure 2.5b shows the Sc/Dy intensity ratio as function of the azimuthal angle for the three different samples. No clear maxima were observed in the spectra of the as received and annealed $DyScO_3$ surfaces, which indicates mixed termination. On the other hand, the wet etched sample shows clear maxima at 45° and 135°. This is due to blocking of Dy by the topmost Sc atoms and can only be observed when the surface is predominantly ScO_2 terminated (Fig. 2.5c). As $Sc(OH)_6^{3-}$ is soluble in alkaline solutions as well, it is most likely that the difference in etching rate is gained during hydroxide formation: $k_{Dy_1} \gg k_{Sc_1}$, which is crucial for achieving selectivity towards ScO_2 terminated $DyScO_3$ (110). This explains why the NaOH (aq) solution does not etch beyond the top layer and no etch pits are created.

The AR-MSRI analysis on treated $GdScO_3$ and $NdScO_3$ substrates (Fig. 2.5d and e) show clear maxima for the wet etched surfaces at 45° and 135°, indicating Sc terminated surfaces. This implies that the surface treatment is effective for all $REScO_3$. Since ScO_2^- is polar, a combination of oxygen vacancies, structural reconstruction and adsorbates is likely to occur at the surface. However, this should not affect the predominant type of cation at the topmost layer. The surface structure of $DyScO_3$ is discussed in more detail in section 2.4.

2.3.3 Confirmation of complete single termination

Despite the suitability of AR-MSRI and other chemical probing techniques to determine the dominant terminating layer, their ability to prove complete single termination of perovskite-type oxide surfaces is compromised since the elements present at the surface are also present in the bulk. Therefore, a simple method to determine complete single termination of $DyScO_3$ is introduced: thin film growth of $SrRuO_3$.

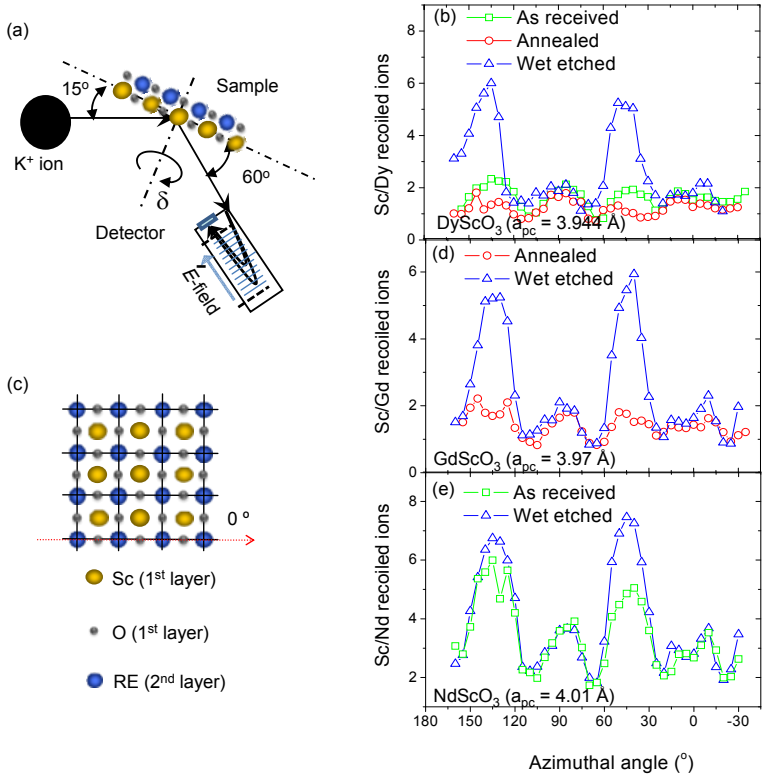

Figure 2.5: (a) Schematic picture of the AR-MSRI setup, where δ denotes the azimuthal angle. The yellow, blue and gray circles correspond to Sc, RE and O ions, respectively. (b) Azimuthal maps of three different treated $DyScO_3$ (110) surfaces are shown: as received, 4 hours annealed and 4 hours annealed and 1 hour wet etched. Maximum blocking of Dy was observed on the wet etched surface at 45° and 135°. (c) A top down view of the atomic arrangement on an unreconstructed ScO_2 terminated $REScO_3$ (110) surface, where the arrow indicates the direction of 0° azimuthal angle. (d) Azimuthal maps of a 4 hours annealed and a 4 hours annealed and 1 hour wet etched $GdScO_3$ (110) with maximum blocking of Gd at 45° and 135° after wet etching. (e) Azimuthal maps of an as received and a 4 hours annealed and 1 hour wet etched $NdScO_3$ (110) with maximum blocking of Nd at 45° and 135°. The measurements were performed in CONCEPT lab at the University of California in Berkeley (CA).

The nucleation of $SrRuO_3$ is very sensitive to differences in surface diffusivity, which amplifies the presence of small areas of mixed termination (see section 2.2 for specific growth conditions). As a result, the mixed or single termination can easily be observed in the morphology of the $SrRuO_3$ layer by AFM and STM.[44, 49–51] From $SrRuO_3$ on $SrTiO_3$ (001) studies, it is known that initial two dimensional $SrRuO_3$ growth occurs when the substrate is singly terminated. An example is given in Figure 2.6a with its corresponding line profile in Figure 2.6b.[49] However,

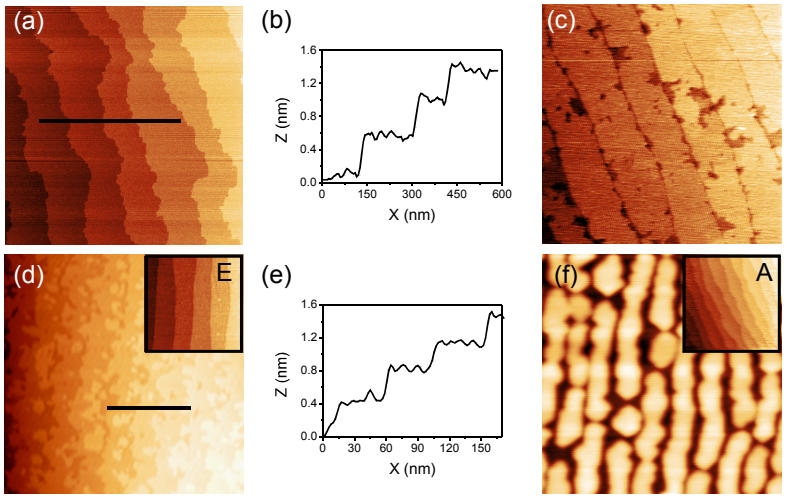

Figure 2.6: *In situ* STM height images of (a) 2 nm $SrRuO_3$ film on TiO_2 terminated $SrTiO_3$ (001) showing steps of one unit cell high with its corresponding height profile (b) and of (c) 3 nm $SrRuO_3$ on mixed terminated $SrTiO_3$ (001) with trenches of approximately 3 nm deep. (d) *In situ* STM height image of 8 nm film of $SrRuO_3$ on annealed and subsequently 1 hour wet etched $DyScO_3$ (110) showing steps of one unit cell high with its corresponding height profile (e). (f) AFM height image of 4 to 8 nm high lines of $SrRuO_3$ on annealed $DyScO_3$ (110). The insets show AFM height images of the corresponding substrates, where E and A denote substrates after wet Etching and after Annealing respectively. Images (a), (c) and (f) and both insets are 1×1 μm^2, image (d) is 500×500 nm^2.

deep trenches in grown $SrRuO_3$ films are typically observed when the $SrTiO_3$ surface is slightly mixed terminated (Fig. 2.6c).[50, 51] On $DyScO_3$, the same phenomena is observed.

Figure 2.6d shows a flat film of $SrRuO_3$ with terraces of one unit cell high and without deep trenches (see Fig. 2.6e for its corresponding line profile). This film was grown on an annealed and subsequently wet etched $DyScO_3$ substrate. This indicates 100% single termination of $DyScO_3$ after wet etching. Based on the lateral resolution being better than 10 nm and the fact that no domains with step heights different from 0.4 nm were observed on a micron-size scan, complete single termination with a better than 1% uncertainty was concluded. On annealed $DyScO_3$, random line growth was observed (Fig. 2.6f), indicating mixed terminated $DyScO_3$ surface after annealing.[44] These results are in agreement with the AR-MSRI measurements and confirm complete single termination after wet etching.

To verify the quality of the $SrRuO_3$ growth on $SrTiO_3$ and on $DyScO_3$, the film structure and surface morphology were monitored by RHEED (Fig. 2.7). The intensity versus time of the specular spot (00) of the two dimensional grown $SrRuO_3$ films $SrTiO_3$ as well as on $DyScO_3$ showed both one clear oscillation and two weak

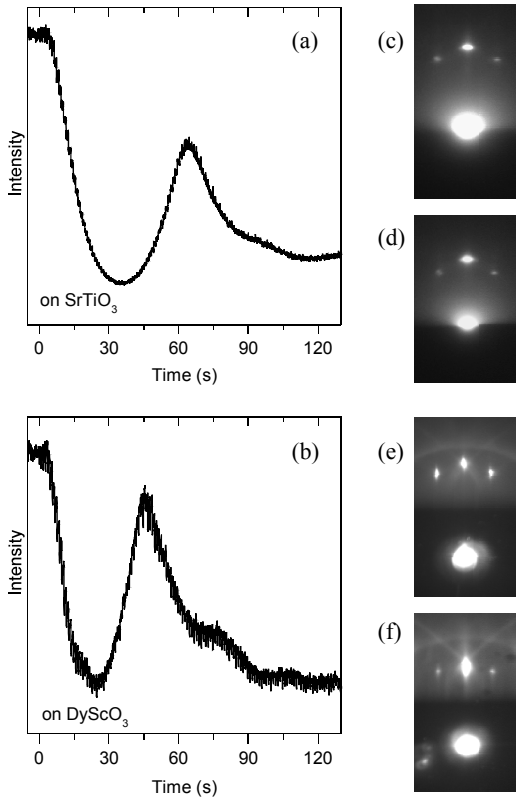

Figure 2.7: *In situ* reflection high energy electron diffraction analysis of $SrRuO_3$ growth. The intensity versus time of the specular spot during the initial $SrRuO_3$ growth on $SrTiO_3$ (a) and on $DyScO_3$ (b). The RHEED patterns before and after growth on $SrTiO_3$ (c and d respectively) and on $DyScO_3$ (e and f respectively) show the crystalline quality of the surfaces.

oscillations (Fig. 2.7a and b, respectively). During $SrRuO_3$ growth on TiO_2 terminated $SrTiO_3$, the surface termination switches from B to A-site termination, since RuO_2 is volatile.[49] As a result, the first RHEED oscillation lasts longer than the following oscillations, which is clearly visible in Figure 2.7a. The first oscillation on $DyScO_3$ was also elongated, implying that the $DyScO_3$ surface was ScO_2 terminated, which is in agreement with the AR-MSRI measurements. After the first clear oscillation, a mixture of layer-by-layer and step-flow growth occurred, i.e. one unit cell high island nucleation, but constant overall morphology and constant RHEED intensity. This resulted in films with meandering step edges (Fig. 2.6a and d).[49, 52, 53] The RHEED patterns before and after $SrRuO_3$ growth (Fig. 2.7c-f) confirmed the crystallinity of the surface layer.

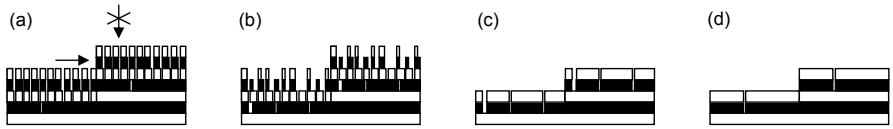

Figure 2.8: Schematic cross-sections of the $DyScO_3$ (110) top layers, where black represents the DyO planes and white the ScO_2 planes. (a) after annealing, (b) after surface roughening and subsequently selective alkaline etching (c), (d) after selective alkaline etching without surface roughening step.

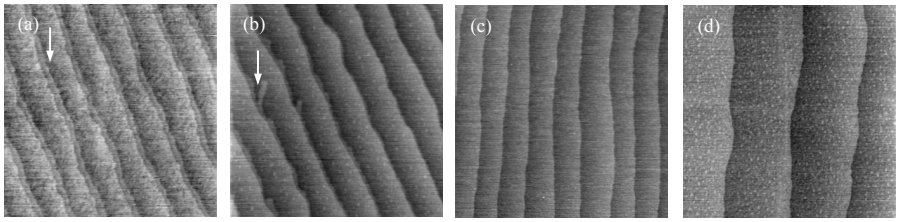

Figure 2.9: (a-d) AFM height images of $DyScO_3$ after annealing for 4 hours at 1000 °C, where (a) and (c) are 1 × 1 μm^2, and (b) and (d) are 2 × 2 μm^2. The arrows in (a) and (b) are a guide to the eye, pointing to a mixed terminated region.

2.3.4 Enhancement of etching rate

It has been shown that singly terminated $DyScO_3$ (110) surfaces can be obtained after selective etching, using 12 M NaOH (aq). This has been achieved by exploiting the difference in coordination of Dy and Sc in the $DyScO_3$ crystal. Sc seemed not to dissolve in NaOH (aq), while the etching rate of Dy was significant but slow. In follow-up studies, it appeared that the number of etching sites at the surface influences the selective etching rate. At the step edges, Dy has a lower coordination than on the surface terraces. Taking the chemistry of Dy into account, the lower coordination is expected to enhance the etching rate. This mechanism would be comparable to the chemical etching of Si (111), where the highest etching rate is observed for the isolated adatom defects and the lowest etching rate for ideally H-terminated (111) planes.[54] Also for $SrTiO_3$, it has been suggested that etching occurs at the step edges.[55] Etching at the step edges is schematically depicted in Figure 2.8a by the arrows.

The number of step edges is correlated with the surface morphology. Therefore, the surface morphology prior to selective etching has to be regulated to control the selective etching rate. Prior to selective etching, $DyScO_3$ is annealed, which straighten out the step edges, though a wide variety of surface morphologies of annealed $DyScO_3$ has been observed by AFM. Some examples of annealed $DyScO_3$ surface morphologies of are shown in Figure 2.9.

Another route to control the surface morphology and, with it, the number of step edges should be achieved. This can be achieved by exchanging the order of

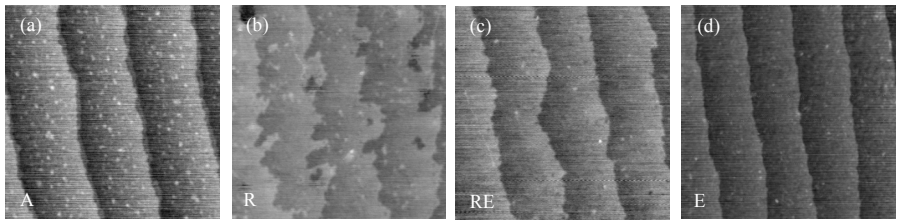

Figure 2.10: AFM height images of two $DyScO_3$ substrates. One substrate was annealed for 2 hours at 1000 °C (a), followed by the surface roughening step (b) and subsequent selective etching (c). Substrate two was annealed for 2 hours at 1000 °C, followed by selective etching (d). A, R, E and RE denote substrates after Annealing, surface Roughening, selective wet Etching and both surface Roughening and selective wet Etching respectively. All images are 1×1 μm^2.

selective etching and annealing since the as received substrate surfaces are less ordered, suggesting a higher step edge density. As mentioned before, exchanging this order gives another difficulty: Dy diffusion to the surface during high temperature annealing, resulting in mixed termination.[14, 33] Therefore, an additional etching step after annealing is introduced, which roughens the topmost layer at the nanometer scale (see Fig. 2.8b). As a result, the number of step edges is increased. Here, an acidic solvent is used to roughen the surface since both Sc and Dy easily dissolve in acidic solutions.[41, 42] This etching step will be further called the surface roughening step and discussed in the next section.

Surface roughening step

In Figure 2.10, AFM height images of $DyScO_3$ after each treatment step are shown. Figure 2.10a shows a $DyScO_3$ surface after annealing for 2 hours. Subsequently, this substrate was immersed in BHF to increase the number of step edges. Its corresponding surface morphology is shown in Figure 2.10b. Finally, selective etching was performed on the same sample (see Fig. 2.10c). As a reference, a $DyScO_3$ substrate, which was only alkaline etched for 1 hour, was prepared (see Fig. 2.10d).

As discussed previously (see section 2.3.3), $SrRuO_3$ nucleation and growth is very sensitive for differences in atomic composition of the surface. Therefore, $SrRuO_3$ was grown on $DyScO_3$ by PLD to verify single or mixed termination of the $DyScO_3$ surface.[14] Figure 2.11 shows the surface morphology after $SrRuO_3$ growth on $DyScO_3$, with and without the additional surface roughening step, measured *in situ* by non-contact AFM. The samples treated with the additional surface roughening step show the typical morphology of a flat $SrRuO_3$ film grown in a mixed step-flow and layer-by-layer growth mode, as shown in Figure 2.11a. The density of single unit cell high islands is increased in comparison to the one shown in Figure 2.6d. This is probably due to the increased number of nucleation sites after surface roughening. The presence of 0.8 nm high steps (two unit cells)

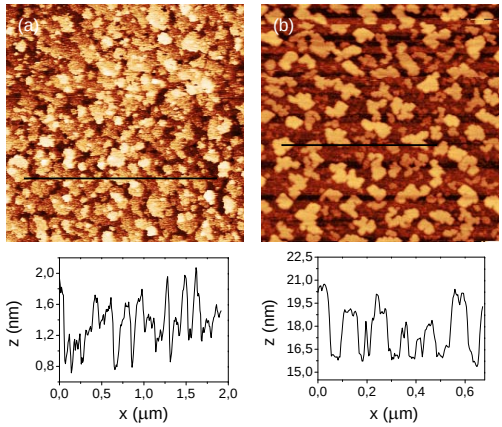

Figure 2.11: Non-contact AFM height images and their corresponding line profile of (a) 12 monolayers $SrRuO_3$ grown on a $DyScO_3$ substrate etched with BHF and 12 M NaOH (aq) and (b) 3 nm high $SrRuO_3$ islands grown on a $DyScO_3$ substrate etched with 12 M NaOH (aq). Note that the $SrRuO_3$ deposition time of (b) would be equal to a 5 nm flat $SrRuO_3$ film. (a) is 2.5 × 2.5 μm^2 and (b) is 1 × 1 μm^2.

in the line profile of Figure 2.11a is due to irregular nucleation near the step edges, though three dimensional island growth was absent. The flat $SrRuO_3$ thin film confirms single termination of the $DyScO_3$ surface.[49, 52, 53] Flat $SrRuO_3$ films were achieved independent of the surface morphology after annealing, as long as the surface roughening step was performed prior to selective wet etching. On the other hand, some samples without surface roughening showed three dimensional $SrRuO_3$ island growth (Fig. 2.11b), which is due to the mixed termination of the $DyScO_3$ surface prior to growth.[14, 44] One hour selective etching was not sufficient to remove all Dy ions of the surface. Note that the minimum required selective etching time varied from sample to sample and, therefore, the surface roughening step is introduced.

Using the surface roughening step, the influence of the surface morphology after annealing is reduced. This enables the increase of annealing time while preserving singly terminated $DyScO_3$ surfaces after selective etching. Increase of the annealing time may be desirable as annealing straighten out the step edges.

2.4 Structure Analysis

Having achieved complete Sc-terminated $DyScO_3$ surfaces, the exact surface structure of $DyScO_3$ has to be resolved. $DyScO_3$ (110) consists of charged atomic planes: DyO^+ and ScO_2^-. As a result, a perfect, bulk-like ScO_2^- terminated surface (see Fig. 2.12) is energetically unfavorable due to its polar nature and surface reconstructions are likely to occur.

Here, possible surface reconstructions are discussed on the basis of RHEED,

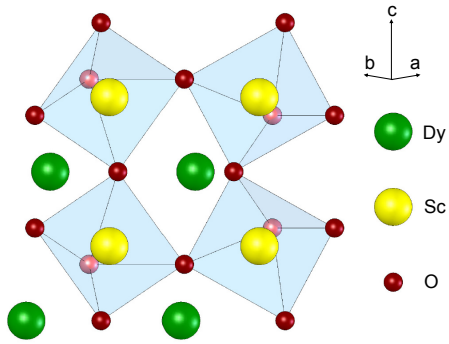

Figure 2.12: A top view of the crystal structure of the unit cell structure of bulk (110) $DyScO_3$, showing two atomic planes: ScO_2 on top and DyO underneath.

AR-MSRI and SXRD measurements. In each section, four samples at different stages of the surface treatment are discussed: after annealing (A), after annealing and surface roughening (R), after annealing and selective wet etching (E) and after annealing, surface roughening and selective wet etching (RE). According to the surface treatment, the first two samples, A and R, should be mixed terminated. On the other hand, the samples E and RE are mainly Sc terminated.

2.4.1 Reflection high-energy electron diffraction

RHEED is a well known technique to determine the primary in-plane surface structure periodicity of crystalline materials.[56] The electrons arrive at the surface under a grazing angle ($< 5°$). At these angles, the escape depth is only a few atomic layers. As a result, RHEED is a surface sensitive diffraction technique. Insulating $DyScO_3$ easily charges in an electron beam at room temperature and high vacuum due to its large bandgap (5.9 eV), complicating RHEED measurements.[38] Therefore, the measurements were done in 10^{-3} mbar oxygen to reduce surface charging; the O_2 background gas acts as a charge neutralizer.

Figure 2.13 shows the diffraction patterns along the different $DyScO_3$ (110) surface directions using 30 keV electrons. The directions are indicated using two-dimensional direct lattice vectors, where the [01] and [10] directions correspond the orthorhombic [001] and [1$\bar{1}$0] directions, respectively. No clear difference between the patterns along the [01] and [10] directions were observed, which implies an in-plane four-fold symmetry.[8,9] By determining the size of the surface unit-cell by the spacing of the diffraction spots, it was established that all diffraction patterns correspond to the bulk in-plane orthorhombic $DyScO_3$ unit cell. No su-

[8]For the measurement along the [01] direction, the direct beam was blocked by the sample holder and, therefore, not visible.

[9]Note that small differences between the [10] and [01] directions are expected to be present since they are dissimilar in the bulk lattice. However, these differences appeared to be too small to determine accurately by RHEED.

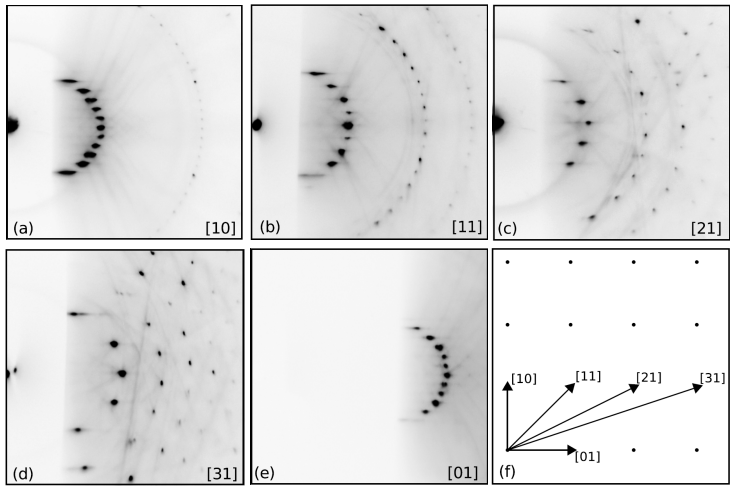

Figure 2.13: RHEED patterns of Sc terminated $DyScO_3$ along different surface directions: (a) along [10], (b) along [11], (c) along [21], (d) along [31] and (e) along [01]. (f) shows schematically the pseudocubic lattice structure, indicating the different directions.

perstructure has been observed by RHEED. This suggests that, if the surface is reconstructed, the possible reconstructions are most likely within the unit cell. No clear differences were observed between chemically treated, thermally treated and as received substrates. This is probably due to the large contribution of Dy ions to the RHEED pattern, since Dy has a large atomic form factor.

2.4.2 Angle resolved mass spectroscopy of recoiled ions

As mentioned in section 2.3.2, AR-MSRI is highly sensitive to surface composition with isotope resolution. Systematic investigations on the dependence of the mass spectroscopy of recoiled ions counts versus azimuthal angle can reveal in-plane crystalline structures.[23, 48]

Full range mass spectra were collected for the four different samples at different azimuthal angles and normalized with respect to the integrated intensity of the K peak. The Sc/Dy intensity ratio as function of the azimuthal angle for the four different samples is shown in Figure 2.14. For the singly terminated samples (RE and E), maxima at -45° and 45° were well pronounced. This is due to the blocking of Dy by the topmost Sc and O atoms and can only be observed when the surface is mainly Sc terminated. The as received substrate showed small maxima at -45° and 45°. This suggests a Sc dominant surface. Note that Dy blocking by O atoms may induce an increased Sc/Dy ratio as well. After annealing and after the surface roughening step, no maxima were visible; the $DyScO_3$ surfaces were clearly mixed terminated.

Between the E samples and the RE sample, only small differences were ob-

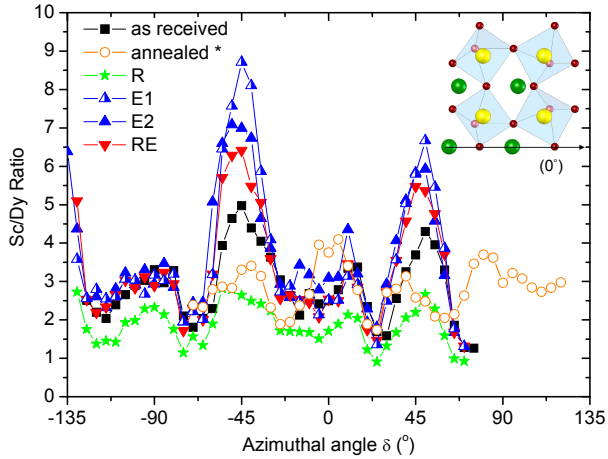

Figure 2.14: Azimuthal maps of different treated $DyScO_3$ (110) substrates: as-received, after surface roughening (R), after selective etching (E), and after surface roughening plus selective etching (RE). The data of annealed $DyScO_3$, indicated by *, was shown in Figure 2.5 as well. Maximum blocking of Dy was observed at -45° and 45°. The inset shows the topview shown in Fig. 2.12. The arrow indicates 0 azimuthal angle. The measurements were performed in CONCEPT lab at the University of California in Berkeley (CA).

served. This may be due to difference in surface roughness, which would be in agreement with the AFM morphology analysis. It has to be mentioned that, though E1 and E2 were treated equally, E1 has a slightly lower surface roughness than E2. Increase of the surface roughness smears out the structure in the recoiled features.[57] However, the angular resolution of the setup is not sufficient to measure this broadening. Despite the suitability of AR-MSRI to determine the dominant termination layer, the ability to prove single termination can be comprised by surface roughness. The possible presence of a low Dy fraction at the surface is hard to establish.

The AR-MSRI data show a four-fold rotation symmetry. Every 90°, Sc blocks Dy. Small variations may be present due to the orthorhombic crystal structure. The measurements are not accurate enough to determine slight deviations between the orthorhombic $[\bar{1}11]$ and $[1\bar{1}1]$ directions. The weak features at other angles may be due to the contribution of oxygen.

2.4.3 Surface X-ray diffraction

SXRD is a well established technique to obtain structural information on crystal surfaces. It is based on the accurate determination of the intensity of CTRs. CTRs arise due to the abrupt truncation of the crystal by its surface. The CTRs are lines, in reciprocal space, perpendicular to the surface plane and interconnecting

Table 2.2: Fractional coordinates of bulk $DyScO_3$ ($Pbnm(62)$ space group) at room temperature, as given by ICSD-99545.[61]

Atoms	x	y	z
Dy	0.0172	0.9393	0.2500
Sc	0.0000	0.5000	0.0000
O1	0.8804	0.5550	0.2500
O2	0.6926	0.3040	0.9392

bulk Bragg peaks.[58–60]

As the CTR profile depends sensitively on the precise atomic structure arrangement at the surface, it is a very useful tool to provide structural information. The crystallographic directions are chosen such that h and k lay in the surface plane, while l is in the direction perpendicular to the surface. The scattering amplitude is given by the coherent sum of the scattering arising from the bulk and the surface layer.

Using the bulk atomic positions of $DyScO_3$ (Table 2.2), and transforming them to the (110) surface setting, the alternating layered structure, ScO_2^- and DyO^+ planes, is obtained and used as a starting point for the models presented. For simplicity, the atomic positions were fixed and remained at their bulk position in all the presented models. The data are fitted by varying the occupancy of each atomic plane, creating different models like singly or mixed terminated surfaces. It is worth mentioning that in the model a perfect ScO_2 terminated surface results in the same CTRs as a perfect DyO terminated surface. Only when deviations from a singly terminated surface are modeled by, e.g., taking holes or mixed termination into account, the difference between the two terminations can be observed. Both cations and oxygen are contributing to each CTR owing to the symmetry of the $DyScO_3$ unit cell. By scanning reciprocal space with radial scans, no fractional order reflections were observed. This indicates that the surface is (1×1) reconstructed, which is in full agreement with the RHEED measurements.

A selection of CTRs for all four samples is shown in Figure 2.15. Comparing A and R samples with E and RE samples, clear differences were observed. For surfaces after A and R treatment, the data (A open circles, R filled circles) do not match the perfect singly terminated model (dashed curve), while the data of RE and E samples (E open circles, RE filled circles) are close to the perfect singly terminated model.

The data of the chemically roughened surface were fitted with a simple surface model, optimizing the occupancy of the top four atomic planes ($2\times$ ScO_2, $2\times$ DyO), yielding a reasonable fit (black solid line). Adding more layers to the model does not improve the fit significantly. A schematic representation of the fit is shown in Figure 2.8b and the optimized occupancies are listed in Table 2.3. The same model was used to fit the data of A sample, resulting in slightly different occupancies of the four layers. Taking the simplicity of the model into account, the model results in reasonable fits. Using a more sophisticated model, taking into account possible atomic displacements and thermal vibrations other than bulk

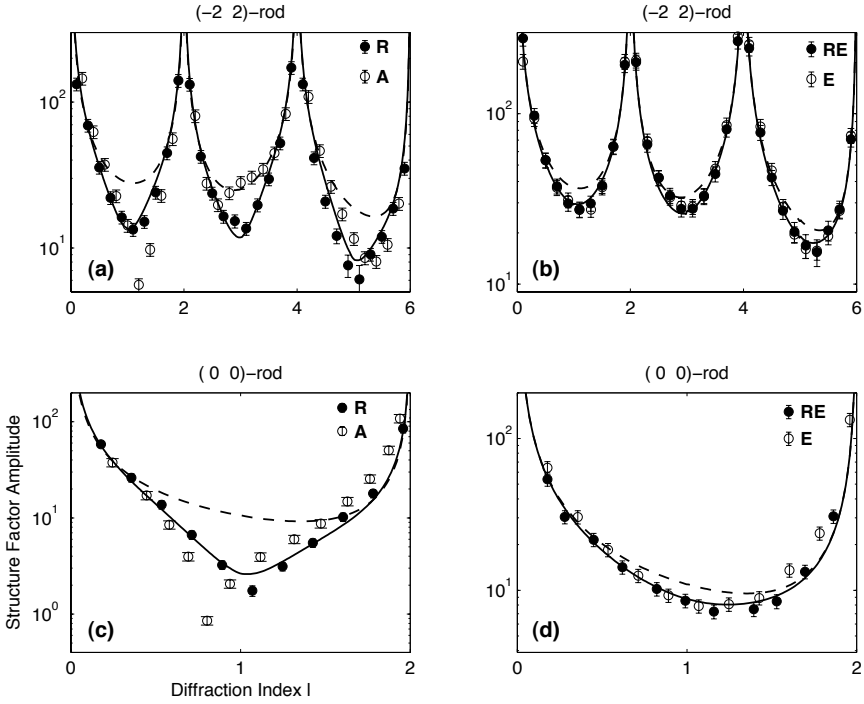

Figure 2.15: The (-2 2) and (0 0) crystal truncation rods of $DyScO_3$ after annealing (A, open circles) and surface roughening (R, filled circles) in (a) and (c) and after selective etching (E, open circles) and both surface roughening and selective etching (RE, filled circles) in (b) and (d). The dashed curves show the fits of a perfect ScO_2 terminated surface. The solid curves are fits to the data of R (a and c) and RE (b and d) treated $DyScO_3$. On the horizontal axis, the diffraction index l and on the vertical axis the structure factor amplitude are given.

values within the top layers, is expected to yield a better fit.[62]

On the other hand, the rods of E and RE (Fig. 2.15b and d) could be well fitted with a perfect ScO_2 terminated surface (dashed line, χ^2=2.9). The fit can be improved by reducing the occupancy of the two topmost planes by 10% (solid black line, χ^2=2.3 for RE). This was in full agreement with their corresponding AFM images showing similar amount of 0.4 nm holes on the step terraces. A schematic representation of this model fit is shown in Figure 2.8c and 2.8d. Increasing the percentage of holes to 20% does not improve the fit (χ^2=2.7) as well as a DyO terminated surface with a 10% reduced occupancy of the two topmost planes (χ^2=2.9). Also modelling a ScO_2 terminated surface with a partially occupied layer of DyO on top, does not yield a better fit (e.g. 5% DyO, χ^2=2.6). The results are listed in Table 2.3.

Using SXRD, it is shown that unreconstructed ScO_2 terminated surfaces were achieved for the E and RE treated samples. There is no indication for a deficiency

Table 2.3: The normalized χ^2 of several models on the different treated $DyScO_3$ surfaces. The occupancies of the top four atomic surface planes are given, where DyO (2) is the most bulk like atomic plane and ScO_2 (1) is the topmost atomic plane. The fits are done by P. Tinnemans, Radboud University in Nijmegen, The Netherlands.

	Occupancy				χ^2
Best model	DyO (2)	ScO_2 (2)	DyO (1)	ScO_2 (1)	
R	0.74	0.60	0.28	0.12	3.6
A	0.91	0.63	0.42	0.36	3.8
E	1.00	1.00	0.90	0.90	2.5
RE	1.00	1.00	0.90	0.90	2.3
Alternative models					
RE	1.00	1.00	1.00	1.00	2.9
RE	1.00	1.00	0.80	0.80	2.7
RE	1.00	1.00	0.05	0.00	2.6
RE	1.00	0.90	0.90	0.00	2.9

of cations at the surface. Due to the relatively low atomic number of oxygen, SXRD is not sufficient to detect possible oxygen vacancies. Moreover, SXRD showed that the surfaces after A and R treatment resulted in mixed terminated and rough surfaces. This is in full agreement with the etching model.

2.4.4 Discussion

SXRD as well as AR-MSRI measurements showed that Sc is the dominant cation at the surface of both E and RE samples. Due to the BHF etching, the RE samples appear to have an increased number of step edges in comparison to E samples. The increased roughness is in agreement with their corresponding AFM height images where unit cell holes were observed.

The RHEED data show (1×1) diffraction patterns for $DyScO_3$ (110), which suggests that surface reconstructions are within the unit cell. The observed four-fold symmetry is also confirmed by AR-MSRI, as it shows clear maxima every 90°. Moreover, the used model to fit the CTRs suggests that cation displacements are negligible. This implies that the cation surface structure is unreconstructed. However, the precise stoichiometry of the surface layer has not yet been determined. The structure is such that vacancies in the surface layer are compatible with (1×1) diffraction patterns. Therefore, ordered cation vacancies are unlikely to occur.

Considering oxygen vacancies at the Sc terminated $DyScO_3$ surface, the total charge reduces. Inserting one oxygen vacancy per orthorhombic unit cell in the topmost atomic plane, the charge of the scandium oxide plane is reduced to $-\frac{1}{2}$. This would be sufficient to overcome the polar discontinuity between bulk $DyScO_3$ and vacuum and may result in (1×1) reconstructed surfaces. Adsorbates are present when $DyScO_3$ is exposed to air and may also play a role in avoiding the polar discontinuity. It has to be mentioned that the used techniques are not suitable to

determine the presence and role of oxygen vacancies and adsorbates at the $DyScO_3$ (110) surface.

2.5 Conclusion

In conclusion, a reliable method is developed for obtaining complete ScO_2 terminated $REScO_3$ by following the framework for controlled selective wet etching of perovskite-type oxides. The pronounced difference in etching rates of REO and ScO_2 in an alkaline solution is used to achieve singly terminated $REScO_3$ surfaces. The influence of the surface morphology on selective wet etching rate is reduced by controlling the morphology by acidic etching. Furthermore, it is shown that the combination of AR-MSRI analysis and $SrRuO_3$ nucleation and growth is a powerful method to determine the termination of perovskite-type surfaces and to verify their complete single termination. This enables studies on new, atomically controlled, heteroepitaxial systems.

RHEED showed an (1×1) diffraction pattern for ScO_2 terminated $DyScO_3$ (110) surfaces. This points to the absence of ordered cation vacancies at the surface. In addition, the SXRD data indicate that cation displacements in relation to the bulk plane are unlikely to be present. Therefore, since surface reconstruction are likely to occur, it is suggested that the polarity difference between bulk and vacuum is overcome by introducing oxygen vacancies in the topmost Sc layer.

In follow-up studies, the wet etching framework can be applied to other complex oxides. In the case of perovskite-type aluminates, e.g., $LaAlO_3$ and $YAlO_3$, the high solubility of Al in acidic as well as in basic solutions can be utilized, resulting in A-site terminated surfaces.

Chapter 3

Amorphous oxide-$SrTiO_3$ heterostructures

Abstract

Conductance confined at the interface of complex oxide heterostructures provides new opportunities to explore nanoelectronic as well as nanoionic devices. Here, it is suggested that redox reactions at the $SrTiO_3$ substrate surface plays an important role on the interfacial properties. Metallic interfaces can be realized in $SrTiO_3$-based heterostructures with various insulating overlayers of amorphous $LaAlO_3$, $SrTiO_3$ and yttria-stabilized zirconia films, while heterostructures with amorphous $La_{7/8}Sr_{1/8}MnO_3$ overlayer remained insulating. The film thickness had a clear influence on the electronic properties of the interface; an abrupt insulator to metal transition was observed when increasing the film thickness above a few nanometer. The exact critical thickness is determined by the overlayer material and the growth pressure. The interfacial conductivity results from the formation of oxygen vacancies near the interface in the $SrTiO_3$ substrate and can be eliminated by performing a post anneal step.[1]

3.1 Introduction

Strontium titanate is a prototype wide band gap insulator with a perovskite structure. Due to the structural compatibility, $SrTiO_3$ has been widely used as a substrate material for the growth of, among others, high temperature superconducting cuprates, colossal magnetoresistive manganites, and multiferroics. Recently, a broad spectrum of interesting properties, such as a quasi-two dimensional electron gas, magnetism, charge writing, resistance switching, giant thermoelectric effect, and colossal ionic conductivity have been observed in various oxide heterostructures based on $SrTiO_3$ substrates.[10, 64–71] These conductance related interfacial properties offer potential applications in oxide electronics, thermoelectric mate-

[1] Parts of this chapter are reprinted with permission from ref. [63], 2011 American Chemical Society.

rials, and solid oxide fuel cells.[72] The origins and the intrinsic mechanisms for these properties have been studied intensively.[73] Many of these properties are observed in heterostructures at the interface between materials with polar atomic planes and neutral atomic planes. For these heterostructures, electronic reconstruction near the interface is suggested to play an important role in determining the interfacial properties.[10, 64] Furthermore, mechanisms such as ion transfer across the interface and formation of defects have been identified as important factors for the transport properties.[65–67, 72, 74–77]

The above mentioned interfacial properties were achieved in crystalline heterostructures. By accident, it was found that interfaces between crystalline $SrTiO_3$ and amorphous oxides can become metallic as well.[63] Interestingly, they showed similar electronic behavior as some crystalline heterostructures. However, electronic reconstruction as well as cation transfer were not expected to occur in these heterostructures, since no polar discontinuity is present at the interface and the fabrication was at room temperature. This makes these heterostructures very suitable for studies on possible other mechanisms that may occur at oxide interfaces. In this chapter, the origin of metallic interfaces between amorphous oxides and crystalline $SrTiO_3$ are discussed in more detail. The focus is mainly on chemical driving forces, leading to compositional changes across the interface.

The first part of the chapter presents the electronic properties of the heterostructures. Clear dependence of oxygen growth pressure, overlayer composition and film thickness were observed. The interface could be tuned from metallic to highly insulating. Secondly, the heterostructures were studied by X-ray photoelectron spectroscopy (XPS). A gradual increase of Ti^{3+} with increase of film thickness was observed, indicating the formation of oxygen vacancies in the $SrTiO_3$. Considering the results shown in this chapter, the chemical reactivity of the plasma species near the $SrTiO_3$ substrate surface appeared to be an important source for the creation of mobile charge carriers in $SrTiO_3$-based oxide heterostructures. Comparable chemical driving forces may also influence the interface behavior of crystalline heterostructures.

3.2 Experimental and Results

3.2.1 Sample growth

$LaAlO_3$, $SrTiO_3$, yttria-stabilized zirconia (Y-ZrO_2) and $La_{7/8}Sr_{1/8}MnO_3$ films were deposited by PLD at room temperature on (001)-oriented TiO_2 terminated $SrTiO_3$, as received $LaAlO_3$ and as received LSAT substrates.[21] To achieve SrO terminated $SrTiO_3$, a monolayer of SrO was deposited by interval (650 °C, 1.3 Jcm^{-2}, 50 Hz, 1×10^{-1} mbar O_2).[78] The amorphous films were grown under an oxygen pressure (P_{O2}) of 1×10^{-6} to 1 mbar by PLD using a KrF laser (λ=248 nm) with a repetition rate of 1 Hz and laser fluence of 1.0-2.0 Jcm^{-2} in both Risø[2] and Twente laboratories. The target to substrate distance was fixed at 4.5 - 5 cm. Commercial $LaAlO_3$, $SrTiO_3$ and Y-ZrO_2 (with 9 mol.% nominal yttria content)

[2]Risø National Laboratory for sustainable energy, Technical University of Denmark.

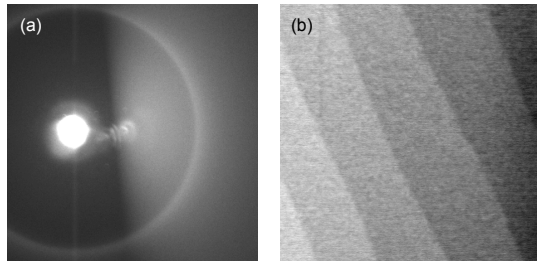

Figure 3.1: (a) RHEED pattern of 5 nm amorphous $SrTiO_3$ grown on $SrTiO_3$ at 10^{-6} mbar and its corresponding AFM height image (b). The height difference between the terraces is approximately 0.4 nm, which corresponds to the height of a single $SrTiO_3$ unit cell. The size of the image is 1×1 μm^2.

single crystals and sintered $La_{7/8}Sr_{1/8}MnO_3$ ceramics were used as targets. The used growth conditions are similar to the ones commonly used in the literature except for the ambient deposition temperature and the variable oxygen pressure. At room temperature, the deposited films are expected to be amorphous and any oxygen exchange between the substrate and the background gas is significantly suppressed. Using RHEED and X-ray diffraction (XRD), no crystalline structure could be determined (see Fig. 3.1a). In this chapter, the structure of these films will be further named amorphous.[3] The morphology of the films was a copy of the substrate surface morphology, resulting in smooth film surfaces (see Figure 3.1b). The film thickness was determined by AFM through patterning the samples prior to deposition or by X-ray reflectivity measurements (XRR).

3.2.2 Scanning transmission electron microscopy

To study intermixing effects at the interface, amorphous $LaAlO_3$ and $SrTiO_3$ films on $SrTiO_3$ were studied by scanning transmission electron microscopy (STEM). With STEM, an image was obtained from the high angle annular dark field (HAADF) intensity measurements, while the spectrum of the low angle electrons can be measured for additional chemical information (electron energy loss spectroscopy, EELS). The STEM data were measured with a FEI Titan microscope in Antwerp, Belgium.

Clear lattice fringes have been observed in the $SrTiO_3$ substrate, while they were absent in the amorphous $LaAlO_3$ layer. This is shown in Figure 3.2a. The lack of fringes confirms the amorphous state of the film, which was suggested by diffraction measurements. The HAADF-STEM image shows clear contrast at the $LaAlO_3$-$SrTiO_3$ interface. Using STEM-EELS, the interface appeared to be atomically sharp without significant intermixing (see Figure 3.2b). This is different

[3] An amorphous material may have a high degree of short range order, but long range ordering is absent. As a result, the amorphous structure does not have an essential discrete diffraction pattern.

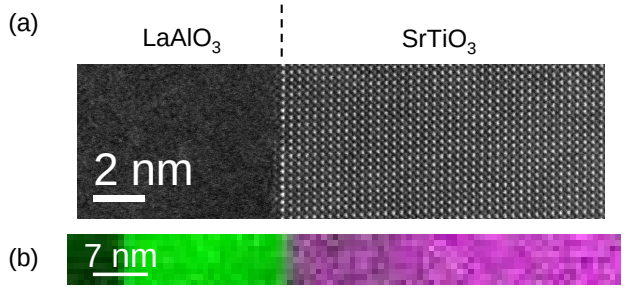

Figure 3.2: (a) HAADF-STEM image of amorphous $LaAlO_3$ on $SrTiO_3$. (b) STEM-EELS image, where La is green and Ti is purple.

from with crystalline $LaAlO_3$-$SrTiO_3$ interfaces, for which significant intermixing near the interface has been observed.[13, 79, 80]

During the exposure of $LaAlO_3$-$SrTiO_3$ to the high energetic e-beam, a bright crystalline layer of one unit cell thick was formed at the $LaAlO_3$-$SrTiO_3$ interface. It appeared that the composition of this monolayer was $LaTiO_3$ like and epitaxial. This suggests that the high energetic beam induced crystallization of the amorphous film. Note that a much higher dose was needed to form a second layer. For $SrTiO_3$-$SrTiO_3$ heterostructures, however, e-beam irradiation induced out-of-plane film crystallization over a larger area, even up to $\sim$ 20 nm.

3.2.3 Electronic properties

The sheet resistance and carrier density of the buried interfaces were measured using a 4-probe Van der Pauw method with ultrasonically wire-bonded aluminum wires as electrodes. The temperature dependent electrical transport and Hall-effect measurements were performed in a Quantum Design physical properties measurement system (PPMS) in the temperature range from 300 K down to 2 K with magnetic fields up to 14 T.

The $LaAlO_3$-$SrTiO_3$, $SrTiO_3$-$SrTiO_3$, and Y-ZrO_2-$SrTiO_3$ heterostructures exhibit conducting metallic behavior (see Fig. 3.3a). In contrast to several crystalline interfaces, the conductivity appeared to be independent of the $SrTiO_3$ surface termination, as shown in Figure 3.4.[10] In this chapter, further results achieved for heterostructures on $SrTiO_3$ are based on TiO_2 terminated $SrTiO_3$ substrate surfaces.

The heterostructures grown on both $LaAlO_3$ and LSAT substrates were highly insulating. These results indicate that the deposited films are insulating and that the metallic behavior is closely related to the $SrTiO_3$ substrate. For the conducting samples, Hall-effect measurements showed that the charge carriers at the interface were electron type, i.e. n-type (see Fig. 3.5). The obtained sheet carrier density, n_s, of Risø grown samples was nearly constant in the temperature range of 100-300 K with a value of (0.8-1.2)$\times 10^{14}$ cm^{-2} (Fig. 3.3b) and decreased gra-

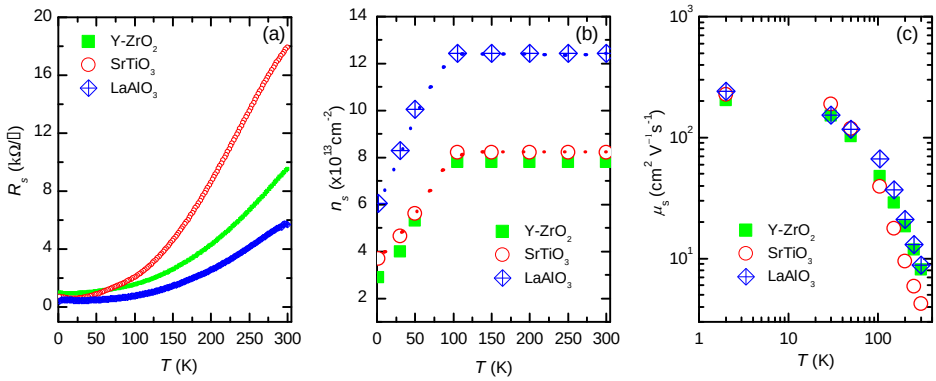

Figure 3.3: The sheet resistance (a), sheet carrier density (b) and the electron mobility (c) versus temperature of 8 nm amorphous films of $LaAlO_3$, $SrTiO_3$, and Y-ZrO_2 grown on $SrTiO_3$ substrates at 1×10^{-6} mbar of O_2. These heterostructures were grown in Risø. The dotted line in (b) is a guide to the eye.

dually with decreasing temperature below 100 K. At temperatures below 30 K, the Hall resistance became nonlinear with respect to magnetic fields (see Fig. 3.5). At 2 K, n_s reached a value around 5×10^{13} cm^{-2}. Note that the constant n_s above 100 K was not observed for the heterostructures fabricated in Twente (see Fig. 3.4). These samples showed a typical thermally activated behavior of the carrier density.[78] It is interesting to mention that $SrTiO_3$ has a structural phase transition around 100 K.[81]

The electron mobility, μ_s, increased upon cooling to 200 cm^{2}V^{-1}s^{-1} at 2 K for Risø samples (Fig. 3.3c). The observed electron mobility for the heterostructures grown in Twente was slightly higher at low temperatures, between 200 and 800 cm^{2}V^{-1}s^{-1}. The observed variation in mobility between samples could not be clearly linked to the film thickness and film composition.

The interfacial conductivity of the amorphous oxide-$SrTiO_3$ heterostructures exhibited strong dependence on the P_{O_2} during film growth. All heterointerfaces grown at $P_{O_2} > 1\times10^{-2}$ mbar were insulating ($R_s > 10^9$ Ω/□, measurement limit) (see Figs. 3.6a and b). Upon decreasing the pressure below 1×10^{-2} mbar, the heterointerfaces of $LaAlO_3$-$SrTiO_3$, $SrTiO_3$-$SrTiO_3$, and Y-ZrO_2-$SrTiO_3$ turned conductive, whereas $La_{7/8}Sr_{1/8}MnO_3$-$SrTiO_3$ remained insulating. In Figure 3.6, the electronic properties at room temperature are shown. It is also important to mention that the temperature behavior of the sheet resistance varies between the different heterostructures. A simple metallic behavior was observed in the $SrTiO_3$-$SrTiO_3$ and Y-ZrO_2-$SrTiO_3$ heterostructures grown at 1×10^{-3} mbar. The $LaAlO_3$-$SrTiO_3$ heterostructures, grown between 10^{-3} and 10^{-4} mbar, showed a more semiconducting behavior. Decreasing the P_{O_2} further, $LaAlO_3$-$SrTiO_3$ showed a simple metallic behavior as well.[63]

More remarkable, an interfacial metal-insulator transition that depends on the

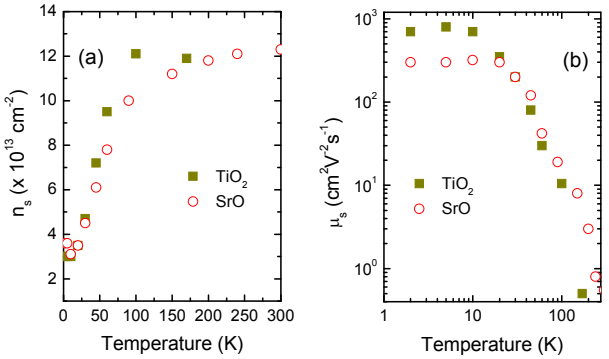

Figure 3.4: Sheet carrier density (a) and electron mobility (b) versus temperature of 2.4 nm amorphous $LaAlO_3$ films on TiO_2 and SrO terminated $SrTiO_3$ grown in Twente at 10^{-6} mbar.

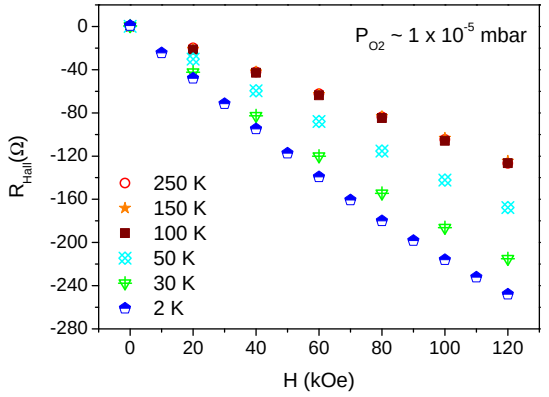

Figure 3.5: The measured Hall resistance at different temperatures of a typical $LaAlO_3$-$SrTiO_3$ sample deposited at P_{O_2} of $1{\times}10^{-5}$ mbar in Risø laboratory. The thickness of the film is approximately 26 nm.

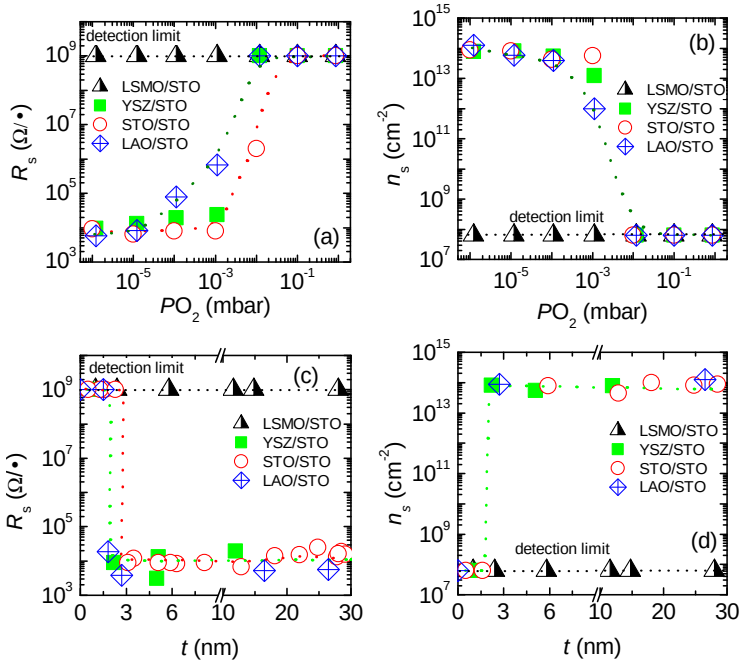

Figure 3.6: The sheet resistance (a) and carrier density (b) versus oxygen pressure for $LaAlO_3$, $SrTiO_3$, Y-ZrO_2 and $La_{7/8}Sr_{1/8}MnO_3$ films grown on $SrTiO_3$. The film thickness is around 30 nm. The sheet resistance (c) and carrier density (d) versus film thickness for amorphous heterostructures grown at P_{O_2} of 1×10^{-6} mbar. All measurements were done at room temperature. The dotted lines are a guide to the eye.

thickness of the amorphous film was observed in these heterostructures. Similar metal-insulator transitions have been observed for crystalline heterostructures with a polar discontinuity at the interface.[64, 71, 82] As shown in Figures 3.6c and d, the amorphous oxide-$SrTiO_3$ heterointerfaces, fabricated at P_{O_2} of 1×10^{-6} mbar, were insulating at a thickness (t) < 1.8 nm for $LaAlO_3$-$SrTiO_3$, $t < 2.2$ nm for Y-ZrO_2-$SrTiO_3$, and $t < 2.8$ nm for $SrTiO_3$-$SrTiO_3$, respectively. Astonishingly, the heterointerfaces abruptly became metallic above these film thickness. No semiconducting state was observed for intermediate film thicknesses. The electronic properties of the interface remained constant with further increase of the film thickness. The critical thickness for the occurrence of conductivity may also increase upon increasing P_{O_2}, as observed for $LaAlO_3$-$SrTiO_3$. The critical thickness is increased to ~ 5.4 nm, when growing $LaAlO_3$ at 10^{-4} mbar O_2. In contrast to the heterostructures described above, the heterostructures with $La_{7/8}Sr_{1/8}MnO_3$ remained insulating, independent of film thickness and growth pressure.

The oxygen pressure had a clear influence on the electronic properties of the interface. Therefore, a series of $LaAlO_3$ films on $SrTiO_3$ was also grown at different argon pressures and compared with $LaAlO_3$ films grown in oxygen. The results

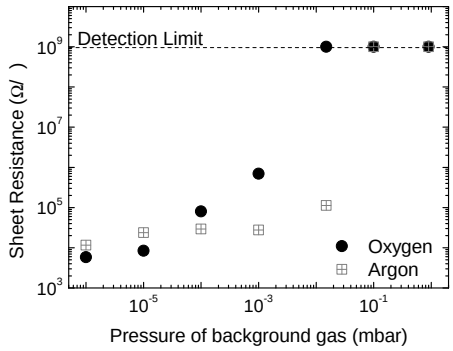

Figure 3.7: The sheet resistance of $LaAlO_3$-$SrTiO_3$ heterostructures grown at different pressures with oxygen or argon as the background gas. The data were measured at room temperature.

are shown in Figure 3.7. A clear difference between the 10^{-2} mbar grown samples was observed. At this pressure, all films grown in oxygen were insulating, where the film grown in argon was still clearly conducting. Increasing the Ar pressure to 10^{-1} mbar resulted in insulating heterostructures.

3.2.4 X-ray photoelectron spectroscopy

To determine the origin of the interfacial conductivity, *in situ* angular resolved XPS measurements were performed. A series of samples were transferred after growth to an XPS chamber while keeping them under high vacuum (below 1×10^{-9} mbar). The XPS chamber (Omicron Nanotechnology GmbH) had a base pressure below 1×10^{-10} mbar. The measurements were done using a monochromatic Al Kα (XM 1000) X-ray source and an EA 125 electron energy analyzer. All spectra were acquired in the Constant Analyzer Energy (CAE) mode. The escape angle of the electrons was varied by rotation of the sample between 15 to 80 degrees with respect to the analyzer normal. The analyzer was calibrated with the use of an *in situ* sputter cleaned Au sample. A CN 10 charge neutralizer system was used to overcome the charging effect in the $La_{7/8}Sr_{1/8}MnO_3$-$SrTiO_3$ heterostructures. For each measurement the filament current, emission current and beam energy were optimized to minimize the full width at half maximum (FWHM) of the peaks. For analyzing the Ti $2p_{3/2}$ peaks, a Shirley background was subtracted and the spectra were normalized on the total area below the Ti peaks ($[Ti] = [Ti^{4+}] + [Ti^{3+}] = 100\%$). The Ti $2p_{3/2}$ spectra were fitted by two Voigt functions. The peak shape and peak seperation were fixed and the area was optimized for each sample. All spectra were calibrated to O $1s$ at 530.1 eV.

Figures 3.8a and b show the Ti $2p_{3/2}$ spectra for different film thicknesses of $LaAlO_3$-$SrTiO_3$ and Y-ZrO_2-$SrTiO_3$ samples, respectively. All samples were grown at P_{O_2} $\sim1\times10^{-6}$ mbar. For $SrTiO_3$-$SrTiO_3$, the broad Ti core-level spectra of the amorphous $SrTiO_3$ film obscured the details of the $SrTiO_3$ substrate. As

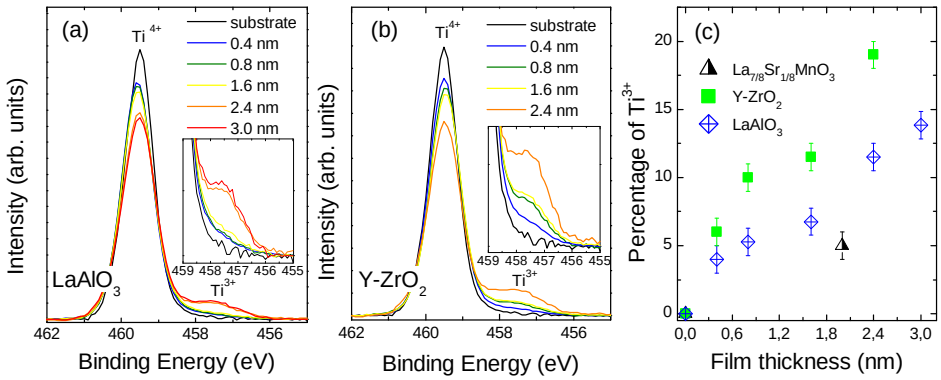

Figure 3.8: (a) and (b) The Ti $2p_{3/2}$ XPS spectra for different film thicknesses of amorphous $LaAlO_3$-$SrTiO_3$ and Y-ZrO_2-$SrTiO_3$, respectively. The insets show a close-up of the Ti^{3+} peak. All films were grown at P_{O_2} 1×10^{-6} mbar. The spectra were measured at an emission angle of 80°. (c) The film thickness versus percentage of Ti^{3+} for $LaAlO_3$-$SrTiO_3$, Y-ZrO_2-$SrTiO_3$ and $La_{7/8}Sr_{1/8}MnO_3$-$SrTiO_3$ samples, where $[Ti^{3+}]$ + $[Ti^{4+}]$ = 100%.

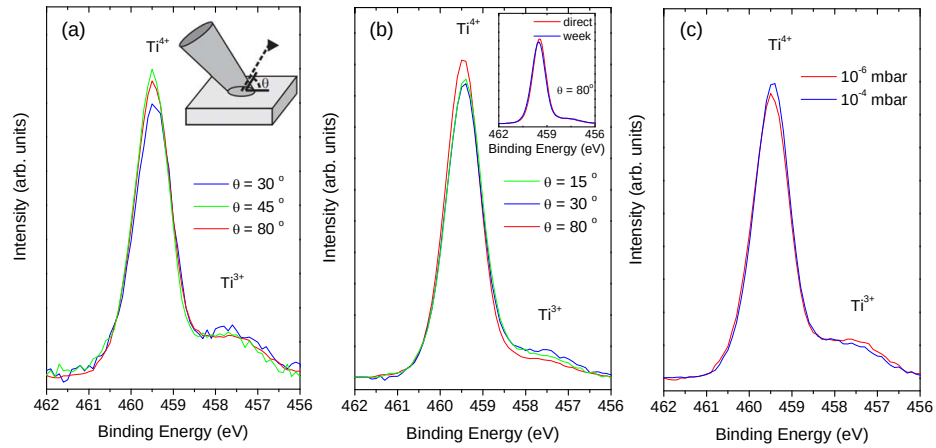

Figure 3.9: (a) and (b) Angle resolved XPS spectra of Ti $2p_{3/2}$ for 2.4 nm and 0.8 nm Y-ZrO_2 films on $SrTiO_3$, respectively, grown at 1×10^{-6} mbar. The inset of (a) shows how the emission angle, θ, is defined. The inset of (b) shows the differences in spectra of the 0.8 nm Y-ZrO_2 film over time of one week. (c) The Ti $2p_{3/2}$ peak for two 2.4 nm films of Y-ZrO_2 on $SrTiO_3$, grown at different oxygen pressures.

shown in Figures 3.8a and b, no clear Ti^{3+} signal in the $2p_{3/2}$ core-level spectra could be detected in the bare $SrTiO_3$ substrate, as expected. However, finite amount of Ti^{3+} is already present in the insulating samples, even at a film thickness of ∼0.4 nm. This suggests the formation of defects in $SrTiO_3$, either by intermixing or by oxygen vacancies.[83] The amount of Ti^{3+} increased with increasing film thickness, as shown in Figure 3.8c. This result, which is difficult to explain by intermixing, may indicate the evolution of oxygen vacancies in $SrTiO_3$ substrates upon film deposition. Note that the amount of Ti^{3+} is stable over time after film deposition (inset Fig. 3.9b), which strongly indicates that the formation of oxygen vacancies only occured during film deposition. Additionally, in contrast to the negligible difference in the measured conductivity at room temperature, a distinct higher concentration of Ti^{3+} is present in Y-ZrO_2-$SrTiO_3$ compared to $LaAlO_3$-$SrTiO_3$ (Figure 3.8c). Moreover, the critical thickness of $LaAlO_3$-$SrTiO_3$ is lower than that of Y-ZrO_2-$SrTiO_3$. This indicates that the concentration of Ti^{3+} is not directly proportional to the conductivity.

For Ti^{3+} depth profiling, angular resolved XPS measurements were performed. No clear angle dependence of the Ti^{3+} signal was observed, independent of the film thickness (Fig. 3.9a and b). This indicates that Ti^{3+} extend at least several nanometers deep into the $SrTiO_3$ substrate. These results are different from the results of crystalline $LaAlO_3$-$SrTiO_3$, for which a clear angle dependence of the Ti^{3+} signal has been reported.[84] Additionally, the effect of P_{O_2} on the concentration of Ti^{3+} was investigated in Y-ZrO_2-$SrTiO_3$. Only small differences in the Ti^{3+} signal were observed between heterostructures grown at 1×10^{-6} mbar $< P_{O_2} < 1\times10^{-3}$ mbar (Fig. 3.9c). This is consistent with the transport measurements as shown in Figures 3.6a and b.

To verify whether the presence of Ti^{3+} is caused by oxygen vacancies, a $LaAlO_3$ film of 2 nm was post annealed at 0.6 bar oxygen and 150 °C for 90 minutes. In Figure 3.10, the Ti $2p$ spectra before and after post annealing are shown. Before post annealing, a clear Ti^{3+} signal is present (11±1 %). On the other hand, the Ti^{3+} signal became negligible after post annealing (2±1 %). This suggests oxygen from the background gas diffused into the substrate. After post annealing, all samples became insulating. The required time to refill the $SrTiO_3$ with oxygen depended on the thickness of the film and the annealing temperature. A thick $LaAlO_3$ film was measured by X-ray diffraction after post annealing at 300 °C. In the θ-2θ scan, no film peaks were observed, which suggests that the $LaAlO_3$ film remained amorphous after post annealing.

In short, the XPS results suggest that the interfacial conductivity in amorphous oxide-$SrTiO_3$ heterostructures should be mainly ascribed to oxygen vacancies on the $SrTiO_3$ substrate side. This is also consistent with the clearly reduced amount of Ti^{3+} in the $La_{7/8}Sr_{1/8}MnO_3$-$SrTiO_3$ heterostructure compared to $LaAlO_3$ and Y-ZrO_2 on $SrTiO_3$ (Figure 3.8c).

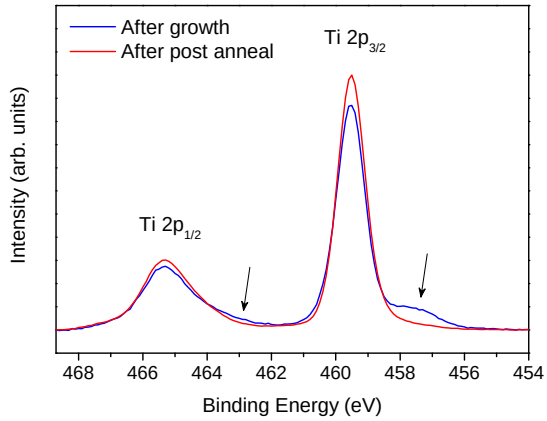

Figure 3.10: XPS Ti 2*p* spectra of a 2 nm $LaAlO_3$ film grown on $SrTiO_3$, directly after growth and after post annealing. The arrows point to the Ti^{3+} signal. The increased spectral weight around 460-461 *e*V of the sample after post annealing originate from the Ti^{3+} satellite.

3.3 Discussion

Based on aforementioned results, the oxygen pressure during film growth turned out to be the main factor that controls the interfacial conduction. In a PLD process, the pressure determines the expansion dynamics of the plume and the composition of the plasma.[85] In the pressure range of $P_{O_2}<1\times10^{-2}$ mbar, the PLD plasma expands freely and consists of a large fraction of energetic atomic neutrals and a small fraction (in the range of 1% - 5%) of ions, with energies between tens and hundreds of *e*V.[85, 86] This is also the pressure range in which interfacial conduction is mainly observed. Increasing the pressure to $P_{O_2}>1\times10^{-2}$ mbar generally results in collisions between the plasma plume and the background gas, leading to a much lower energy for the plasma species.[85] The plasma species are thermalized and oxidized before arriving at the substrate.[85, 86] In this high oxygen pressure regime, the interfacial conductivity became negligible. This suggests the P_{O_2} dependence of the plasma properties and the interfacial conduction exhibit close correspondence. Consequently, two scenarios should be considered for the interfacial conductivity: first, the impinging of the high energetic plasma species into the substrate, and second, the chemical reactivity of the plasma species with respect to the $SrTiO_3$ substrate.

The first scenario, defect creation by exposure of the $SrTiO_3$ surface to the high energy of the impinging plasma species is similar to the Ar^+ irradiation induced conductivity in $SrTiO_3$.[76, 77, 87, 88] When ions impinge on the substrate surface, the energy loss is typically of several hundreds of *e*V per nm. As a consequence, the penetration length of the PLD plasma should be much lower than 1 nm, comparable to Ar^+ irradiation at 100 *e*V.[88] When the thickness of the grown film is larger than 1 nm, the bombarding effect on $SrTiO_3$ substrates should become

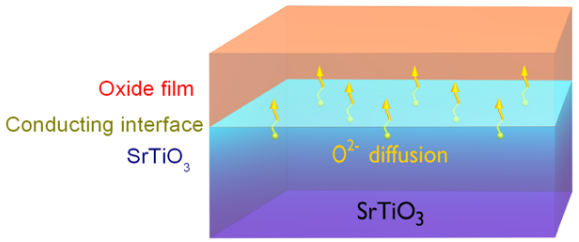

Figure 3.11: Schematic representation for the oxygen ions outward diffusion induced interfacial conduction in $SrTiO_3$-based heterostructures during growth of the oxide films at room temperature.

negligible. Therefore, the sputtering effect with possible cation intermixing involved is especially a concern during deposition of the first (mono)layer of the film. Since interfacial conductivity was observed for larger film thicknesses, it is expected that the sputtering effect has a much smaller contribution to the conductivity than the chemical effect described below. Moreover, the sputtering scenario is not compatible with the gradual increase of the density of oxygen vacancies in $SrTiO_3$ substrate upon increasing film thickness as shown in Figure 3.8c. Additionally, with the assumption of a similar kinetic distribution of plasma species when ablating different oxides, a sputtering scenario is not consistent with the insulating interfaces between $SrTiO_3$ substrates and amorphous $La_{7/8}Sr_{1/8}MnO_3$ films. Finally, the STEM-EELS data of amorphous $LaAlO_3$ on $SrTiO_3$ showed nearly no La intermixing in the $SrTiO_3$ (see section 3.2.2). This indicates that cation intermixing due to sputtering is not the main origin of the conducting interface.

In the second scenario, taking the chemical reactivity of the plasma into account, the deposited species may react with the oxygen anions (O^{2-}) present in the $SrTiO_3$ substrate lattice. In this case, besides the oxygen source from the target and the background oxygen gas, the oxygen ions in $SrTiO_3$ substrates most likely diffuse outward to oxidize the reactive plasma species adsorbed on the $SrTiO_3$ substrate surface. This is schematically depicted in Figure 3.11. Similar to this, outward diffusion of oxygen ions from the $SrTiO_3$ substrate has been observed during the growth of reactive metals of Ti and Y films by molecular beam epitaxy under ultrahigh vacuum.[89] Here, it is suggested that the oxygen vacancies and the resulting interfacial conductivity may be induced from redox reactions at the interface: reducing the $SrTiO_3$ substrate surface to oxidize the oxygen-deficient overlayer.

The chemical interactions at the interface between a metal and the TiO_2 or $SrTiO_3$ substrate surface are controlled not only by the thermodynamic stability of the metal oxide, but also by the space charges at the metal-oxide interface. The space charges are determined by the electronic configuration at the interface, i.e. the relative Fermi level of the metal and that of the TiO_2 or $SrTiO_3$ before

contact.[90, 91] An interfacial redox reaction[4] with TiO_2 can occur at room temperature when the heat of metal oxide formation per mole of oxygen, $\Delta {H_f}^O$, is lower than -250 kJ/(mol O) and the work function of the metals, φ, is in the range of 3.75 eV $< \varphi <$ 5.0 eV.[90] The heat of metal oxide formation and the work function of several metals are shown in Figure 3.12.

Interestingly, for the conducting heterostructures, one of the main neutral species in each freely expanding plume (Al, Ti, and Zr) follows the above criterion, with a highly negative $\Delta {H_f}^O$. Moreover, conducting interfaces between amorphous $CaHfO_3$ and $SrTiO_3$ substrates have been reported.[87, 92] According to Figure 3.12, Hf fits the criteria for occurrence of the redox reaction with TiO_2 as well. Mn is one of the main atomic species of the corresponding $La_{7/8}Sr_{1/8}MnO_3$ plasma and fits the criterea for a redox reaction with TiO_2 as well, but results in insulating heterostructures on $SrTiO_3$.[93, 94] However, for redox reactions with $SrTiO_3$, it has been shown that temperature is an important parameter for the occurrance/non-occurance of redox reactions. For example, Cr reacts with $SrTiO_3$ above 640 °C, while Al oxidizes already at room temperature.[91] For metals with an relatively high φ or less negative $\Delta {H_f}^O$, the temperature has to be increased above room temperature to result in an interfacial redox reaction between metal and $SrTiO_3$.[91, 93] So far, the focus was on the B-site atoms. However, the influence of, e.g., La is expected to be minimal as $LaBO_3$-$SrTiO_3$ interfaces could become conducting or remained insulating. Furthermore, it has been observed that La ions in the plasma are already partially oxidized during ablation at 10^{-3} mbar oxygen.[95] The partial oxidation may suppress redox reactions between La and $SrTiO_3$. The redox reactions at the interface between complex oxides are more complicated than those at simple oxide interfaces. Nevertheless, the lack of redox reactions at the interface of the $La_{7/8}Sr_{1/8}MnO_3$-$SrTiO_3$ samples, as a result of a less negative $\Delta {H_f}^O$, can explain their insulating states.

The scenario that takes the chemical reactivity of the plasma into account is also supported by the data of the $LaAlO_3$ films grown in argon (see Fig. 3.7). During deposition in argon, the reactive species in the plasma can only be oxidized by the oxygen in the plasma before arriving on the substrate. Apparently, the collisions between the species and the oxygen in the plasma is still sufficiently low at 10^{-2} mbar. Therefore, most species are expected to be metallic when arriving at the $SrTiO_3$ substrate. As a result, redox reactions between the plasma species and the $SrTiO_3$ surface can occur and, consequently, oxygen diffuses from the $SrTiO_3$ to the amorphous film. The interface may become conducting. The increase of collisions in the plasma at 10^{-1} mbar results in an increase of oxidized plasma species. The heterostructures remain insulating. Growing films in oxygen, the interaction between plasma species and oxygen background gas is expected to be sufficient to oxidize the plasma species already at 10^{-2} mbar. In addition, oxygen exchange between film and background gas may occur. This results in insulating heterostructures grown at 10^{-2} mbar oxygen.

It is important to note that the chemical reactivity scenario also clarifies the observed differences in electronic behavior between the heterostructures described

[4]Interfacial redox reaction: $Me^I \parallel Me^{II}O_x \rightarrow Me^IO_y \parallel Me^{II}O_{x-y}$

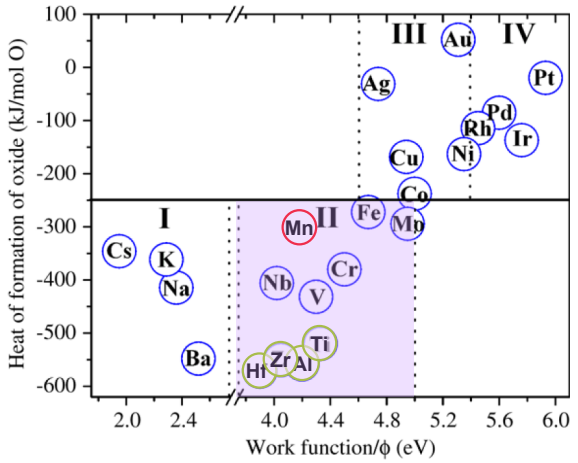

Figure 3.12: The dependence of the heat of metal oxides formation versus the work function of metals. The area where interfacial redox reaction may occur is yellow colored. Interfacial conductivity is experimentally shown for amorphous films with the elements that are marked green. The elements that experimentally resulted in insulating interfaces are marked red. This Figure has been reproduced with permission from ref. [90].

here and the ones described by Schneider *et al.*.[96] Schneider *et al.* achieved insulating heterostructures by depositing amorphous $LaAlO_3$ on $SrTiO_3$ capped with two monolayers of crystalline $LaAlO_3$. As a result, possible redox reactions between the $SrTiO_3$ surface and the amorphous $LaAlO_3$ were suppressed by the crystalline $LaAlO_3$ layer.

It should be mentioned that a possible sputtering effect, which is especially a concern during the deposition of the first (mono)layer, cannot enable conductivity directly at larger film thicknesses, but could facilitate or enhance the oxygen outward diffusion leading to interfacial conductivity.

3.4 Conclusion and Outlook

It has been shown that the chemical composition of the PLD plasma affects the electronic properties of amorphous oxide-$SrTiO_3$ heterostructures by introducing oxygen vacancies near the $SrTiO_3$ substrate surface. The results indicate that, besides electronic interactions, chemical reactions at the interface play an important role in determining interfacial conductivity. Moreover, the results show that a film thickness dependent transport behavior in oxide heterostructures does not have to be solely induced by intrinsic electronic reconstruction.

Similar chemical reactions are expected to occur during low pressure growth of oxide heterostructures at high temperatures. However, no solid conclusions on interfacial reconstructions of crystalline heterostructures can be made, as, e.g., oxygen vacancies are mobile at high temperatures. At high temperatures, the

interaction between background gas and substrate are significant. As a result, the interfacial behavior of crystalline heterostructures depends also on the cool-down procedure.

The easy room temperature fabrication of highly conductive interfaces of complex oxide heterostructures is promising for the application in both oxide electronics and thermoelectric oxides. Furthermore, the chemical reactivity of $SrTiO_3$ can be exploited to determine the oxygen affinity of the film material at room temperature. Variations in Ti^{3+} formation between different elements appeared to give a distinct indication for the oxygen affinity.

For further understanding of these amorphous oxide-$SrTiO_3$ interfaces, several follow-up studies are proposed. First of all, amorphous films, containing Na or Ni, on $SrTiO_3$ should be studied. Insulating behavior of these heterostructures would verify the redox reaction mechanism. Secondly, the two dimensionality of the conducting layer and its thickness have to be determined. This is possible by performing Hall measurements both parallel and perpendicular to the magnetic field. Moreover, it would be interesting to study the suggested oxygen transfer in more detail and to resolve the thickness of oxygen depleted $SrTiO_3$. It has been shown that dynamic secondary ion mass spectroscopy (SIMS) depth profiling may give information on the oxygen transfer and the oxygen balance.[97] Therefore, samples consisting ^{18}O exchanged $SrTiO_3$ substrates with an amorphous film deposited in ^{16}O can be studied. Distinct differences in the oxygen depth profile are expected between insulating and conducting heterostructures. Furthermore, an oxygen depth profile of an in ^{16}O post annealed sample may give information on the oxygen indiffusion during post annealing. Note that the accuracy of dynamic SIMS depth profiling is approximately 5 nm.

Chapter 4

$LaAlO_3$ - $SrTiO_3$ heterostructures

Abstract

The conducting interface between two wide band gap insulators, $LaAlO_3$ and $SrTiO_3$, has attracted a lot of interest. However, no unified picture can be drawn to clarify the experimental results. Up to now, many studies have been focused on the $LaAlO_3$ layer and its surface, but the conducting layer is in the $SrTiO_3$. Therefore, in this chapter, the influence of the $SrTiO_3$ template on the electronic behavior has been investigated. Varying strain, octahedral rotations and $SrTiO_3$ defect density, the interface was tuned from metallic to insulating. On $SrTiO_3$ and (La,Sr)(Al,Ta)O_3, the $LaAlO_3$-$SrTiO_3$ interface could become metallic, while the interface remained insulating on $DyScO_3$ and $NdGaO_3$. Furthermore, the electronic behavior strongly depended on the oxygen growth pressure. The metallic interface on $SrTiO_3$ was canceled out by introducing a grown $SrTiO_3$ layer with a lower oxygen vacancy concentration than a $SrTiO_3$ single crystal. The shown results suggest that both oxygen vacancies and specific octahedral rotations have to be present in the $SrTiO_3$ near the interface to achieve conductivity.

4.1 Introduction

Chemical driving forces at oxide interfaces can result in interesting properties near the interface, as discussed in the previous chapter.[63] At crystalline oxide heterointerfaces, the influence of chemical reactions is expected to be even more complex. Moreover, electronic, ionic and structural reconstructions have to be taken into account for the understanding of these heterointerfaces. For some crystalline heterostructures, also the precise atomic stacking of the interface appeared to be crucial to control the physical behavior near the interface.[10] Such crystalline heterostructures are discussed in this chapter and electronic, ionic and structural reconstructions are considered.

Recently, Ohtomo and Hwang have shown that the electronic behavior of the interface between two wide band gap insulating perovskite-type oxides, $SrTiO_3$

(3.2 eV) and $LaAlO_3$ (5.6 eV), strongly depends on the atomic stacking of the interface: TiO_2-SrO-AlO_2-LaO (p-type) remains insulating, while SrO-TiO_2-LaO-AlO_2 (n-type) shows metallic behavior near the interface.[10] The initial explanation to describe this phenomenon was focused on intrinsic electronic reconstruction at the interface. $SrTiO_3$ consists of alternating SrO and TiO_2 planes along the [001] direction. Both atomic planes are charge neutral. On the other hand, $LaAlO_3$ consists of positively (LaO^+) and negatively (AlO_2^-) charged planes. When $LaAlO_3$ is grown on top of $SrTiO_3$, a polar discontinuity exhibits at the interface.[10] With increase of $LaAlO_3$ thickness, a potential build-up is created due to the electric fields between the oppositely charged layers in $LaAlO_3$. This has to be compensated when the energy can not longer be accommodated by internal deformations: when the potential build-up becomes larger in energy than the band gap of $SrTiO_3$. As a result, the valence band of $LaAlO_3$ crosses the Fermi level and electrons from the $LaAlO_3$ surface can be transfered to the $SrTiO_3$ conduction band.

In a purely ionic model, the divergence can be removed by transferring half an electron (hole) per unit cell area across the LaO-TiO_2 (AlO_2-SrO) interface from $LaAlO_3$ to $SrTiO_3$. For the n-type interface (TiO_2^0-LaO^+), an electron can easily be transferred to the Ti $3d$ conduction band, resulting in Ti^{3+}. The interface is electronically reconstructed and the extra electron would result in conductivity at the n-type interface. Hall measurements have shown that the conductivity is indeed electron like.[10] At the p-type interface (SrO^0-AlO_2^-), both cations have a closed shell, thus intrinsic hole doping is unexpected. To avoid the divergence of the electrostatic potential, oxygen vacancies are suggested to form in the SrO layer.[13] As a result, intrinsic hole doping is suppressed and, therefore, no conductivity is observed at the p-type interface.

Below, the main experimental observations for $LaAlO_3$-$SrTiO_3$ heterostructures are pointed out.

- The electronic behavior depends on the atomic stacking; SrO-AlO_2 is insulating, TiO_2-LaO is conducting.[10]
- A minimum of four monolayers of $LaAlO_3$ is necessary to achieve metallic interfaces.[82]
- The electronic behavior strongly depends on the PLD growth parameters: oxygen pressure and cool-down procedure. The electronic properties of films grown at $\leq 10^{-5}$ mbar without post-annealing are dominated by oxygen vacancies in the $SrTiO_3$. Conductivity confined at the interface is observed in samples after post annealing or grown at 10^{-4}-10^{-3} mbar. Growing at 10^{-1} mbar results in insulating heterostructures, independent of the atomic stacking at the interface.[66, 77]
- In well oxidized samples, the sheet carrier density is $\sim 2\times 10^{13}$ cm^{-2} at 2 K ($\approx$0.03 electron per two dimensional interface unit cell) and is thermally activated.[76–78, 82, 98] Furthermore, the sheet carrier density is independent of the $LaAlO_3$ thickness ($\geq$ 4 unit cells).[82]
- The conducting layer is in $SrTiO_3$ near the interface and is confined within a few nanometers of the interface.[84, 98–101]

According to the intrinsic electronic reconstruction model, crossing of the potential build-up and the band gap is expected to occur at four monolayers of $LaAlO_3$. This value is in agreement with the observed critical thickness.[82] To compensate the potential build-up, half an electron per two-dimensional interface unit cell was suggested to cancel the internal electric field through the $LaAlO_3$ layer completely for the *n*-type interface. This would be equivalent to a sheet carrier density of 3.3×10^{14} cm^{-2} if all electrons became mobile. However, this value is far above the measured carrier density at low temperatures.[76–78, 82, 98] This suggests that a part of the transferred electrons are immobile.

The suggested divergence in $LaAlO_3$ should be able to measure by XPS. The divergence of the $LaAlO_3$ bands towards the Fermi level would result in asymmetric broadening of the La and Al peaks in the XPS spectra. Experimentally, broadening appeared to be absent independent of the $LaAlO_3$ thickness.[11, 102] In addition, the Ti^{3+} concentration, measured by XPS, was much lower than the predicted 0.5 e^- per two dimensional interface unit cell.[84, 103]

The absence of the potential build-up suggests that additional mechanisms play a role on the interfacial behavior. First of all, oxygen vacancies in $SrTiO_3$ are suggested to be created during film growth by sputtering of high energy La ions.[76, 77, 100] This would result in a conducting $SrTiO_3$ layer near the interface. In spite of the fact that it may clarify conductivity near the interface, this mechanism does not explain the termination dependence and critical thickness.

Secondly, cation intermixing, La with Sr or Al with Ti, has been suggested to avoid the polar catastrophe.[104] Considering the simple ionic model, half an Al ion substituted in the first $SrTiO_3$ layer would avoid the polar discontinuity at the *n*-type interface. La-Sr intermixing could remove the polar discontinuity at the *p*-type interface. During deposition at relatively low oxygen pressure ($\leq 10^{-3}$ mbar), the plasma species were expected to implement in the $SrTiO_3$ due to their high kinetic energy. Using STEM-HAADF and STEM-EELS, atomic interdiffusion has been observed at both *n*- and *p*-type interfaces, La in $SrTiO_3$ as well as Ti in $LaAlO_3$.[13] Furthermore, the interdiffusion appeared to be more pronounced for *n*-type interfaces. Using SXRD, atomic positions and displacements across an *n*-type interface were deduced by fitting the experimental data to simulations.[104, 105] It was concluded that mainly La-Sr intermixing occurs over a longer length scale, resulting in a few monolayers of predominately $LaTiO_3$ stoichiometry and a region of $La_xSr_{1-x}TiO_3$ near the interface. Since $La_xSr_{1-x}TiO_3$ becomes conducting with $0.05 < x < 0.95$, metallic behavior at the $LaAlO_3$-$SrTiO_3$ interface could be observed. This implies that the La doping of the underlying $SrTiO_3$ may be at least partially responsible for electron conduction at the *n*-type interface. Nevertheless, it is not clear why the threshold for conductivity should be four unit cells, unless this thickness of $LaAlO_3$ is required to drive enough La into the $SrTiO_3$ to form a continuous, conductive doped layer. Additionally, interdiffusion does not explain the difference between *n*- and *p*-type interfaces.

Recently, a model based on a polarization discontinuity at the interface has been proposed.[102, 106] In this model, it is suggested that structural reconstructions occur near the interface to avoid the potential build-up. It has been

shown that the unit cell of $SrTiO_3$ is elongated near the $LaAlO_3$-$SrTiO_3$ interface, while the oxygen octahedra are contracted.[12, 107, 108] Moreover, $SrTiO_3$ is polarized near the interface, as measured by optical second harmonic generation (SHG) measurements.[109] The SHG signal increases significantly when the thickness of the $LaAlO_3$ layer reaches four monolayers. It is suggested that the observed polarization in $SrTiO_3$ is related to strain of the oxygen octahedral rotation discontinuity between $SrTiO_3$ and $LaAlO_3$ and would develop with $LaAlO_3$ thickness.[102, 106] At certain growth conditions, the structural reconstructions result in charge transfer to the $SrTiO_3$, where the charge resides in impurity states within the band gap. The energy of the impurity states within the band gap increases with induced polarization. Subsequently, conductivity occurs when the electrons are activated and move into the $SrTiO_3$ conduction band deeper in the $SrTiO_3$. However, this model does not clarify the absence of a $LaAlO_3$ critical thickness when the $LaAlO_3$ surface is capped with $SrTiO_3$.[78, 110] According to the model, oxygen octahedra rotations would be absent in the $SrTiO_3$ substrate for very thin $LaAlO_3$ films.

Despite many studies focused on $LaAlO_3$-$SrTiO_3$ heterostructures, no unified picture can be drawn to clarify the experimental results.

4.1.1 Variations of $LaAlO_3$-$SrTiO_3$

Besides resolving the mechanism behind the interfacial conductivity, improvement of the electronic behavior, e.g. higher mobility, has been widely studied. Improvements have been achieved by, e.g., modifying the standard $LaAlO_3$-$SrTiO_3$ stacking. For example, capping the $LaAlO_3$ surface by $SrTiO_3$ increased the stability and reproducability of the interfacial behavior.[78, 110] Furthermore, the critical thickness of $LaAlO_3$ is absent in these heterostructures. Note that these samples consist of an n-type interface between the $SrTiO_3$ substrate and the $LaAlO_3$ film and a p-type interface between $LaAlO_3$ and the $SrTiO_3$ capping layer. Another $LaAlO_3$ surface capping, $SrCuO_2$-$SrTiO_3$, resulted in an increase of the mobility, up to 5500 $cm^2V^{-1}s^{-1}$, and the absence of thermally activated carriers. In addition, the $LaAlO_3$ critical thickness is increased to six monolayers.[111] The variations between the different heterostructures suggest that the $LaAlO_3$ surface state plays an important role on the electronic behavior.

While $LaAlO_3$ surface states seem to influence the electronic behavior of the interface strongly, it has to be mentioned that the conducting layer is in the $SrTiO_3$ substrate near the interface.[98] Therefore, modifications of the $SrTiO_3$ template are expected to affect the electronic behavior as well. Exploring the influence of the $SrTiO_3$ template will be helpful revealing the mechanism behind the interfacial conductivity. Up to now, the influence of the $SrTiO_3$ template has not been investigated yet.

In this chapter, $LaAlO_3$-$SrTiO_3$ heterostructures with modified $SrTiO_3$ templates are explored to achieve a better understanding of the interface behavior. Two different methods are applied to modify the $SrTiO_3$ layer near the interface. First of all, a $SrTiO_3$ layer has been deposited on $SrTiO_3$ by two different optimized growth methods: PLD and hybrid molecular beam epitaxy (H-MBE). For

Table 4.1: Pseudocubic lattice parameters of commercial available perovskite-type oxides which are used in this chapter. The lattice parameters are at room temperature. Furthermore, their misfit with $SrTiO_3$ and $LaAlO_3$ are given as well as their bulk oxygen octahedra tilt system. Data are taken from [30, 112–115].

Material	lattice constants (nm)	crystal structure	tilt system	misfit $SrTiO_3$	misfit $LaAlO_3$
$SrTiO_3$	0.3905	cubic	$a^0a^0a^0$	-	3.0%
$LaAlO_3$	0.379	rhombohedral	$a^-a^-a^-$	-2.9%	-
LSAT	0.387	cubic	$a^0a^0a^0$	-0.9%	2.1%
$NdGaO_3$	0.386	orthorhombic	$a^+b^-b^-$	-1.2%	1.8%
$DyScO_3$	0.395	orthorhombic	$a^+b^-b^-$	1.2%	4.2%

the differently grown $SrTiO_3$ layers, a slight variation in defect concentration and kind of defects may be expected. According to the suggested models described above, defects are crucial to achieve conductivity. Note that not all defects have to result in mobile charge carriers. The second method is based on inducing biaxial strain on the $SrTiO_3$. Biaxial strain has been achieved by $SrTiO_3$ deposition on other perovskite-type oxide substrates: LSAT, $NdGaO_3$ and $DyScO_3$. As a result, the crystal structure of $LaAlO_3$ varied as well. Inducing biaxial strain is expected to result in an alteration of the oxygen octahedra rotations as well. In Table 4.1, an overview of lattice parameters and octahedra rotations of used substrates are given. The influence of biaxial strain and oxygen octahedral rotations on the film are schematically depicted in Figure 4.1. Figure 4.1a and b illustrate the change in in-plane lattice parameters, accommodated entirely by a change in the in-plane metal-oxygen bond lengths. Figure 4.1c and d show that the lattice mismatch can be accommodated by a change in magnitude or type of tilt patterns through rigid rotations of the oxygen octahedra. In this case, the B-O bond lengths remain unchanged, but the B-O-B bond angle varies.

4.2 Sample Fabrication

4.2.1 Substrates

Before growth, $DyScO_3$ (110), $SrTiO_3$ (001) and $NdGaO_3$ (110) substrates were chemically and thermally treated to achieve B-site termination. $DyScO_3$ was chemically treated with NaOH (aq) solution after annealing, as described in chapter 2. $SrTiO_3$ was chemically treated with H_2O and buffered HF before annealing.[21] $NdGaO_3$ was chemically treated with H_2O and a modified HF solution before annealing.[117] LSAT (001) was treated thermally, resulting in mainly B-site termination.[118, 119]

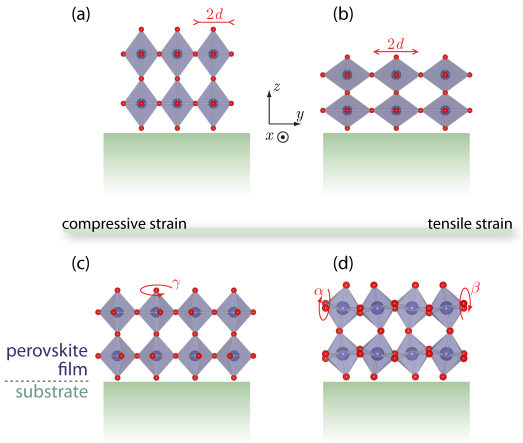

Figure 4.1: Coherently strained perovskite films. The BO_6 octahedra deformation under compressive and tensile strain are shown in (a) and (b) respectively, where d is the equatorial B-O bond length. (c) and (d) show the octahedral rotations perpendicular and parallel to the substrate, respectively. The Figure is reproduced with permission from ref. [116].

4.2.2 Growth

$SrTiO_3$ (001) films were grown by PLD and H-MBE. Five to twenty monolayers thick $SrTiO_3$ films were grown by PLD on $SrTiO_3$, LSAT, $DyScO_3$ and $NdGaO_3$. $SrTiO_3$ was ablated from a single crystal target using a fluence of 1.3 Jcm^{-2} and a laser frequency of 1 Hz. The films were grown at $1{\times}10^{-1}$ mbar oxygen and a substrate temperature of ∼750 °C. Subsequently, the growth was either continued with $LaAlO_3$ deposition or the sample was cooled down in 100 mbar oxygen by turning off the heater (taking 1.5-2 hours). The PLD chamber was pumped down when the heater temperature was below 90 °C. For H-MBE, 20 monolayers of $SrTiO_3$ were grown on $SrTiO_3$ and LSAT substrates.[1] Jalan *et al.* have achieved high quality $SrTiO_3$ films by using H-MBE.[120, 121] Instead of using an effusion cell for Ti as well as for Sr (like MBE), a Ti-organic complex was used as Ti source: titanium tetraisopropoxide [$Ti(OC_3H_7)_4$ or TTIP]. This enlarged the growth window of stoichiometric $SrTiO_3$ in comparison to conventional MBE. More experimental details can be found in refs. [120–122].

Here, $LaAlO_3$ was always grown by PLD. It was ablated from a single crystal target using a fluence of 1.3 Jcm^{-2} and a laser frequency of 1 Hz. The oxygen background pressure was varied from $1{\times}10^{-6}$ to $1{\times}10^{-1}$ mbar. The substrate temperature was kept at ∼750 °C. Samples with a thick $LaAlO_3$ layer (≥10 monolayers) were capped by 2 monolayers of $SrTiO_3$, as capping enhances the stability and reproducability of the electronic properties.[78, 110] The $SrTiO_3$ capping layer

[1]The H-MBE $SrTiO_3$ films were grown by B. Jalan, University of California, Santa Barbara.

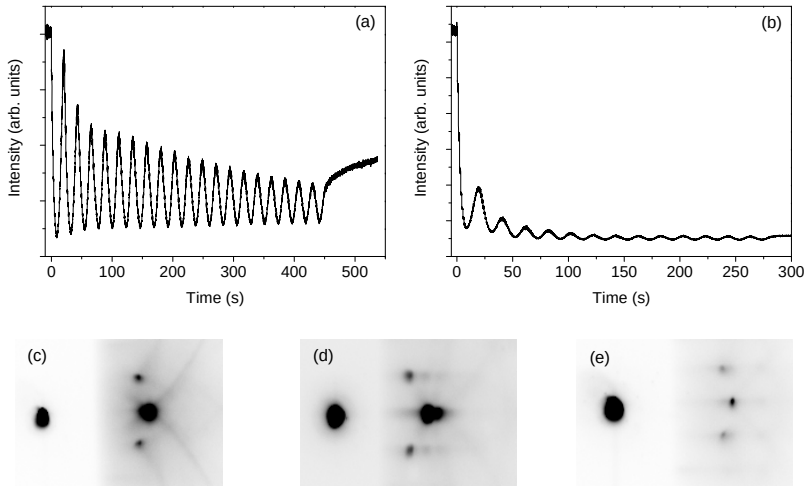

Figure 4.2: RHEED oscillations of (a) $SrTiO_3$ and (b) $LaAlO_3$ grown on $SrTiO_3$. $SrTiO_3$ was grown at 10^{-1} mbar and cooled down afterwards. Subsequently, the $LaAlO_3$ layer was grown at 10^{-3} mbar. The RHEED patterns of a $SrTiO_3$ substrate (a), after $SrTiO_3$ growth (b) and after $LaAlO_3$ growth (c).

was grown under the same conditions as the underlying $LaAlO_3$ layer.

Growth was *in situ* studied by RHEED. Clear RHEED oscillations were observed for both $SrTiO_3$ and $LaAlO_3$ as shown in Figure 4.2. The amplitude of the $SrTiO_3$ RHEED oscillations decreased over time, but the RHEED pattern remained two dimensional. This is in agreement with previous studies on homoepitaxial $SrTiO_3$ growth at 10^{-1} mbar and implies an increased surface roughening at the atomic scale.[123] The intensity decrease of the specular spot during the initial $LaAlO_3$ growth is typical for $LaAlO_3$ on $SrTiO_3$. This is probably due to the differences in structure factor. After the first few monolayers, the amplitude of the oscillations remained constant, which suggests a constant surface roughness.

4.2.3 Surface morphology

The low surface roughness was confirmed by AFM, as shown in Figure 4.3. Representative AFM height images of $LaAlO_3$-$SrTiO_3$ on $NdGaO_3$ and LSAT can be found in ref. [124] and ref. [118], respectively. The substrate terrace morphology was clearly visible. This points to layer-by-layer growth with preserved B-site termination, which is in agreement with the RHEED data.

4.3 Results $SrTiO_3$-$SrTiO_3$

To study the effect of the $SrTiO_3$ template on the interfacial behavior, $SrTiO_3$ substrates were replaced by $SrTiO_3$ thin films. In this section, the properties of

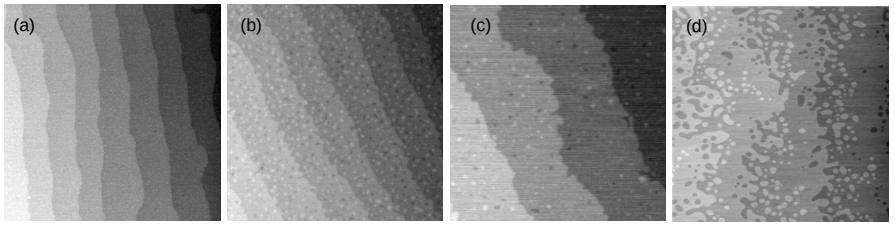

Figure 4.3: AFM height images of (a) $SrTiO_3$(PLD)-$SrTiO_3$, (b) $SrTiO_3$(H-MBE)-$SrTiO_3$, (c) $LaAlO_3$-$SrTiO_3$(PLD)-$SrTiO_3$ and (d) $LaAlO_3$-$SrTiO_3$(PLD)-$DyScO_3$. The images are respectively 2×2, 1.5×1.5, 1×1 and 5×5 μm^2. The height difference between the terrace steps correspond to a single unit cell (∼0.4nm).

the $SrTiO_3$ films are studied in more detail. Besides the surface morphology of $SrTiO_3$, which influences the interface roughness, the $SrTiO_3$ stoichiometry has to be considered. Off-stoichiometry changes the cubic crystal structure of $SrTiO_3$ at room temperature, but may also change the physical properties. In this chapter, $SrTiO_3$-$SrTiO_3$ structures were studied by XRD, XRR and XPS. Furthermore, the electronic properties of the $SrTiO_3$ films were determined. In combination with RHEED and AFM, a good estimation of the film quality could be given. Nevertheless, these techniques do not give information on the physical behavior of the $SrTiO_3$ film.

In a previous study, the thermal conductivity of $SrTiO_3$ films is determined by Oh *et al.*.[125] Thermal conductivity is sensitive for defects and, therefore, a useful technique to define the film quality. In Figure 4.4a and b, the thermal conductivity (Λ) versus temperature has been shown for several $SrTiO_3$ templates grown by PLD and MBE. It has to be mentioned that the MBE-1 samples were grown under identical circumstances as the H-MBE samples discussed in this chapter. The PLD-2 samples are comparable with the PLD grown samples in this chapter.

The thermal conductivity of MBE-1, PLD-2 are similar to the thermal conductivity of the single crystal at room temperature (solid line). Small deviations are observed at lower temperatures. Figure 4.4b shows clear differences in thermal conductivity between several PLD grown films. This variance is caused by the used target during growth. The use of a single crystal target resulted in films with a significant higher thermal conductivity than the use of a ceramic target. Oh *et al.* mentioned that for the homoepitaxial layers, the decrease in thermal conductivity correlated well with the expansion of the lattice parameter in the direction normal to the surface.[125] They reported that the out-of-plane lattice parameter of MBE-1 and PLD-2 were similar to bulk $SrTiO_3$.[125] This implies a low defect concentration in these $SrTiO_3$ templates.

4.3.1 Electronic properties

$SrTiO_3$ is a wide band gap insulator, but $SrTiO_3$ can become conducting by introducing oxygen vacancies or cation doping.[126] The electronic transport proper-

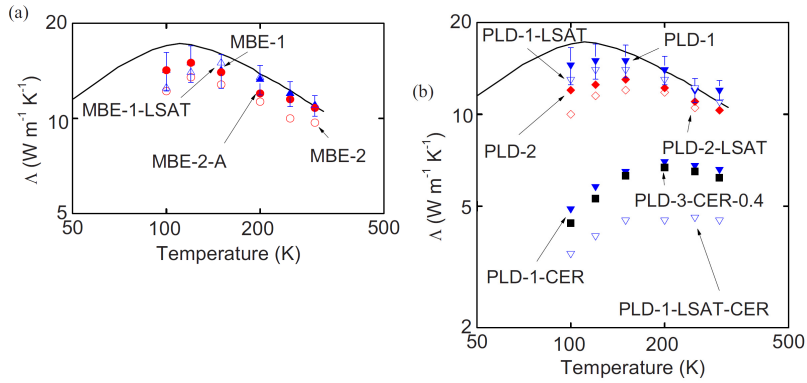

Figure 4.4: Thermal conductivity versus temperature of several $SrTiO_3$ templates and compared with a $SrTiO_3$ single crystal (solid line). (a) Molecular beam epitaxy (MBE) samples, grown at the University of California Santa Barbara (MBE-1) and at Cornell University (MBE-2). MBE-2-A was deposited under under identical conditions as MBE-2, but was subsequently post annealed. (b) PLD samples, grown at University of California Berkeley, (PLD-1), University of Twente (PLD-2) and University of Illinois (PLD-3). CER indicates samples using ceramic $SrTiO_3$ targets instead of single crystal targets during PLD. If not else mentioned, the $SrTiO_3$ layer was grown on $SrTiO_3$. The Figure was reproduced with permission from ref. [125].

ties of $SrTiO_3$-$SrTiO_3$ homostructures grown by PLD and H-MBE were measured using a 4-probe Van der Pauw method with ultrasonically wire-bonded aluminum wires as electrodes. The measurements were performed in a Quantum Design PPMS. No resistivity could be determined at room temperature, indicating insulating $SrTiO_3$. This is in agreement with the electronic behavior of bulk stoichiometric $SrTiO_3$.

4.3.2 X-ray diffraction and X-ray reflectivity

XRD and XRR measurements give information on the crystal structure, density, film thickness and roughness of the surface and interfaces. For perfect $SrTiO_3$ films on $SrTiO_3$, only strong substrate peaks can be observed by XRD. However, small variation in, e.g., density results in the appearance of a film peak and/or thickness interference fringes.

Figure 4.5a shows reciprocal space maps of twenty monolayers thick $SrTiO_3$ films on $SrTiO_3$ (001) grown by PLD and H-MBE, measured with a Bruker D8 Discover. By measuring 2θ versus ω around the substrate peak, the θ-2θ scan is not obscured by diffuse scattering. As a result, small discrepancy between substrate and film can be observed. For the H-MBE sample, thickness fringes are weakly present, marked by the arrow in Figure 4.5a, but no film peak could be distinguished. The thickness fringes are in line with in-plane lattice parameters of $SrTiO_3$, which implied coherently grown $SrTiO_3$ with identical in-plane lattice

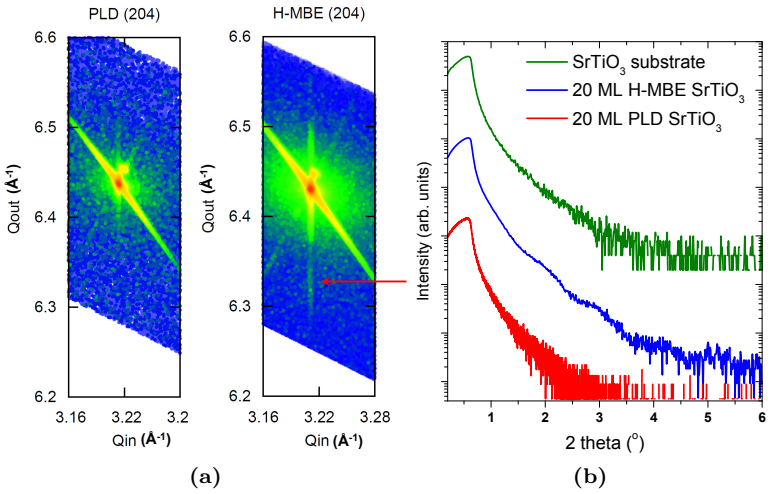

Figure 4.5: (a) (204) reciprocal space maps of 20 monolayers of $SrTiO_3$ on $SrTiO_2$ grown by PLD (left) and H-MBE (right). The arrow points to a thickness fringe of the H-MBE grown $SrTiO_3$ layer. (b) X-ray reflectivity scans of a $SrTiO_3$ substrate and 20 monolayers of H-MBE and PLD grown $SrTiO_3$ on $SrTiO_3$.

parameters to the substrate. The presence of fringes and the absence of a film peak indicate slight off-stoichiometry in the film. For PLD grown $SrTiO_3$, no film peak and no thickness fringes were observed. This indicates that the stoichiometry of the PLD grown $SrTiO_3$ is similar to the substrate.

The differences in unit cell density of $SrTiO_3$ on $SrTiO_3$ were confirmed by XRR, as shown in Figure 4.5b. No interference fringes were observed for PLD grown films. This points to similar unit cell density for both $SrTiO_3$ layers and an atomically sharp interface. On the other hand, clear fringes were observed for H-MBE grown $SrTiO_3$ on $SrTiO_3$. The separation of the minima corresponds to an 8 nm thick layer, which is similar to the 20 unit cell thick $SrTiO_3$ film. By fitting the H-MBE data, using Diffrac^{plus} LEPTOS software, the density difference between film and substrate was estimated to be approximately 3%.

It is important to mention that $SrTiO_3$ films grown on $NdGaO_3$, LSAT and $DyScO_3$ were coherently strained with identical in-plane lattice parameters to the substrates. The out-of-plane lattice parameters were approximately 0.395 nm on $NdGaO_3$, 0.393 nm on LSAT and 0.383 nm on $DyScO_3$.

4.3.3 X-ray photoelectron spectroscopy

XPS is a quantitative spectroscopic technique which can be used to determine the empirical formula. Here, a rough estimation of the cation ratio of the top $SrTiO_3$ layers was achieved by comparing XPS spectra of grown $SrTiO_3$ films with $SrTiO_3$ substrates. A detailed setup description is given in section 3.2.4. Bulk survey

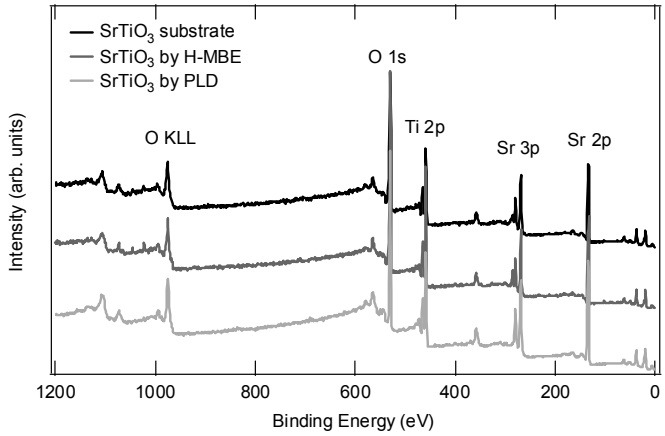

Figure 4.6: XPS survey scans of a $SrTiO_3$ substrate, and 20 monolayers thick $SrTiO_3$ films grown by PLD and H-MBE. The measurements were done at an emission angle of 80°.

scans are shown in Figure 4.6. The main features include the O KLL edge around 975 eV, the O 1s at 530.1 eV, Ti 2p around 460 eV, Sr 3p around 270 eV and Sr 3d around 135 eV. Carbon contamination at the surface was observed on *ex situ* measured H-MBE grown $SrTiO_3$ and $SrTiO_3$ substrates at approximately 286 eV. No indication for other impurity atoms was found. Detailed scans around the Ti 2p and Sr 3p show similar FWHM for the various samples. The FWHM of Ti $2p_{3/2}$ is 1.0±0.1 eV and the FWHM of Sr $3p_{3/2}$ is 2.0±0.1 eV. The Sr/Ti area ratios were determined from the survey scans and are given in Table 4.2.

The Sr/Ti ratios of PLD grown $SrTiO_3$ and $SrTiO_3$ substrate are comparable, indicating similar Sr-Ti stoichiometry. For the more surface sensitive measurements (30°), the Sr/Ti ratio increased significantly for the PLD grown film. This

Table 4.2: Integrated XPS Sr/Ti ratios of different $SrTiO_3$ samples for several emission angles. The total area was set to [Sr]+[Ti]=100%. The error margins were estimated on the quality of the background substraction routines. The 20 monolayers thick $SrTiO_3$ films were grown on $SrTiO_3$ (001).

Sample	angle(°)	Sr $3p_{3/2}$ (%)	Ti $2p_{3/2}$ (%)	Sr/Ti
$SrTiO_3$ substrate 1	80	50.4±1	49.6±1	1.02±0.05
$SrTiO_3$ substrate 2	80	48.5±1	51.5±1	0.94±0.05
$SrTiO_3$ substrate 2	30	49.9±1	50.1±1	1.0±0.05
$SrTiO_3$ by PLD 1	80	48.6±1	51.4±1	0.95±0.05
$SrTiO_3$ by PLD 1	30	54.4±1	45.6±1	1.19±0.05
$SrTiO_3$ by PLD 2	80	49.8±1	50.2±1	0.99±0.05
$SrTiO_3$ by H-MBE 1	80	47.2±1	52.8±1	0.89±0.05

could point to an increase of Ti vacancies in the top surface layer. Other possibilities are a gradual shift from TiO_2 to SrO termination during growth or Sr outward diffusion. It has to be mentioned that Sr outward diffusion towards the top unit cells occurs at high temperature, independent of oxygen pressure.[127] Additionaly, it is shown that high pressure growth of $SrTiO_3$ does not tend to result in Sr rich $SrTiO_3$ films.[128] Note that off-stoichiometry is hard to determine by XRD and XRR measurements if only the top-most unit cell is off-stoichiometric. The H-MBE grown $SrTiO_3$ film showed a relatively low Sr/Ti ratio. The decreased Sr/Ti ratio could be due to an increase of Sr vacancies, which may clarify the fringes in the XRD and XRR data.

4.4 Results $LaAlO_3$-$SrTiO_3$

4.4.1 Electronic properties

The electronic behavior of the $LaAlO_3$-$SrTiO_3$ heterostructures was measured using a 4-probe Van der Pauw method with ultrasonically wire-bonded aluminum wires as electrodes. The electrical transport and Hall-effect measurements were performed in a Quantum Design PPMS in the temperature range from 300 K down to 2 K with magnetic fields up to 9 T.

$LaAlO_3$-$SrTiO_3$ under induced strain

The electronic behavior of several $LaAlO_3$-$SrTiO_3$ heterostructures under induced strain was studied. The thickness of the $SrTiO_3$ was varied from 5 to 20 monolayers; the thickness of the $LaAlO_3$ layer was varied from 2 to 15 monolayers. Furthermore, the oxygen growth pressure during $LaAlO_3$ growth was varied from 10^{-6} to 10^{-1} mbar.

$LaAlO_3$-$SrTiO_3$ on $NdGaO_3$ and $DyScO_3$ appeared to be insulating, independent of the $LaAlO_3$ film thicknesses. Heterostructures on LSAT became conducting, independent of the $SrTiO_3$ growth technique. However, the $LaAlO_3$ growth pressure had to be reduced to 10^{-6}–10^{-5} mbar to achieve conducting interfaces. The conducting heterostructures showed a slight upturn in sheet resistance at low temperatures. Moreover, the electron mobility was significantly lower than the mobility of standard $LaAlO_3$-$SrTiO_3$, while the carrier density increased by one order of magnitude.[118] The conducting behavior of $LaAlO_3$-$SrTiO_3$-LSAT could be destroyed by the introduction of a single SrO layer, i.e. creating a p-type interface.

$LaAlO_3$-$SrTiO_3$ on $SrTiO_3$

Previous studies have shown that the interface of $LaAlO_3$ on $SrTiO_3$ substrates is metallic as long as the $LaAlO_3$ layer is grown $\leq 10^{-3}$ mbar.[66] In this section, twenty monolayers of $SrTiO_3$ are introduced between the $SrTiO_3$ substrate and the $LaAlO_3$ film. Here, the $LaAlO_3$ was grown at 10^{-3} mbar. The heterostructures with PLD grown $SrTiO_3$ appeared to be insulating, which is in agreement with the

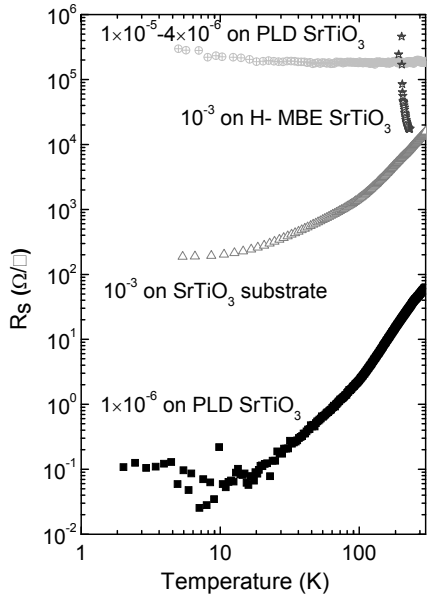

Figure 4.7: The sheet resistance versus temperature of several $LaAlO_3$-$SrTiO_3$-$SrTiO_3$ heterostructures, where $LaAlO_3$ was grown at several oxygen pressures.

observations of Fix *et al.*. They observed a decrease in conductivity for increased $SrTiO_3$ film thickness.[99] For H-MBE grown $SrTiO_3$, the sheet resistance could be determined at room temperature, which is shown in Figure 4.7. During cool-down, the sheet resistance increased significantly; below 200 K, the resistance was above the detection limit. This behavior indicates that the $LaAlO_3$-$SrTiO_3$(H-MBE) interface is insulating.

For $LaAlO_3$-$SrTiO_3$ on LSAT, the growth pressure of $LaAlO_3$ had to be reduced to achieve conducting interface.[118] To distinguish a similar trend for $LaAlO_3$-$SrTiO_3$(PLD)-$SrTiO_3$, the growth pressure of the $LaAlO_3$ layer was reduced systematically. When $LaAlO_3$ was grown at $\leq 1\times10^{-5}$ mbar, the sheet resistance could be determined. However, no electron mobility and carrier density could be determined due to low excitation current. Reducing the $LaAlO_3$ growth pressure further, the conducting behavior of the heterostructure was dominated by the conductivity of bulk $SrTiO_3$. This does not preclude that the $LaAlO_3$-$SrTiO_3$ is conducting as well.

4.4.2 X-ray photoelectron spectroscopy

XPS was used to achieve information on the interface chemistry and the possible origin of the interface conductivity. As discussed in section 4.1, one of the possible mechanisms to overcome the polar discontinuity between $LaAlO_3$ and $SrTiO_3$, is electron doping from the $LaAlO_3$ surface to the TiO_2 layer at the interface. This

results in the formation of Ti^{3+}, which could be observed by XPS in the core level spectra. Moreover, band bending of the $LaAlO_3$, due to the potential build-up, should be visible with XPS, since it would result in broadening of the La and Al peaks. Finally, the influence of the La/Al ratio in $LaAlO_3$ is under high debate. Here, XPS is used to give information on the chemical composition of $LaAlO_3$. The same setup as described in section 3.2.4 was used.

Potential build-up

The potential build-up in $LaAlO_3$ is expected to be gradual over thickness. For n-type interfaces, this results in a gradual shift of the core levels and valence band spectra towards lower binding energy. As a result, the La as well as the Al peaks should be broadened to lower binding energy and become asymmetric; the exact shape would depend on the $LaAlO_3$ thickness. The potential build-up across the $LaAlO_3$ was expected to grow with increased thickness, until electron crossover from the $LaAlO_3$ valence band to the $SrTiO_3$ conduction band occurs. The predicted asymmetric broadening versus thickness is schematically depicted by Segal *et al.*.[11]

In this section, *in situ* measured La and Al spectra of $LaAlO_3$ are presented. La $3d_{5/2}$ spectra of $LaAlO_3$ on several templates are shown in Figure 4.8a and compared with the spectrum of a $LaAlO_3$ single crystal. The La $3d_{5/2}$ spectra were symmetric and no significant broadening was observed, which is comparable to the results of Segal *et al.*.[11] It is interesting to note that no difference has been observed between conducting and insulating heterostructures. This implies that the potential build-up is absent, which suggests that the electronic reconstruction model is not applicable to clarify the conductivity at the n-type interface.

The Al $2p$ spectra were broadened and asymmetric, as shown in Figure 4.8b. The asymmetric broadening was to higher binding energy and independent of the $LaAlO_3$ film thickness. This is in conflict with the electronic reconstruction model. The broadening was canceled by introducing a capping layer, like polar $LaTiO_3$. Therefore, it is suggested that the observed broadening is due to chemical distortion of the top-most AlO_2 layer, which is the terminating atomic plane in standard $LaAlO_3$-$SrTiO_3$ heterostructures.

Presence of Ti^{3+}

The electronic reconstruction model includes electron transfer from the $LaAlO_3$ surface to the n-type interface, ideally half an electron charge per two dimensional interface unit cell. These electrons are suggested to locate at the Ti $3d$ band near the interface, resulting in Ti^{3+}. The presence of Ti^{3+} at the $LaAlO_3$-$SrTiO_3$ interface can be distinguished by XPS as shown by Sing *et al.*.[84] They observed a lower Ti^{3+} signal than predicted by the electronic reconstruction model. Moreover, a strong influence of the $LaAlO_3$ growth pressure and background gas on the Ti^{3+} signal was observed.[129] Müller *et al.* showed that the Ti^{3+} signal became neglegible for insulating heterostructures grown at high oxygen pressures (10^{-1} mbar). It is worth mentioning that the formation of oxygen vacancies and

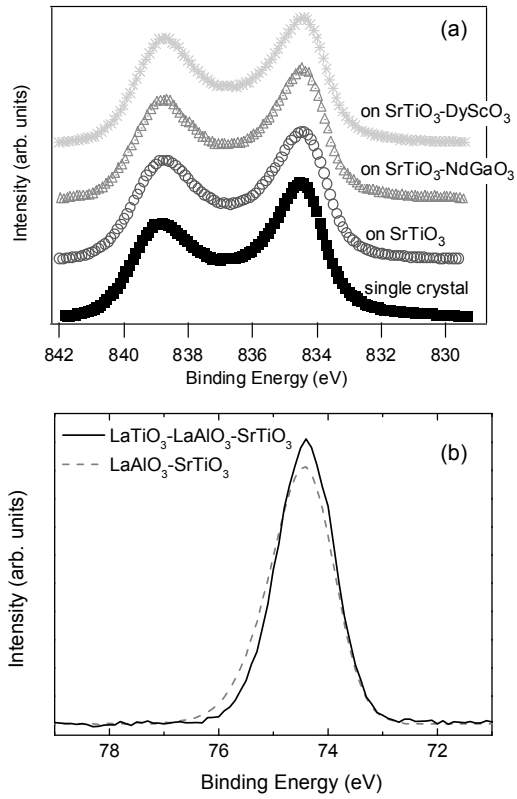

Figure 4.8: (a) XPS La $3d_{5/2}$ spectra of several $LaAlO_3$ films. All $LaAlO_3$ films were five monolayers thick, the $SrTiO_3$ was grown by PLD. (b) XPS Al $2p$ spectra of uncapped $LaAlO_3$ and $LaAlO_3$ capped by thin $LaTiO_3$. The $LaAlO_3$ layer was 30 monolayers thick. The La spectra were taken at 80° with respect to the analyzer normal, the Al spectra at 39°.

intermixing may result in Ti^{3+} as well.

Here, the Ti^{3+} signal has been determined for several modified $LaAlO_3$-$SrTiO_3$ heterostructures. For these heterostructures, twenty monolayers of $SrTiO_3$ were deposited at 10^{-1} mbar oxygen and cooled down at 100 mbar oxygen after growth. The $LaAlO_3$ layer was 5 unit cells thick and grown at 10^{-5} mbar on $SrTiO_3$-$NdGaO_3$ and at 10^{-3} mbar on the other $SrTiO_3$ templates. Their Ti $2p_{3/2}$ spectra are shown in Figure 4.9.

In both $SrTiO_3$ single crystal and bare $SrTiO_3$ films, no Ti^{3+} signal was observed, while a small, but distinct Ti^{3+} signal was present in the $LaAlO_3$-$SrTiO_3$ heterostructures. The Ti^{3+} signal appeared to depend on the $SrTiO_3$ template. The Ti^{3+} signal was most pronounced in the standard $LaAlO_3$-$SrTiO_3$ heterostructure. For the heterostructure on $NdGaO_3$, a comparable Ti^{3+} signal was observed, but this is expected to be due to the reduced $LaAlO_3$ growth pressure.

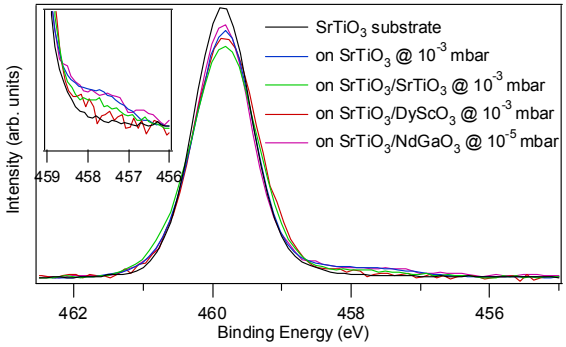

Figure 4.9: Ti $2p_{3/2}$ XPS spectra of 5 monolayers $LaAlO_3$ on $SrTiO_3$. The grown $SrTiO_3$ was 20 unit cells thick and grown by PLD. As a reference, the spectrum of a TiO_2 terminated $SrTiO_3$ substrate is shown. The inset shows a zoom-in around the Ti^{3+} peak. The spectra were taken at 80° with respect to the analyzer normal. The peaks were normalized on their total area.

The decreased Ti^{3+} signal for modified $LaAlO_3$-$SrTiO_3$ heterostructures can be explained by a reduction of oxygen vacancies or less La interdiffusion. The broadening of the Ti peak of $LaAlO_3$-$SrTiO_3$-$DyScO_3$ is probably due to charging, as the sample was highly insulating.

$LaAlO_3$ stoichiometry

Currently, the $LaAlO_3$ cation stoichiometry and its influence on the electronic behavior is under high debate. PLD grown films can be off-stoichiometric, as shown by XPS and Rutherford back scattering (RBS) measurements.[130] Most samples were La deficient. However, Al deficiency has also been reported.[130] Schlom *et al.* suggested that there is a relation between the La/Al ratio and the interfacial conductivity.[131] They observed conducting interfaces when the La/Al ratio was $\leq 0.97 \pm 0.03$.[2] It has been proposed that more oxygen diffuses outward the $SrTiO_3$ when being in contact with a La deficient $LaAlO_3$ film compared to being in contact with an Al deficient film.[132, 133] As a result, La deficient $LaAlO_3$-$SrTiO_3$ heterostructures become metallic, while Al deficient $LaAlO_3$-$SrTiO_3$ heterostructures would remain insulating.

Up to now, La-Al stoichiometry has been determined for samples grown at low oxygen pressures, $\leq 10^{-2}$ mbar. In this pressure regime, the interfaces can become conducting. Here, also high pressure grown $LaAlO_3$ films (at 10^{-1} mbar) were taken into account. The plasma kinetics are completely different at 10^{-1} mbar. The plasma species are oxidized and have a low kinetic energy, as discussed in chapter 3. Furthermore, the plasma plume is confined, while it expands freely at low background pressures.

[2] It has to be mentioned that the study of Schlom *et al.* was mainly focused on MBE grown $LaAlO_3$ films on $SrTiO_3$.[131]

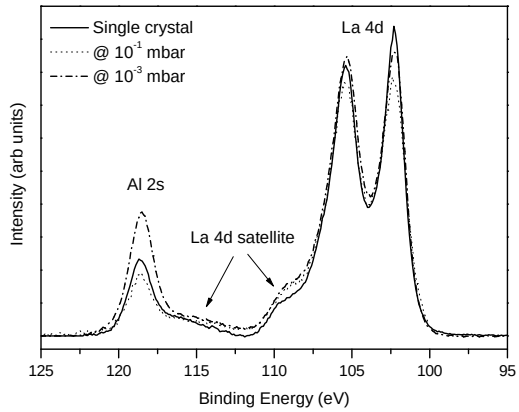

Figure 4.10: La 4*d* and Al 2*s* XPS spectra of a $LaAlO_3$ single crystal and of 5 monolayers thick $LaAlO_3$ films grown at 10^{-1} and 10^{-3} mbar O_2. The spectra were acquired *in situ* after growth at 80° with respect to the analyzer normal. The data were normalized on the total [La]+[Al] area.

In Figure 4.10, La 4*d* and Al 2*s* XPS spectra of heterostructures grown at various oxygen pressures are shown.[3] $LaAlO_3$ grown at low oxygen pressure showed La deficiency, which is consistent with literature.[130] The deficiency was independent of the O_2 growth pressure $\leq 10^{-3}$ mbar. A clear increase of the La/Al ratio was observed for $LaAlO_3$ grown at high oxygen pressures. This trend was independent of the $SrTiO_3$ template. The La/Al ratio became similar to the La/Al ratio of the single crystal. Note that the La sattelite feature is slightly different for grown $LaAlO_3$ layer. This might be induced by structural changes in the $LaAlO_3$ film.

4.4.3 Scanning transmission electron microscopy

STEM was used to achieve information on the crystal structure and stoichiometry. Figure 4.11 shows the results of 5 monolayers $LaAlO_3$ on PLD grown $SrTiO_3$-$SrTiO_3$, where $LaAlO_3$ was grown at 10^{-3} mbar. The STEM-HAADF image shows 5 monolayers of La and 20 monolayers of grown Sr, which is in agreement with the RHEED analysis. Moreover, the image shows that the films were fully epitaxial grown on $SrTiO_3$. In the HAADF-STEM image, lattice fringes were observed for $SrTiO_3$ as well as $LaAlO_3$. The La and Sr columns are clearly visible, which is due to their relatively high atomic weight in contrast to the Al and Ti columns. The interface between $LaAlO_3$ and $SrTiO_3$ could easily be distinguished due to the high contrast between Sr and La. A slight contrast between substrate and $SrTiO_3$ film was also visible, which may originate from differences in, e.g. strain, impurities and off-stoichiometry.

[3]Note that the Al 2*s* is obscured by satellites of the La 4*d*.

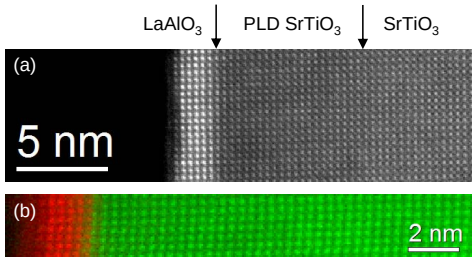

Figure 4.11: (a) HAADF-STEM image of a 5 ML $LaAlO_3$ grown on $SrTiO_3$(PLD)-$SrTiO_3$(001) at 10^{-3} mbar O_2 and its corresponding STEM-EELS image after PCA treatment (b). La is shown in red and Ti in green. The arrows point to the $LaAlO_3$-$SrTiO_3$ and $SrTiO_3$-$SrTiO_3$ interfaces. The measurements were performed at the EMAT centre in Antwerp, Belgium.

From STEM-EELS spectra, it appeared that the oxygen signal was slightly higher in PLD grown $SrTiO_3$ in comparison to the $SrTiO_3$ substrate. EELS quantification indicated an increase of the Ti/O ratio of approximately 3.8% in PLD grown $SrTiO_3$. The increased Ti/O ratio may originate from O enrichment or Ti deficiency. However, from angle resolved XPS, Ti deficiency was suggested to be only present in the top-most atomic plane. The deviation in the Ti/O ratio may clarify the contrast at the $SrTiO_3$-$SrTiO_3$ interface. The fine structures of Ti and O were similar along PLD $SrTiO_3$ and bulk $SrTiO_3$. This suggests that the Ti ions have on average a similar oxidation state and coordination in both $SrTiO_3$ layers.

The STEM-HAADF image does not show any Ruddlesden-Popper phase, which has been observed for Sr-rich $SrTiO_3$ by Brooks *et al.*.[134] For Sr-poor $SrTiO_3$, they observed a disordered structure. Here, no clear structural disordering has been observed in PLD grown $SrTiO_3$, indicating a Sr concentration close to 1.

STEM-EELS elemental scan profiles of La, Ti and O show intermixing between the $SrTiO_3$ and $LaAlO_3$ layers. La and Ti diffusion nicely dropped to zero at approximately 3 unit cells deep inside the $SrTiO_3$ and $LaAlO_3$, respectively. This points to a broad interface between $LaAlO_3$ and $SrTiO_3$, which is comparable with standard $LaAlO_3$-$SrTiO_3$ interfaces.[13, 79, 135]

4.4.4 High temperature conductance characteristics

High temperature oxygen equilibrium conductance (HTEC) behavior of $LaAlO_3$-$SrTiO_3$ interfaces on $SrTiO_3$ was investigated as function of ambient oxygen partial pressure and temperature. At the measurement temperatures (850-1100 K), the samples are in equilibrium with the surrounding oxygen atmosphere. As a result, the effect of mobile oxygen vacancies on the interface conductivity can be ruled out.[135–137] Therefore, HTEC measurements give more insight on the defect chemistry of the heterostructures, other than oxygen vacancies. To examine the influence of grown $SrTiO_3$, the H-MBE and PLD grown heterostructures are

compared with a $SrTiO_3$ substrate and a standard $LaAlO_3$-$SrTiO_3$ heterostructure.

The HTEC measurements were carried out in an yttria-stabilized zirconia oxygen-pump system, where the oxygen partial pressure could continuously be adjusted between 1 and 10^{-22} bar. The temperature was varied from 850 K to 1100 K. The H-MBE as well as the PLD grown $SrTiO_3$ films were 20 monolayers thick. The $LaAlO_3$ layer was kept at 10 monolayers and capped with two monolayers of $SrTiO_3$. $LaAlO_3$ was grown at 10^{-3} mbar and the samples were subsequently cooled down at growth pressure. Further experimental details of the HTEC measurements are given in [135].

Comparing the electronic properties of the heterostructures at low temperatures (see Fig. 4.7), clear differences were present. Heating the heterostructures to 850-1100 K, all samples became conducting, since $SrTiO_3$ becomes conducting in oxygen deficient atmospheres at elevated temperatures.[138] Figure 4.12a shows the HTEC characteristic of a single crystalline $SrTiO_3$ substrate. As a result of oxygen exchange, the typical V-shaped curve is present with enhanced n-type and p-type conductance in reduced and oxidized atmospheres, respectively.[139] The n-type conductivity is a result of oxygen loss, which gives rise to the generation of free electrons. In oxygen rich atmospheres, p-type conductivity is observed due to the creation of free holes when incorporating oxygen into the crystal. The underlying oxygen exchange reactions are given by the Kröger-Vink notation:

$$\text{Reduction: } O_O^{\times} \leftrightarrow 2e' + V_O^{\bullet\bullet} + \tfrac{1}{2}O_2$$

$$\text{Oxidation: } V_O^{\bullet\bullet} + \tfrac{1}{2}O_2 \leftrightarrow 2h^{\bullet} + O_O^{\times}$$

where mobile oxygen vacancies are given by $V_O^{\bullet\bullet}$ and $^{\times}$ denotes zero charge, $'$ single negative charge and $^{\bullet}$ single positive charge. From the Kröger–Vink notation, the characteristic slopes observed in the P_{O_2}-dependence of the conductivity ($-\frac{1}{4}$ and $+\frac{1}{4}$) can be deduced for $SrTiO_3$ with inherent acceptor-type impurity content. The plateau at low temperatures and intermediate pressures is attributed to the ionic conductivity contribution resulting from oxygen vacancy diffusion.[135]

Comparing the $SrTiO_3$ substrate with the standard $LaAlO_3$-$SrTiO_3$ heterostructure (see Fig. 4.12b), the conductance deviates significantly at intermediate P_{O_2}, revealing an additional conduction path generated by the metallic $LaAlO_3$-$SrTiO_3$ interface. Note that at higher temperatures (1100 K) as well as in highly reduced and oxidized regimes, the conductance of $LaAlO_3$-$SrTiO_3$ is dominated by the contribution of the $SrTiO_3$ substrate.

Figure 4.12c and d, show the HTEC characteristics of $LaAlO_3$-$SrTiO_3$ heterostructures with H-MBE and PLD grown $SrTiO_3$ respectively. It is remarkable that the H-MBE heterostructure shows a similar behavior as the standard $LaAlO_3$-$SrTiO_3$ heterostructure, while the PLD heterostructure has an analogous behavior to the $SrTiO_3$ single crystal. Also for these heterostructures, the conductivity is dominated by the bulk $SrTiO_3$ conductivity at high and low oxygen partial pressures. The HTEC measurements of all samples are similar at these conditions.

At intermediate pressures, standard $LaAlO_3$-$SrTiO_3$ and the H-MBE heterostructure show a plateau. The conductance decreased only slightly from low P_{O_2}

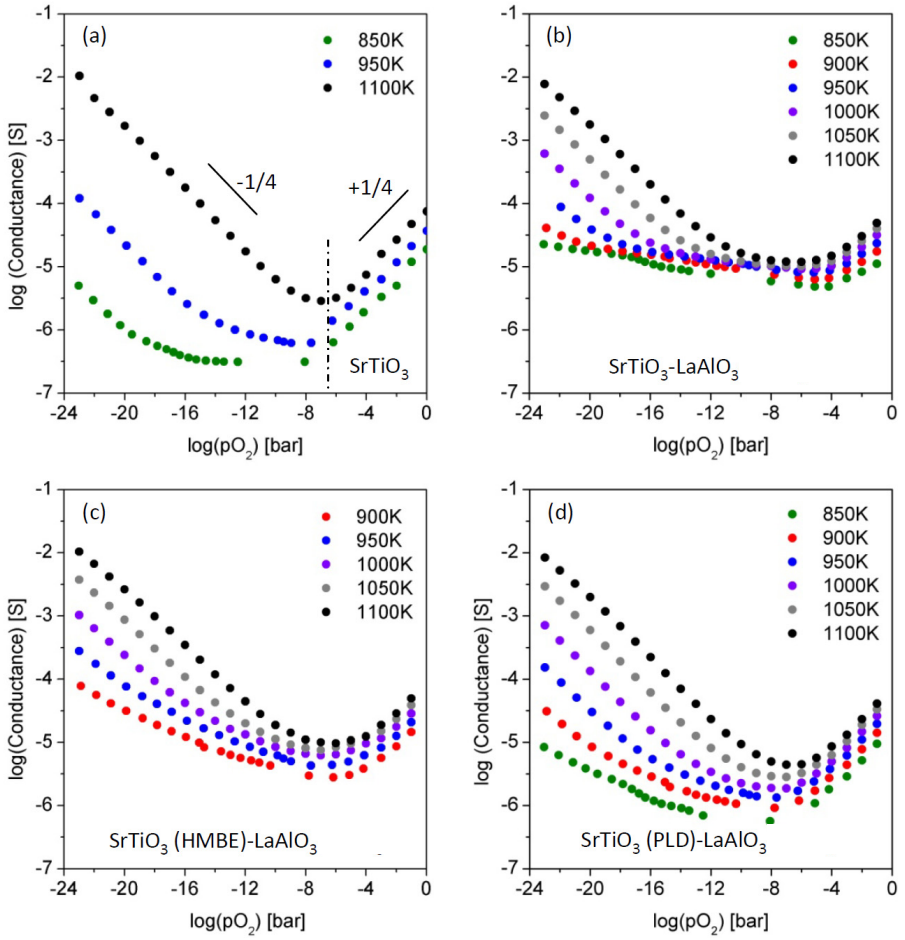

Figure 4.12: HTEC characteristics of (a) $SrTiO_3$ single crystal, (b) standard $LaAlO_3$-$SrTiO_3$, (c) $LaAlO_3$-$SrTiO_3$(H-MBE)-$SrTiO_3$ and (d) $LaAlO_3$-$SrTiO_3$(PLD)-$SrTiO_3$ for various temperatures. The dotted line in (a) shows the border between n-type ($-\frac{1}{4}$) and p-type ($+\frac{1}{4}$) behavior. The measurements were performed by F. Gunkel at the Forschungszentrum in Jülich, Germany.

to high P_{O_2}. The plateau originates from the presence of mobile extrinsic carriers. It has been suggested that the mobile extrinsic carriers are a result from either lattice distortions or A-site cation intermixing.[135] For the PLD-$SrTiO_3$ heterostructure, the plateau is nearly absent above 950 K. This implies a mobile extrinsic donor dopant band is not created in $LaAlO_3$-$SrTiO_3$(PLD)-$SrTiO_3$. Whether extrinsic donors are absent or trapped is hard to resolve: the influence of the grown $SrTiO_3$ on the conductance is vanished by the bulk $SrTiO_3$. Below 950 K, the plateau of PLD grown $SrTiO_3$ heterostructure is attributed to the ionic conductivity contribution resulting from oxygen vacancy diffusion, similar to the $SrTiO_3$ single crystal.

Similar high temperature conductance analysis were carried out on $LaAlO_3$-$SrTiO_3$-LSAT heterostructures.[140] It appeared that the sheet electron density was P_{O_2} and temperature independent for reducing conditions. This supports the idea of a donor-type conduction mechanism at the $LaAlO_3$-$SrTiO_3$ interface, which could be provided by cation intermixing. Furthermore, the sheet carrier density decreased under oxidizing conditions. This indicates a complex charge compensation mechanism in the vicinity of the interface, involving the formation of Sr-vacancies at high oxygen partial pressures.[140] The alteration of the sheet carrier density was reversible, indicating reversibility of the formation of Sr-vacancies. Since the formation and annihilation of strontium vacancies appeared to take place at typical growth temperatures, they have to be considered in the discussion of the $LaAlO_3$-$SrTiO_3$ interface.

4.5 Discussion

To summarize: the main results, presented in sections 4.3 and 4.4, are:

- H-MBE grown $SrTiO_3$ film is slightly off-stoichiometric. The top-most plane of PLD $SrTiO_3$ is off-stoichiometric.
- An increase of the Ti/O ratio is observed for PLD grown $SrTiO_3$ in comparison to $SrTiO_3$ single crystal.
- Conducting interfaces are achieved in $LaAlO_3$-$SrTiO_3$ and $LaAlO_3$-$SrTiO_3$-LSAT heterostructures. The $LaAlO_3$-$SrTiO_3$ interfaces remained insulating on $SrTiO_3$, $NdGaO_3$ and $DyScO_3$.
- No potential build-up has been observed in $LaAlO_3$-$SrTiO_3$ heterostructures by XPS.
- The Ti^{3+} signal is reduced in modified $LaAlO_3$-$SrTiO_3$ heterostructures.
- $LaAlO_3$ grown by PLD in low oxygen pressure is La deficient.
- Mobile extrinsic carriers have been observed in $LaAlO_3$-$SrTiO_3$ and $LaAlO_3$-$SrTiO_3$(H-MBE)-$SrTiO_3$ at $\sim$900 K and 10^{-10}-10^{-3} mbar oxygen. The mobile extrinsic carriers were absent in $SrTiO_3$ and $LaAlO_3$-$SrTiO_3$(PLD)-$SrTiO_3$.

Table 4.3: Symmetry consequences of $SrTiO_3$ and $LaAlO_3$ due to two-dimensional thin film epitaxy.[116]

Substrate	$SrTiO_3$ structure	$LaAlO_3$ structure
$SrTiO_3$	cubic	monoclinic
$DyScO_3$	orthorhombic	triclinic
$NdGaO_3$	orthorhombic	triclinic
LSAT	tetragonal	monoclinic

4.5.1 $LaAlO_3$-$SrTiO_3$ under induced strain

In this chapter, it has been shown that the $SrTiO_3$ template influences the electronic properties of the $LaAlO_3$-$SrTiO_3$ interface significantly. The interface on LSAT and $SrTiO_3$ may become conducting, while the interface remained insulating on $NdGaO_3$ and $DyScO_3$. This suggests that the crystal structure of $SrTiO_3$ and $LaAlO_3$ may play an important role on the interfacial behavior. The theoretically predicted lattice type of $SrTiO_3$ and $LaAlO_3$ on the different substrates are given in Table 4.3. Reciprocal space maps showed that $LaAlO_3$ and $SrTiO_3$ were coherently grown and copied the in-plane lattice parameters. Therefore, the theoretically predicted crystal structures for $LaAlO_3$ and $SrTiO_3$ are expected to be present. Due to deformations in the $LaAlO_3$ and $SrTiO_3$ crystal structure, oxygen octahedra deformations are likely to be induced. Furthermore, $LaAlO_3$ induces octahedral rotations in the $SrTiO_3$ near the interface, as investigated by Jia *et al.*, but this may vary on the different $SrTiO_3$ templates.[12]

The oxygen octahedra of bulk $LaAlO_3$ are rotated: $a^-a^-a^-$ according to Glazer notation. By inducing strain, the octahedra rotation can be tuned. On cubic substrates under tensile strain, an $a^-a^-c^0$ tilt system is predicted, i.e. rotations around the $[110]_{pc}$ axes.[141] These rotations were observed experimentally by STEM on standard $LaAlO_3$-$SrTiO_3$ heterostructures.[12] Similar $LaAlO_3$ induced rotations are expected to occur in $LaAlO_3$-$SrTiO_3$-LSAT near the $LaAlO_3$-$SrTiO_3$ interface as both in-plane lattice parameters are equivalent in the heterostructures on LSAT. On $NdGaO_3$ and $DyScO_3$, the crystal structure of $LaAlO_3$ is expected to be triclinic, which could result in different octahedral rotations in $LaAlO_3$.

The $LaAlO_3$ induced oxygen octahedra rotations in $SrTiO_3$ are predicted to cause spontaneous polarization in the $SrTiO_3$ near the interface.[102, 106] As a result of polarization in the $SrTiO_3$, band bending is suggested to occur near the interface, which moves the impurity states into the $SrTiO_3$ conduction band deeper in the $SrTiO_3$. For the $LaAlO_3$-$SrTiO_3$ heterostructures under induced strain, the oxygen octahedra are expected to be deformed. Furthermore, deformation of the $LaAlO_3$ oxygen octahedra may change the induced deformation of the $SrTiO_3$ oxygen octahedra near the interface. This may change or even suppress the polarization in the $SrTiO_3$, which could clarify the differences in electronic transport between the heterostructures. The suggested variation of induced polarization may be established by optical second harmonic generation. Alteration in the oxygen octahedra rotations could be determined by, e.g., STEM-EELS.[12]

Additionally, X-ray photoelectron diffraction may be suitable to resolve octahedra rotations in the top 2 nm.

It has to be mentioned that, in contrast to the results shown here, Bark *et al.* achieved conducting $LaAlO_3$-$SrTiO_3$ interfaces on LSAT, Si as well as $NdGaO_3$.[142] In addition, they observed insulating $LaAlO_3$-$SrTiO_3$ interfaces on both $DyScO_3$ and $GdScO_3$. This implies that they only gained conducting interfaces when $SrTiO_3$ was grown under compressive strain. They observed an increase of the $LaAlO_3$ critical thickness for compressively strained heterostructures. A minimum of 5 monolayers $SrTiO_3$ was necessary to achieve conducting interfaces, independent of the substrate.

To understand the difference in electronic behavior between both studies, the differences in fabrication process were explored. In this chapter, the substrates were treated chemically and/or thermally before $SrTiO_3$ growth to achieve B-site termination. The surface of the subsequently grown $SrTiO_3$ was expected to remain mainly B-site terminated.[4] Bark *et al.* treated the $SrTiO_3$ surface chemically and thermally before $LaAlO_3$ growth.[142, 144] The surface treatment was essential to achieve conducting interfaces. Note that no chemical or thermal surface treatment of $SrTiO_3$-LSAT was necessary to achieve conducting $LaAlO_3$-$SrTiO_3$ interfaces in the study presented here. In addition, differences in $SrTiO_3$ fabrication process may have influenced the defect concentration and, consequently, the electronic properties of the interface.

4.5.2 $LaAlO_3$-$SrTiO_3$ on $SrTiO_3$

Above, deformations of the oxygen octahedra rotations were suggested to be responsible for the differences in electronic behavior between the strain induced $LaAlO_3$-$SrTiO_3$ heterostructures. However, this can not explain the insulating behavior of $LaAlO_3$-$SrTiO_3$-$SrTiO_3$ heterostructures. For these heterostructures, the $SrTiO_3$ and $LaAlO_3$ layers are expected to have similar crystal structure and oxygen octahedra rotations as in standard $LaAlO_3$-$SrTiO_3$ heterostructures. This implies that the $SrTiO_3$ crystal quality is also important to achieve conducting interfaces. In the $SrTiO_3$ films, the quality near the interface could have been improved or deteriorated in comparison to the $SrTiO_3$ substrate.

The suggested models which could clarify the interfacial conductivity are considered. First of all, intrinsic electronic reconstruction would occur due to the polar discontinuity between $SrTiO_3$ and $LaAlO_3$. However, this is not expected to be different for $LaAlO_3$-$SrTiO_3$-$SrTiO_3$, since polar $LaAlO_3$ is still grown on neutral, cubic $SrTiO_3$. Moreover, the lack of the potential build-up in the XPS measurements of any of the heterostructures implies that other reconstructions have to occur at the $LaAlO_3$-$SrTiO_3$ interface. Other models include the formation of defects, e.g. oxygen vacancies and La-Sr intermixing, to induce conductivity.

From STEM-EELS measurements, no clear difference in intermixing has been observed for PLD grown $SrTiO_3$-$LaAlO_3$ interfaces and standard $SrTiO_3$-$LaAlO_3$

[4] Note that it has been shown that the SrO coverage has to be close to one for achieving insulating interfaces.[143]

interfaces. This implies that defects gained by intermixing are not the sole origin for interfacial conductivity. Nevertheless, these defects may participate in the conducting behavior. HTEC measurements point to the creation of mobile carriers by A-site intermixing in standard $LaAlO_3$-$SrTiO_3$ and $LaAlO_3$-$SrTiO_3$(H-MBE). These mobile carriers were absent in $LaAlO_3$-$SrTiO_3$(PLD)-$SrTiO_3$. These defect induced carriers appeared to be mobile at high temperatures, meanwhile the role of oxygen vacancies could be neglected during the HTEC measurements. Therefore, the HTEC measurements do not directly prove that the interfacial conductivity at low temperatures is dominated by intermixing.

Beside intermixing, oxygen vacancies were suggested to be necessary to achieve conducting interfaces. In this chapter, the electronic properties versus growth pressure were determined for PLD grown $LaAlO_3$-$SrTiO_3$ on $SrTiO_3$ and LSAT substrates. The $LaAlO_3$-$SrTiO_3$ interfaces on LSAT became conducting when grown $\leq 10^{-5}$ mbar. On $SrTiO_3$, the interface remained insulating up to $> 1\times10^{-5}$ mbar. Decreasing the pressure even further, the results point to conducting $LaAlO_3$-$SrTiO_3$ interfaces. The pressure dependent transport behavior suggests that oxygen vacancies participate in the conducting behavior of modified $SrTiO_3$-$LaAlO_3$ interfaces. A lower oxygen growth pressure was necessary to achieve conductivity in the modified heterostructures. This implies that it is harder to form oxygen vacancies in grown $SrTiO_3$. This is in agreement with the lower Ti^{3+} signal observed by XPS and the increased O signal measured by STEM-EELS.

4.6 Conclusion

In this chapter, a clear influence of $SrTiO_3$ template on the $LaAlO_3$-$SrTiO_3$ interfacial behavior has been shown. Variations in crystal structure as well as defect concentration can turn the interface from metallic into insulating. Specific octahedra rotations in $SrTiO_3$ as well as in $LaAlO_3$ are suggested to be essential to mobilize the defect induced carriers. This fits with the polarization discontinuity model. Moreover, the formation of oxygen vacancies near the interface are proposed to be essential for achieving conducting interfaces. From XPS and STEM-EELS measurements, it is suggested that the number of oxygen vacancies is reduced in PLD grown $SrTiO_3$.

Chapter 5

Electron transfer from $LaTiO_3$ to $LaFeO_3$

Abstract

$LaFeO_3$ and $LaTiO_3$ are both insulators. The charge gap of $LaFeO_3$ is determined by the filled oxygen p band and the empty upper Fe d band. For $LaTiO_3$, the charge gap is determined by the partially filled lower Ti d band and the empty upper Ti d band. In $LaFeO_3$-$LaTiO_3$ heterostructures, alignment of their oxygen p-bands is proposed to occur near the interface due to continuation of the oxygen octahedra sublattice. As a result, the empty upper d band of $LaFeO_3$ is pulled below the energy level of the partially filled lower d band of $LaTiO_3$. Consequently, electron transfer from $LaTiO_3$ to $LaFeO_3$ is expected to occur, resulting in mixed valent Fe and Ti. A change in the occupation of the Fe d band in $LaFeO_3$ is suggested to modify the magnetic behavior. Here, $LaFeO_3$-$LaTiO_3$ heterostructures were fabricated by pulsed laser deposition. The proposed charge transfer was studied by X-ray photoelectron spectroscopy. Partly reduced Fe has been observed if $LaFeO_3$ was stacked adjacent to $LaTiO_3$ and the Fe^{2+} concentration strongly depended on the [Ti]/[Fe] ratio. In addition, the spectral weight of the partially filled Ti d band in the valence band spectra decreased as function of $LaFeO_3$ thickness. Both observations confirm the electron transfer from $LaTiO_3$ to $LaFeO_3$. So far, no clear variations in magnetic and electronic behavior have been observed, but may be realized in follow-up studies.

5.1 Introduction

The interface between $LaAlO_3$ and $SrTiO_3$ was discussed in the previous chapter. In those heterostructures, a polar discontinuity is present at the interface, which would result in a potential build-up. To avoid the potential build-up between $SrTiO_3$ and $LaAlO_3$, electronic reconstruction has been proposed to occur.[10] Experimentally, no clear indication for sole intrinsic electronic reconstruction has been observed, yet.[11] To investigate other intrinsic mechanisms which could result in electronic reconstruction at complex oxide interfaces, an iso-polar material

system, $LaFeO_3$-$LaTiO_3$, is presented in this chapter. For this specific heterostructure, charge transfer is proposed to occur as a result of oxygen p band alignment near the interface; no polar discontinuity has to be present.

The perovskite series $LaMO_3$ ($M = 3d$ transition metal ion, Ti-Cu) is of high interest since it has a wide variety of magnetic, electrical and structural properties.[145–148] In this chapter, the focus lies on $LaMO_3$, with M = Ti-Co. These materials are insulators due to strong electron-electron correlation. They have a partially filled d band which is split into Hubbard subbands, which are stacked between $4s$ and $2p$ bands.[148–150] The arrangement of these bands determines their insulating behavior. Zaanen, Sawatzky and Allen (ZSA) have pointed out that insulating $3d$-electron systems can be classified in two categories: Mott-Hubbard (MH) insulators and charge-transfer (CT) insulators.[149] The early transition metal oxides (M = Ti, V) fall into the MH class of compounds. Their charge gap is determined by the Hubbard splitting (U) of the d bands (d-d gap). The late transition metal oxides (M = Cr-Co) are CT insulators. Their charge transfer gap (Δ) is determined by the filled p band of the oxygen ligands and the unoccupied upper Hubbard $3d$ band (p-d gap). To summarize, the insulators are classified as MH for $U < \Delta$ and CT for $U > \Delta$.

As discussed in the previous two chapters, the combination of different materials can result in new material functionalities near the interface. In this chapter, heterostructures consisting of a MH and a CT insulator are discussed in more detail. The d-d band gaps of $LaTiO_3$ and $LaVO_3$ are rather small compared to the p-d band gaps of $LaFeO_3$ and $LaCrO_3$. On the other hand, the p-d band gaps of $LaTiO_3$ and $LaVO_3$ are much larger than those of the CT insulators, as shown in Table 5.1.

From a structural point of view, the MH insulator and the CT insulator share their oxygen octahedra at the interface in a MH-CT heterostructure.[151] Therefore, it is proposed that the p bands of the oxygen ligand in the MH insulator and the CT insulator align at the MH-CT interface. Due to alignment of the oxygen p bands, the empty upper d band of the CT insulator is expected to be pulled below the energy level of the partially filled lower d band of the MH insulator. Consequently, electron transfer from $LaTiO_3$ to $LaFeO_3$ is expected to occur. This is schematically depicted in Figure 5.1.

In $LaMO_3$, the $3d$ transition metal has an ionization state of M^{3+}. However, its ionization state can be tuned by controlled doping of the $LaMO_3$. In MH-CT heterostructures, the MH $3d$ element is suggested to be partially oxidized and the CT $3d$ element would be partially reduced as a result of the predicted charge transfer. The presence of mixed valent cations is expected to influence the physical properties. Controlled modification of the physical properties may be achieved by regulating the suggested charge transfer process.

To understand possible variations in the physical properties, the magnetic behavior of $LaFeO_3$ is taken as an example and discussed in more detail. $LaFeO_3$ is an antiferromagnetic insulator with a Néel temperature (T_N) of 740 K.[156] In $LaFeO_3$, Fe has a d^5 electron configuration, i.e. Fe^{3+}. As a result of sole Fe^{3+}, superexchange interaction between the Fe $3d$ orbitals through the oxygen $2p$ or-

Table 5.1: Physical properties of LaMO$_3$ at low temperatures. The charge gaps were determined by optical reflectivity. Data are taken from [148, 152–155].

LaMO$_3$	$3d^x$	electronic behavior	U (eV)	Δ (eV)	magnetic behavior
$LaTiO_3$	$3d^1$	MH	0.1	4.5	antiferromagnetic
$LaVO_3$	$3d^2$	MH	1.1	4.0	antiferromagnetic
$LaCrO_3$	$3d^3$	CT	-	3.4	antiferromagnetic
$LaMnO_3$	$3d^4$	CT	-	1.1	antiferromagnetic
$LaFeO_3$	$3d^5$	CT	-	2.2	antiferromagnetic
$LaCoO_3$	$3d^6$	CT	-	0.6	paramagnetic
$LaNiO_3$	$3d^7$	metallic	-	0	paramagnetic
$LaCuO_3$	$3d^8$	metallic	-	0	paramagnetic

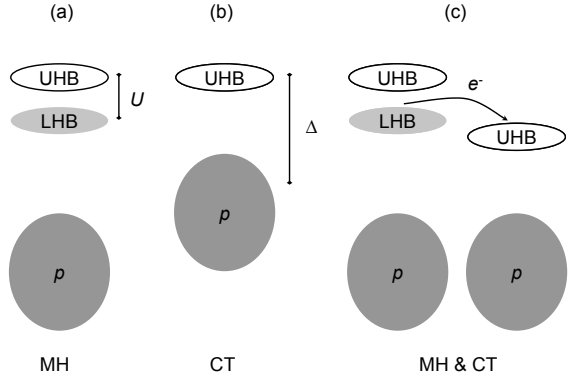

Figure 5.1: Band diagram of (a) a Mott-Hubbard insulator, (b) a charge-transfer insulator and (c) the combination of a Mott-Hubbard and a charge-transfer insulator. LHB denotes the (partially) filled lower Hubbard band, UHB denotes the empty upper Hubbard band.

bitals has to be considered. The electron spins interact through the oxygen anion, giving one σ and two π interactions. Due to the antiparallel alignment of the electron spins between the neighboring bands and the Pauli exclusion principle within the bands, the electrons show an antiparallel spin alignment. Moreover, Hund's coupling aligns all spins of a single cation into one direction (high spin), resulting in antiferromagnetic spin alignment. The magnetic structure of bulk $LaFeO_3$ is G-type; inter- and intralayer spin coupling are antiparallel.[154, 157]

In electron doped $LaFeO_3$, Fe^{3+} is partially reduced to Fe^{2+}, which results in unequally filled neighboring cations. Having unequally filled neighboring cations, double exchange interaction may be considered. Within each atom, all unpaired electrons strive to attain the configuration with the lowest energy. Therefore, all spins align parallel to each other conform Hund's rules. Subsequently, double exchange predicts that the mobile electrons hop from one cation to another without changing spin direction in order to reduce the kinetic energy. This indirect coup-

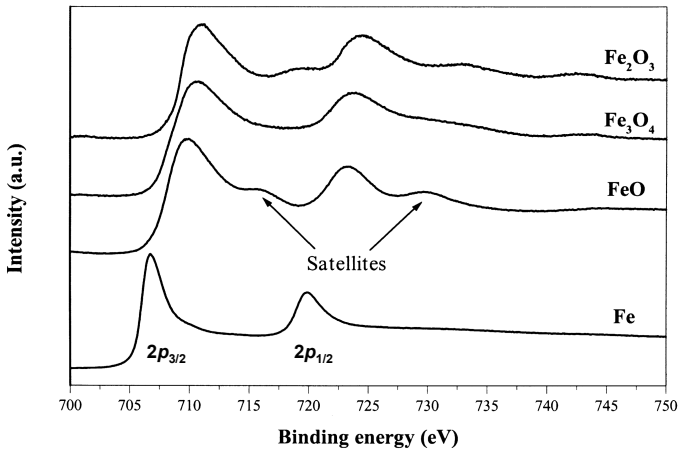

Figure 5.2: Fe $2p$ XPS spectra of Fe, FeO, Fe_2O_3 and Fe_3O_4. The Figure was reproduced with permission of ref. [159].

ling between the neighboring cations via the mobile electrons results in parallel alignment of spins of neighboring Fe ions and lowers the energy. The material becomes ferromagnetic and conducting. The magnetic behavior of electron doped $LaFeO_3$ in a MH-CT heterostructure is expected to depend on the doping concentration and the electron-electron interaction. To compare it with chemically doped $LaFeO_3$, Sr doping of $LaFeO_3$ results in an decreased T_N. Nevertheless, the material remained antiferromagnetic.[158]

The $3d$ elements are often studied by photoelectron spectroscopy. For example, the valence state of the elements can easily be determined, since their spectra differ in shape and energy. Additionally, satellite structures appear in the core level and valence band spectra. They reflect many-body effects arising from electron-electron interaction and hybridization of M $3d$-ligand p orbitals. A clear example of both the variation in valence state and satellite structure is given in Figure 5.2, where the iron spectra of metallic Fe, FeO (Fe^{2+}), Fe_2O_3 (Fe^{3+}) and Fe_3O_4 ($\frac{1}{3}$ Fe^{2+} and $\frac{2}{3}$ Fe^{3+}) are shown. Differences in peak position, peak shape as well as satellite structure are clearly visible for the different valence states.

In this chapter, results of MH-CT heterostructures are presented; $LaTiO_3$-$LaFeO_3$ was used as a model system. The heterostructures were studied by photoelectron spectroscopy and physical property measurements to investigate the suggested charge transfer in MH-CT heterostructures.

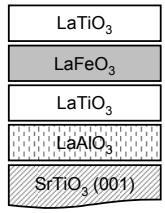

Figure 5.3: Schematic stacking of a $LaFeO_3$-$LaTiO_3$ heterostructure described in this chapter.

5.2 Fabrication

5.2.1 Substrates

$LaTiO_3$-$LaFeO_3$ heterostructures were grown by PLD on $SrTiO_3$ (001) and LSAT (001) single crystals. $SrTiO_3$ substrates were chemically and thermally treated resulting in well defined TiO_2 terminated surfaces.[21] LSAT substrates were annealed at 1050 °C for 10 hours under oxygen flow and are expected to be mainly B-site terminated (TaO_2-AlO_2).[118, 119] Singly terminated substrates are preferred for controlled growth and an atomically precise interface stacking. Note that in $LaTiO_3$-$LaFeO_3$ heterostructures, charge transfer is expected due to oxygen p band alignment, which should be independent of the atomic stacking at the interface. Moreover, the stacking of all $LaTiO_3$-$LaFeO_3$ interfaces can be given by TiO_2-LaO-FeO_2 as both materials have La at the A-site.

5.2.2 Growth

The heterostructures discussed in this chapter were grown by PLD in the COMAT system in Twente as well as the EMANUELA system in Würzburg (both designed by TSST, Enschede). The base pressure of the PLD chambers was below 5×10^{-8} mbar before growth. To allow comparison, the optical path, growth pressure, substrate temperature and substrate-to-target distance were kept constant for both setups. However, slight differences in the setup were present, since the constructions of the systems are not equal.

A buffer layer of $LaAlO_3$, 15 to 30 monolayers thick, was grown on the substrate to exclude contributions of the $SrTiO_3$ substrate in the XPS measurements. $SrTiO_3$ consists of Ti^{4+} and may obscure the Ti XPS spectra of $LaTiO_3$. Due to the large band gap of $LaAlO_3$ (5.4 eV), $LaAlO_3$ is expected to have no influence on the electron transfer from $LaTiO_3$ to $LaFeO_3$. A schematic view of the complete heterostructure is given in Figure 5.3. This stacking is used as a basis to study the charge transfer in $LaTiO_3$-$LaFeO_3$ heterostructures, unless explicitly stated otherwise. The $LaTiO_3$ layers were both kept at a thickness of two monolayers, while the thickness of the $LaFeO_3$ layer was varied.

$LaAlO_3$, $LaFeO_3$ and $LaTiO_3$ were grown at 700-750 °C by PLD and *in*

situ monitored by RHEED.[1] The $LaAlO_3$ layer was grown at 10^{-3} mbar oxygen with a fluence of 1.3 Jcm^{-2}. The $LaFeO_3$ and $LaTiO_3$ layers were grown at 2×10^{-6} to 1×10^{-3} mbar oxygen, with a fluence of 1.9 Jcm^{-2}. All layers were deposited with a repetition rate of 1 Hz. For $LaAlO_3$, a $LaAlO_3$ single crystal target was used. For $LaFeO_3$ and $LaTiO_3$, $LaFeO_3$ and $La_2Ti_2O_7$ sintered targets (Praxair electronics) were used. The extremely low growth pressure for $LaTiO_3$ and $LaFeO_3$ was chosen to ensure the fabrication of the perovskite phase of $LaTiO_3$.[160] At higher growth pressures and for thick films, the $La_2Ti_2O_7$ phase is expected to dominate. However, very thin $LaTiO_3$ films (<5 monolayers) can also be grown in the perovskite phase at higher oxygen pressures.[160]

In Figure 5.4a-d, clear RHEED oscillations of the different layers are shown. The RHEED patterns after growth were two-dimensional and comparable with the $SrTiO_3$ substrate pattern before growth (see Fig. 5.4e and f). The growth rate was similar in both PLD systems and constant in the 2×10^{-6}-1×10^{-3} mbar pressure regime; 0.023 nm/pulse for $LaAlO_3$, 0.029 nm/pulse for $LaTiO_3$ and 0.014 nm/pulse for $LaFeO_3$, using a spot size of 2.3 mm^2 on the target.

5.2.3 Surface morphology

The surface morphology was studied by AFM after growth. Smooth surfaces with a defined terrace structure, comparable with the substrate surface, were observed (see Fig. 5.4g). The terraces were separated by 0.4 nm high steps. This indicated layer-by-layer growth of each material, which is in agreement with the RHEED analysis.

5.2.4 Crystal structure

Both bulk $LaFeO_3$ and bulk $LaTiO_3$ are orthorhombic at room temperature, with a pseudocubic lattice parameter of ∼0.393 nm.[152, 161] On $SrTiO_3$, both materials are grown under compressive strain. For a single $LaTiO_3$-$LaFeO_3$ lattice, it is hard to distinguish the crystal structure by XRD. Therefore, XRD was done on a $[2\ LaTiO_3\times2\ LaFeO_3]_{15}$ superlattice grown on top of $SrTiO_3$-15 $LaAlO_3$.[2] The measurements were performed on a Bruker D8 Discover.

The θ-2θ XRD scan of the superlattice is shown in Figure 5.5a and b. The superlattice peaks, indicated by SL, are weakly visible in Figure 5.5a. These peaks appear because the scattering density of both materials is different. In this heterostructure, this difference only originates from Fe versus Ti, which have electron densities close to each other. The low intensity of the superlattice peaks indicate that the interfaces are slightly roughened. For a [2×2] superlattice, each perovskite unit cell is adjacent to an interface. As a result, superlattice peaks vanish already

[1] The heater set temperature was kept constant for all samples. Nevertheless, small variations in the substrate surface temperature was observed by measuring with an optical Pyrometer.

[2] For the superlattice, RHEED oscillations were observed and the pattern remained two dimensional. This was in agreement with its AFM height image where the terrace structure was still visible. The well defined growth of the superlattice is necessary for comparison with single lattices.

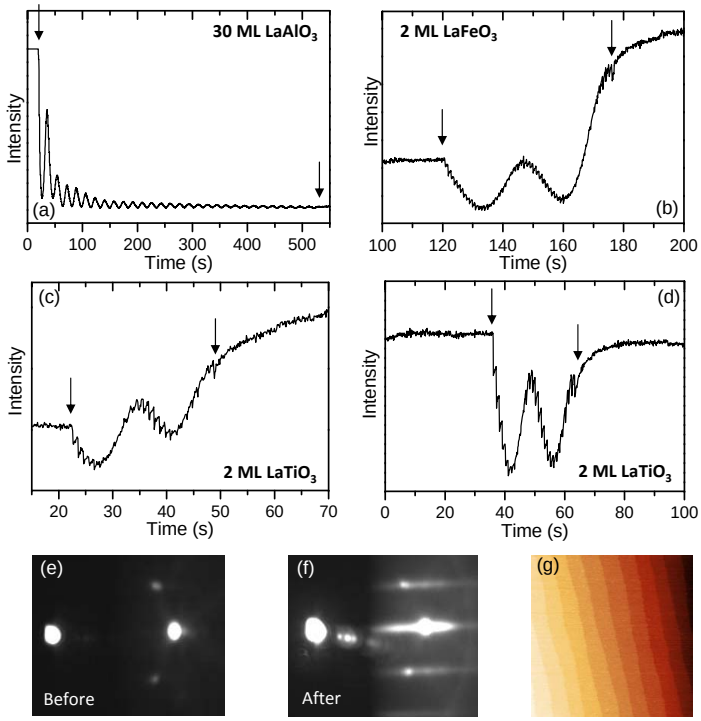

Figure 5.4: (a-d) RHEED oscillations of a 30 $LaAlO_3$-2 $LaTiO_3$-2 $LaFeO_3$-2 $LaTiO_3$ heterostructure grown on $SrTiO_3$ at 10^{-3} mbar, where (c) is of the bottom $LaTiO_3$ layer and (d) of the top $LaTiO_3$ layer. (e) and (f) RHEED patterns before and after growth, respectively. (g) AFM height image of a complete heterostructure grown on $SrTiO_3$.

by minor interface roughening. According to the RHEED data, it is expected that the roughness of the interface increases with the number of periods. In this chapter, the study is mainly focused on single $LaFeO_3$-$LaTiO_3$ heterostructures. For the single heterostructures, the interface roughness is expected to be negligible, which would be in agreement with their RHEED and AFM data.

Thickness interference fringes, corresponding to the (008) superlattice peak, were clearly visible (see Fig. 5.5b). Their period is in agreement with the total thickness of the superlattice. Reciprocal space maps verified that the superlattice was fully coherent with the underlaying $LaAlO_3$-$SrTiO_3$ template and showed an approximately tetragonal structure. From this, it is assumed that the single $LaFeO_3$-$LaTiO_3$ heterostructures are fully coherent as well. Due to biaxial compressive strain on the $LaTiO_3$-$LaFeO_3$ layers, both out-of-plane lattice parameters increased to 0.395 nm. The volume remained similar to the bulk value.

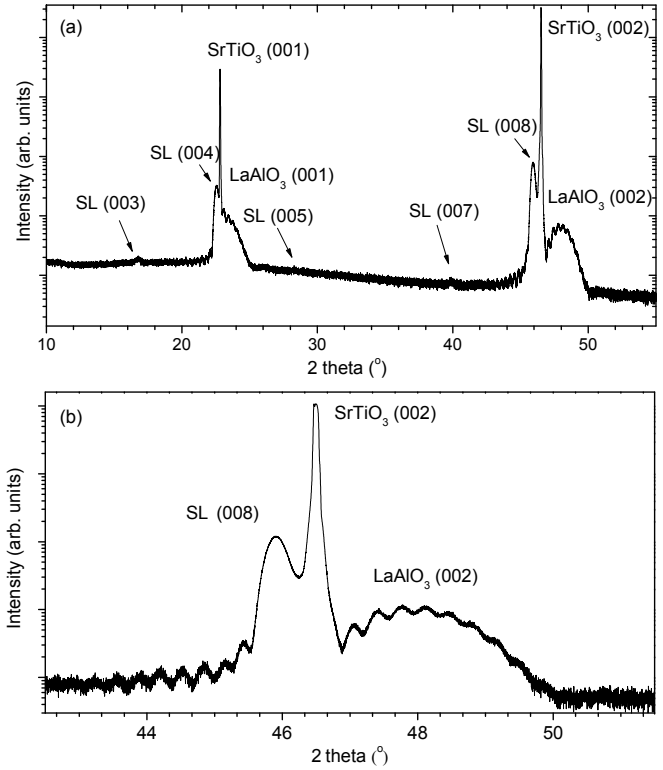

Figure 5.5: (a) shows a θ-2θ scan of $[(LaTiO_3)_2$-$(LaFeO_3)_2]_{15}$-15 $LaAlO_3$-$SrTiO_3$. (b) is a close-up of (a) along $SrTiO_3$ (002). SL denotes superlattice peak. The heterostructure was grown at 10^{-6} mbar.

5.3 Photoelectron Spectroscopy

To distinguish the presence of mixed valent transition metal oxides, the heterostructures were analyzed by XPS. *In situ* UPS and XPS measurements were done in Würzburg as well as in Twente. Both systems were designed by Omicron Nanotechnology GmbH, equipped with an EA 125 electron energy analyzer. For XPS, a monochromized Al Kα source (XM1000) was used as well as a non-monochromized Al Kα source. For UPS, a He plasma lamp (HIS13) operated at the He I (21.2 eV) excitation edge was used. The base pressure of both XPS chambers was below 10^{-10} mbar. The analyzers were calibrated with the use of an *in situ* sputter cleaned Au sample.

Hard X-ray photoelectron spectroscopy was performed at Desy in Hamburg (BW2 beamline). A monochromatic source with an excitation energy of 3500 eV was used. The analyzer (Scienta SES 200) was calibrated with a Au sample to the Au $4f_{7/2}$ line at 84.0 eV.

To overcome the charging effect of the insulating samples, a flood gun was used: a Flood Gun 15/40 (SPECS) in Würzburg and a CN 10 charge neutralizer system (Omicron Nanotechnology GmbH) in Twente. For each measurement the filament current, emission current and beam energy were optimized to minimize the FWHM of the peaks.

All spectra were aligned to the O $1s$ at 530.1 eV of $SrTiO_3$ single crystal. For charging samples, the scan time was reduced to avoid broadening of the spectra (max. 0.1 eV). For data analysis, a Shirley background was subtracted and the spectra were normalized to the total area. Note that normalization of the Fe $2p$ spectra are complicated due to different satellite structures of Fe^{2+} and Fe^{3+}. Moreover, the La MNN (at ∼740-800 eV) obscures the Fe $2p$ satellite structure when measuring with an Al Kα source.

5.3.1 Single films

$LaTiO_3$

The Ti $2p$ spectra of thin $LaTiO_3$ were studied. A thin $LaTiO_3$ film was chosen to ensure the perovskite phase.[160] The low oxygen growth pressure is expected to suppress the formation of the $La_2Ti_2O_7$ phase. Two monolayers of $LaTiO_3$ were grown on $LaAlO_3$-$SrTiO_3$ and studied by XPS. A $LaAlO_3$ buffer layer was used to reduce the Ti^{4+} signal of the $SrTiO_3$.

The Ti $2p$ spectrum of $LaTiO_3$ is shown in Figure 5.6a, where A-D mark the Ti $2p_{3/2}$ positions of several titanium oxides. The Ti $2p_{3/2}$ peak of $LaTiO_3$ has a relatively high binding energy for Ti^{3+}, ∼458.9 eV (B). For comparison, the Ti $2p_{3/2}$ of $SrTiO_3$ (Ti^{4+}) is at ∼459.9 eV (A). For $La_2Ti_2O_7$ (Ti^{4+}) the Ti $2p_{3/2}$ peak was observed at 458.4 eV (C), with O $1s$ at 529.9 eV.[162] At lower binding energy of the Ti $2p$ of $LaTiO_3$ (∼457 eV, D), spectral weight was observed. Modeling the Ti $2p$ with four Voight functions did not gave reasonable fits. This indicated that the spectral weight at lower binding energy does not originate from a lower Ti valence state, but that the Ti $2p$ peaks are asymmetric. Asymmetry may originate from, e.g., band bending or surface states. However, the absence of asymmetric La in the XPS spectra precludes band bending of $LaTiO_3$.

The corresponding valence band spectrum is shown in Figure 5.6b. No lower Hubbard band, originating from the Ti $3d^1$, is observed.[3] Lack of the lower Hubbard band points to an empty d shell, i.e. Ti^{4+}. This suggests that the $La_2Ti_2O_7$ phase was stabilized instead of the $LaTiO_3$ phase. From growth, the $LaTiO_3$ phase was expected to be stabilized as the film is very thin and grown at low oxygen pressure. Moreover, the XRD data of the superlattice do not indicate the presence of $La_2Ti_2O_7$.

It is remarkable that no clear Ti^{3+} features were observed in the Ti $2p$ as well as valence band spectra. The lack of Ti^{3+} features is similar to previous studies on $LaTiO_3$-$LaAlO_3$, where also no Ti^{3+} signal was observed for thin $LaTiO_3$ on $LaAlO_3$ in the core level XPS spectra[4].[163, 164] For these heterostructures, Has-

[3] Lack of the lower Hubbard band was independent of X-ray source.

[4] There is no information on the valence band XPS spectra for these samples.

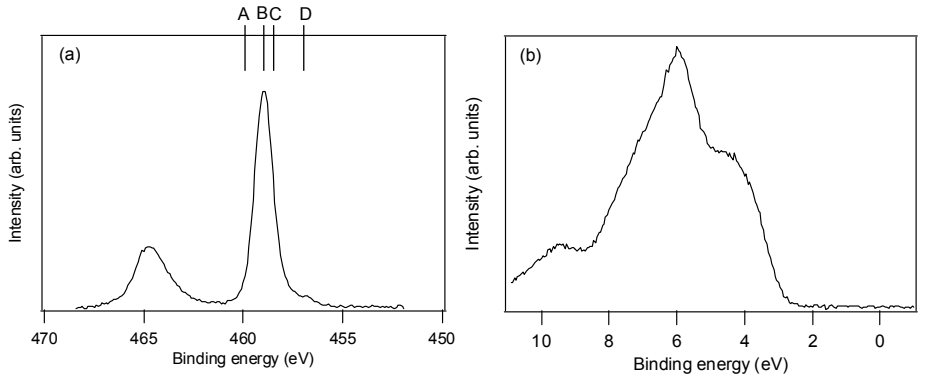

Figure 5.6: Bulk sensitive hard XPS spectra of thin $LaTiO_3$ on $LaAlO_3$-$SrTiO_3$ where (a) shows the Ti $2p$ and (b) the valence band spectrum. In (a), A marks the position of Ti $2p_{3/2}$ in $SrTiO_3$, B marks the Ti position observed in this $LaTiO_3$ film, C marks the Ti position in $La_2Ti_2O_7$ and D marks the asymmetry of the Ti $2p_{3/2}$ of $LaTiO_3$.

sink observed clear Ti^{3+} fingerprints by STEM-EELS measurements.[163]. Additionally, Ti^{4+} fingerprints were absent in those samples. STEM-EELS and growth analysis indicate that the Ti valence state of $LaTiO_3$ is hard to distinguish correctly by XPS.

$LaFeO_3$

A 30 monolayers thick $LaFeO_3$ film on $SrTiO_3$ was taken as a $LaFeO_3$ reference sample. Its Fe $2p$ spectrum is shown in Figure 5.7a. The binding energy of the Fe $2p_{3/2}$ is comparable to Fe_2O_3, implying Fe^{3+}. The typical satellite structure for Fe^{3+} with octahedral symmetry at $\sim$720 eV confirms the Fe^{3+} ionization state.[165] In the Fe $2p_{3/2}$ peak, fine structure was observed due to multiplet splitting.[166] From fitting, the separation between the fine structure peaks has been determined to be $\sim$1 eV (see section 5.3.4). Furthermore, the FWHM of the Fe peaks of $LaFeO_3$ were small in comparison to those of simple Fe oxides. The reduced FWHM is probably due to a change in electrostatic interactions, crystal field splitting or spin-orbit coupling between the $2p$ core hole and unpaired $3d$ electrons of the photoionized Fe cation.[166]

In the valence band spectrum (Fig. 5.7b), the $LaFeO_3$ charge transfer band, marked by the arrow, was observed. No spectral weight was observed close to the Fermi level (0 eV), which is consistent with the insulating behavior of $LaFeO_3$.

5.3.2 $LaTiO_3$-$LaFeO_3$ on $LaAlO_3$-$SrTiO_3$

In this section, XPS spectra of various $LaTiO_3$-$LaFeO_3$ heterostructures are presented. Figure 5.8a shows the Fe $2p$ spectrum of a $LaFeO_3$-$LaTiO_3$ heterostructure. In comparison to thick $LaFeO_3$, an extra peak at $\sim$708 eV is observed, which

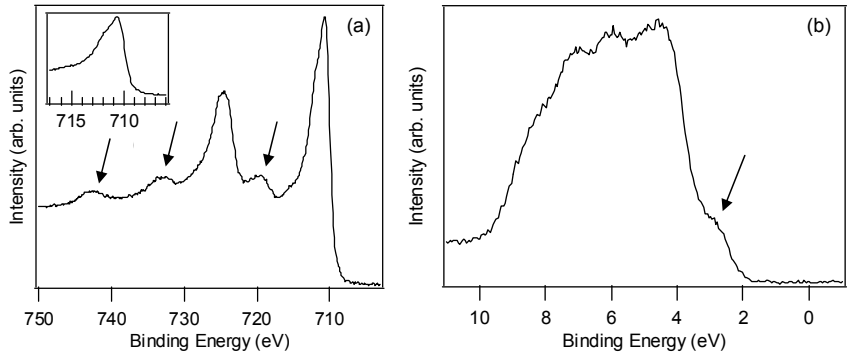

Figure 5.7: Bulk sensitive hard XPS spectra of thick $LaFeO_3$ on $SrTiO_3$, where (a) shows the Fe $2p$ and (b) the valence band spectrum. The arrow in (a) points to Fe^{3+} satellites, in (b) to the charge transfer band. The inset of (a) shows a close-up of the Fe $2p_{3/2}$ spectrum.

is marked by the circle in Figure 5.8a. The extra peak points to the presence of Fe^{2+}. To distinguish whether the Fe^{2+} signal originated from the proposed charge transfer, a $LaFeO_3$-$LaAlO_3$ heterostructure has been fabricated for comparison. $LaAlO_3$ is a wide band gap insulator with only single valent cations. Therefore, no charge transfer to Fe is expected to occur in this heterostructure. The lack of charge transfer was confirmed by XPS, since only Fe^{3+} was observed in $LaAlO_3$-$LaFeO_3$ (see Fig. 5.8a).

To study the $LaTiO_3$-$LaFeO_3$ heterostructures in more detail, the thickness of the $LaFeO_3$ layer has been varied while the thickness of the $LaTiO_3$ layers was kept at two unit cells. As shown in Figure 5.8b marked by the arrow, the Fe^{2+} signal reduced with increase of the $LaFeO_3$ thickness. The reduction may be clarified by two different scenarios. The first possibility is that doping only occurs at the interface. As a result, the Fe^{2+} signal reduces in comparison to the Fe^{3+} signal for thicker $LaFeO_3$ films, but the total Fe^{2+} concentration remains constant. In the second scenario, the electron doping of Fe depends on the $[LaTiO_3]/[LaFeO_3]$ ratio. The number of electrons that is transferred to the $LaFeO_3$ layer remains constant, but is homogeneously spread in the $LaFeO_3$ film. As a result, the $[Fe^{2+}]/[Fe^{3+}]$ ratio reduces by increase of the $LaFeO_3$ thickness.

Angular resolved XPS was performed to obtain information on the distribution of the Fe^{2+} ions in the $LaFeO_3$ film. Figure 5.9 shows angular resolved Fe spectra of a $LaTiO_3$-4 $LaFeO_3$-$LaTiO_3$ heterostructure. A slight increase of Fe^{2+} was observed in the surface sensitive measurement. This could point to a higher Fe^{2+} concentration in the top $LaFeO_3$ monolayer in comparison to the underlying $LaFeO_3$ layers. As the $LaFeO_3$ film was only four monolayers thick, each $LaFeO_3$ monolayer was close to a $LaTiO_3$-$LaFeO_3$ interface. If doping only occurs at the interface, the observed angle dependence should be more pronounced for thicker $LaFeO_3$ films. Nevertheless, the minor difference between bulk and surface sensi-

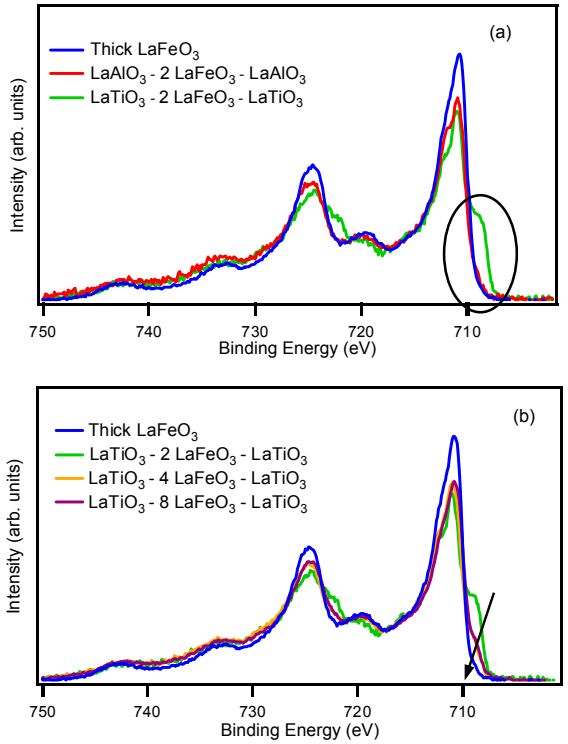

Figure 5.8: (a) Fe 2*p* hard XPS spectra of thick $LaFeO_3$, $LaAlO_3$-2 $LaFeO_3$-$LaAlO_3$ and $LaTiO_3$-2 $LaFeO_3$-$LaTiO_3$. The circle marks the Fe^{2+} signal of $LaTiO_3$-2 $LaFeO_3$-$LaTiO_3$. (b) Fe 2*p* XPS spectra of $LaTiO_3$-$LaFeO_3$ with $LaFeO_3$ thicknesses of 2, 4 and 8 monolayers. The $LaTiO_3$ layers were kept at two unit cells. The arrow indicates the decrease of Fe^{2+} with increase of $LaFeO_3$ thickness. All measurements were done at normal emission.

tive measurement can not explain the pronounced reduction in electron doped Fe for increased $LaFeO_3$ thicknesses. The influence of the $[LaTiO_3]/[LaFeO_3]$ ratio, is expected to give significant differences in $[Fe^{2+}]/[Fe^{3+}]$ ratio. The negligible angle dependence in XPS suggests a nearly homogeneous Fe^{2+} distribution over the $LaFeO_3$ film. Therefore, it is proposed that the variation in the $[LaTiO_3]/[LaFeO_3]$ ratio is the most likely explanation for the trend shown in Figure 5.8b.

The above mentioned results were on heterostructures where $LaFeO_3$ was sandwiched between two $LaTiO_3$ layers. To investigate whether only one of the $LaTiO_3$ layers is crucial for Fe reduction, heterostructures without top or bottom $LaTiO_3$ were fabricated. In both heterostructures, Fe^{2+} was present, but the Fe^{2+} concentration was reduced compared to sandwiched $LaFeO_3$ of equal thickness. This suggests that charge transfer occurs at both interfaces.

According to the proposed charge transfer mechanism, besides mixed valent

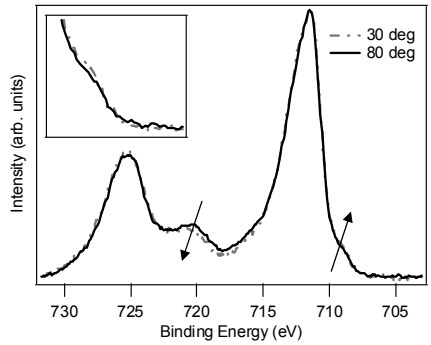

Figure 5.9: Fe $2p$ XPS spectra of $LaTiO_3$-4 $LaFeO_3$-$LaTiO_3$ at different angles. The inset shows a close-up of the Fe^{2+} signal at 709 eV.

Fe, also mixed valent Ti should be present in MH-CT heterostructures. In Figure 5.10, the Ti $2p$ spectrum of a $LaTiO_3$-$LaFeO_3$ heterostructure is compared to thin $LaTiO_3$. For the $LaTiO_3$-$LaFeO_3$ heterostructures, no asymmetry at lower binding energy was observed in the Ti $2p_{3/2}$ spectra. The Ti $2p$ spectra of the heterostructures could be well fitted by two Voight functions, independent of the $LaFeO_3$ thickness; one for $2p_{3/2}$ and one for $2p_{1/2}$. A single, symmetric Ti $2p_{3/2}$ peak suggests the absence of mixed valent Ti, which does not agree with the proposed charge transfer and the corresponding Fe $2p$ spectra. In the valence band spectra, no lower Hubbard band of $LaTiO_3$ was observed, which is similar to the valence band spectra of thin $LaTiO_3$ on $LaAlO_3$-$SrTiO_3$ (see section 5.3.1). As mentioned before, the valence state of Ti in $LaTiO_3$-$LaAlO_3$ was hard to distinguish by XPS (see section 5.3.1). A similar effect may occur for $LaTiO_3$-$LaFeO_3$ on $LaAlO_3$-$SrTiO_3$.

The Ti $2p$ and valence band spectra point to the presence of Ti^{4+} and the lack of Ti^{3+}. However, their corresponding Fe spectra suggest that not each Ti $3d^1$ electron is transferred to the empty Fe upper Hubbard band, as Fe^{3+} is still clearly present in, e.g., $LaTiO_3$-2 $LaFeO_3$. Oxygen vacancies or oxygen interstitials, resulting in $LaTiO_{3-\delta}$ or $La_2Ti_2O_7$, would also change the Ti valence state. To study their presence, the oxygen growth pressure (10^{-6}-10^{-3} mbar) and cool-down procedure (with and without post anneal) were varied. The Ti $2p$ spectra appeared to be independent of growth pressure and cool-down procedure, suggesting that oxygen vacancies as well as interstitials are unlikely to be the origin of the single Ti $2p_{3/2}$ spectrum.

Fe reduction

During the exposure of $LaTiO_3$-$LaFeO_3$ heterostructures to X-rays, reduction of Fe^{3+} to Fe^{2+} was observed, which stabilized to a certain $[Fe^{2+}]/[Fe^{3+}]$ equilibrium. It is important to mention that all shown Fe spectra so far were taken after stabilizing. In this section, the Fe reduction during X-ray exposure is discussed to verify

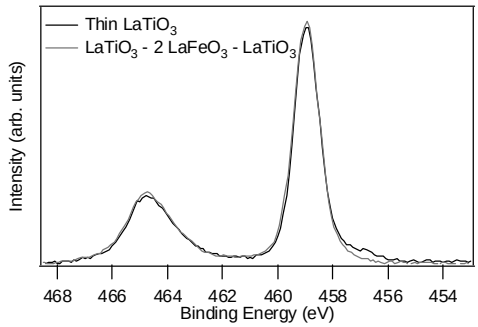

Figure 5.10: The Ti $2p$ XPS spectra of a thin $LaTiO_3$ layer and a $LaTiO_3$-2 $LaFeO_3$-$LaTiO_3$ heterostructure.

whether the observed Fe reduction originates from the proposed charge transfer or is a result of beam damage.

The Fe reduction was slow (in the order of hours, even using a synchrotron source) and occurred locally; only where the X-rays bombarded the surface. During the measurements, Fe saturated to a certain $[Fe^{2+}]/[Fe^{3+}]$ equilibrium. As shown in Figure 5.8b, the $[Fe^{2+}]/[Fe^{3+}]$ equilibrium depended on the [Ti]/[Fe] ratio of the heterostructure. Unlike the reduction in $LaTiO_3$-$LaFeO_3$ heterostructures, Fe reduction was absent in the reference samples. Thick $LaFeO_3$ and $LaAlO_3$-$LaFeO_3$ were stable during X-ray exposure. This suggests that the reduction of Fe is not solely due to X-ray damage.

The reduction of Fe over time is clearly visible in Figure 5.11a. It shows the Fe $2p$ spectrum at the beginning of the XPS measurement and after reaching the $[Fe^{2+}]/[Fe^{3+}]$ equilibrium. The reduced Fe state remained stable for at least 60 hours after switching off the X-rays and storing the samples in ultra high vacuum. Exposing $LaTiO_3$-$LaFeO_3$ heterostructures to air, Fe^{2+} reoxidized to Fe^{3+}. With these observations, the question raised whether the reduction is an ionic or an electronic process.

Oxygen transfer from $LaFeO_3$ towards $LaTiO_3$ would result in Fe^{2+}. Oxidation of $LaTiO_3$ could occur, since the $La_2Ti_2O_7$ phase is energetically favorable, and results in oxidation of Ti^{3+} to Ti^{4+}.[160] However, no variation in the Ti $2p$ spectra was observed during X-ray exposure. The La and Al spectra were stable during X-ray exposure as well. Moreover, the Fe reduction was independent of growth pressure and post annealing.

To understand the Fe reduction in more detail, the source energy was varied. Instead of using an X-ray source (1486.8 eV for a lab source, 3500 eV for a synchrotron source), a He I source (21.2 eV) has been used. Exposing the heterostructures to this energy, ionic migration is expected to be negligible in comparison to electronic transfer. To distinguish the variation of the Fe state by He I exposure, the Fe $2p$ spectrum was shortly measured by XPS before and after He I exposure. After He I exposure, the Fe was partially reduced to Fe^{2+}, as shown in

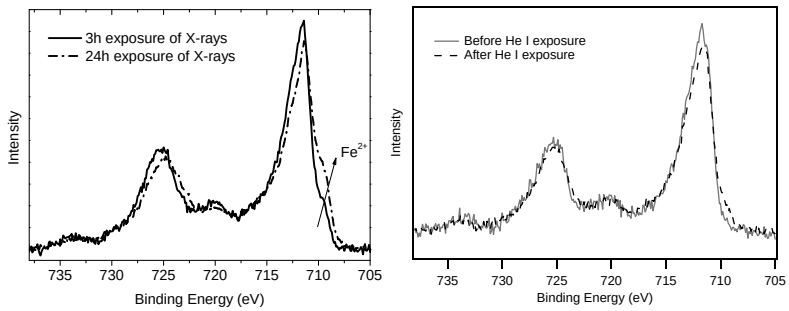

Figure 5.11: (a) Fe 2*p* XPS spectra of a $LaTiO_3$-2 $LaFeO_3$-$LaTiO_3$ heterostructure after different exposure times, measured in Würzburg at an emission angle of 39°. After 24 hours, the reduction was saturated. (b) Fe 2*p* XPS spectra of $LaTiO_3$-8 $LaFeO_3$-$LaTiO_3$ before and after exposure to He I. The exposure duration was approximately three hours.

Figure 5.11b. This observation suggests strongly that the Fe reduction is a result of electron transfer.

Reduction of cations in oxide crystals by X-ray exposure has been observed in previous studies.[167–170] An extensively studied example is the reduction of Cu in oxides.[167–169] Cu can completely reduce from Cu^{2+} to metallic Cu when adsorbates are present at the surface. This is also consistent with observations on thin $SrCuO_2$ films.[5] Measuring the Cu spectra *in situ* by XPS directly after growth, clear Cu^{2+} features were present and remained stable during the measurements. After storing the sample for at least one week in vacuum (max. 10^{-9} mbar), Cu reduced slowly to Cu^{+} during X-ray exposure. Moreover, additional O and C peaks were observed by XPS, indicating surface contamination. For *ex situ* measured $SrCuO_2$ samples, the reduction speed was increased. Exposing the reduced copper oxides to air, the Cu remained Cu^{+}, i.e. it did not reoxidize to Cu^{2+}.[167] Comparing the reduced Cu oxides with $LaTiO_3$-$LaFeO_3$ heterostructures, clear differences in reduction process were observed. No differences between *in situ* and *ex situ* measurements were observed for $LaTiO_3$-$LaFeO_3$ heterostructures and Fe^{2+} reoxidized to Fe^{3+} after exposure to air. Furthermore, in contrast to Cu, Fe did not reduce completely to Fe^{2+}, but reached a certain $[Fe^{2+}]/[Fe^{3+}]$ equilibrium. Therefore, it is suggested that the reduction of Cu and Fe are based on different mechanisms.

For MoO_3 and WO_3, a reduction of the cations was observed as well during X-ray exposure.[170] After exposing the crystal surfaces to air, W and Mo reoxidized, which is analogous to Fe. Fleisch *et al.* realized stabilization of the reduced Mo and

[5] $SrCuO_2$ was grown on $SrTiO_3$ (001) with and without $LaAlO_3$ buffer layer (in Twente). Capping $SrCuO_2$ with two monolayers of crystalline $SrTiO_3$ did not change the Cu reduction process.

W states by exposing to H_2. With this result, they suggested that the reduction by X-rays was caused by internal electron transfer from oxygen to metal orbitals, creating isolated +5 states and O^-. By exposing the reduced state to H_2, H_2O was created, destroying the reversibility of the photochromism. However, the proposed charge transfer from O to Mo or W was not supported by the O 1s XPS spectra, since the O 1s did not changed during X-ray exposure. To clarify their results, they suggested that the created holes at the O site are either distributed over the oxygen lattice or diffused into the bulk of the oxide. A similar mechanism may occur in the $LaFeO_3$-$LaTiO_3$ heterostructures. Nevertheless, in comparison to MoO_3 and WO_3, the reduction mechanism of $LaFeO_3$-$LaTiO_3$ is probably more complex as cation interactions and band alignment may also participate in the reduction process.

As mentioned above, no changes in Ti, Al and La spectra were observed during the XPS measurements. This suggests that La, Al and Ti have steady valence states during XPS measurements. Moreover, no clear change in the O 1s spectra has been observed. If the proposed mechanism for WO_3 and MO_3 is applicable for the $LaTiO_3$-$LaFeO_3$ heterostructures, homogeneous hole distribution over the thin $LaFeO_3$ layer is expected to give a distinct variation in O 1s XPS signal. Therefore, changes in O valence state are expected to be diffused into the sample. Note that no information on the chemical state of the $SrTiO_3$ substrate could be obtained by the XPS measurements as $SrTiO_3$ was deeply buried from the surface. To distinguish the influence of the $SrTiO_3$ substrate on the reduction process, comparable heterostructures were fabricated on other templates. These results are presented in the next section.

5.3.3 $LaTiO_3$-$LaFeO_3$ on $LaAlO_3$-LSAT and $SrTiO_3$

To study the effect of the template on the charge transfer in $LaTiO_3$-$LaFeO_3$ heterostructures, the heterostructures were fabricated on $SrTiO_3$ and $LaAlO_3$-LSAT. Growing the heterostructure directly on $SrTiO_3$, effect of the $LaAlO_3$-$SrTiO_3$ interface can be excluded. Another approach, $SrTiO_3$ replacing by LSAT, was also used. LSAT has lattice parameters close to $SrTiO_3$ (see Table 4.1) and both crystals are cubic. As a consequence, no big changes in the crystal structure of the heterostructure are expected. In contrast to $SrTiO_3$, LSAT is insulating even at high temperatures, which is expected to suppress accumulation of charge into the LSAT substrate during growth.[24] The heterostructures on LSAT were charging during X-ray exposure. A flood gun was used to avoid peak broadening.

In Figure 5.12a, the Fe 2p spectra of $LaFeO_3$-$LaTiO_3$ heterostructures on $LaAlO_3$-$SrTiO_3$ and $LaAlO_3$-LSAT are compared. A clear increase of Fe^{2+} signal is observed for the heterostructure on LSAT and the Fe 2p spectrum of this sample was stable during X-ray exposure. Decreasing the $[LaTiO_3]/[LaFeO_3]$ ratio for heterostructures on $LaAlO_3$-LSAT, partial Fe reduction was present during X-ray exposure .

Figure 5.12b compares $LaTiO_3$-2 $LaFeO_3$ heterostructures grown on $SrTiO_3$ and $LaAlO_3$-$SrTiO_3$. On $SrTiO_3$, the iron valence state was predominantly Fe^{2+}. In addition, the Fe^{2+} signal was stable during the measurement, i.e. no Fe reduc-

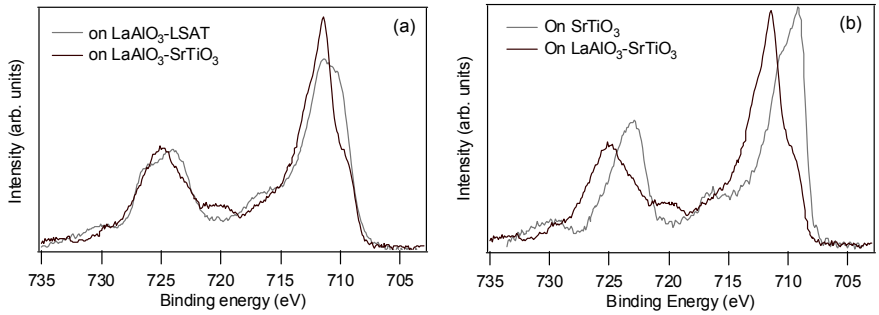

Figure 5.12: Fe $2p$ spectra of $LaTiO_3$-2 $LaFeO_3$-$LaTiO_3$ grown on (a) $LaAlO_3$-$SrTiO_3$ and $LaAlO_3$-LSAT, and on (b) $LaAlO_3$-$SrTiO_3$ and $SrTiO_3$. The measurements were performed *in situ* at an emission angle of 39°.

tion by X-ray exposure has been observed. Also $LaTiO_3$-4 $LaFeO_3$ on $SrTiO_3$ was already reduced before X-ray exposure. The reduced Fe states were instable in air for both heterostructures. Increasing the $LaFeO_3$ thickness to 8 monolayers, Fe reduction by X-ray exposure was observed *in situ* and similar to the behavior discussed in section 5.3.2.

Comparing the Fe spectra of the heterostructures on different templates, clear variations are observed. The stability during X-ray exposure and the $[Fe^{2+}]$ concentration varied clearly form template to template. This indicates that the template has a distinct influence of reduction process.

Besides a variation in the Fe spectra, a variation in the Ti spectra may be present for the heterostructures on different templates. Studying the Ti and valence band spectra of $LaFeO_3$-$LaTiO_3$ on $SrTiO_3$, clear differences have been observed in comparison to similar heterostructures on $LaAlO_3$-$SrTiO_3$. The Ti $2p_{3/2}$ peak was asymmetric to lower binding energy and the lower Hubbard band was present in the valence band spectra (see Fig. 5.13a and b). The presence of the lower Hubbard band implies that Ti in $LaTiO_3$ is at least partially 3+, though the Ti valence state is not evident from the Ti $2p$ spectra. Increasing the $LaFeO_3$ thickness, the asymmetry of the Ti peak and the spectral weight of the lower Hubbard band decreased. Since the spectral weight of the lower Hubbard band is a result of the total number of Ti d^1 electrons, a decrease in signal for thicker $LaFeO_3$ films support the electron transfer from $LaTiO_3$ to $LaFeO_3$. For the heterostructures on $LaAlO_3$-LSAT, no lower Hubbard band was observed.

5.3.4 Fits of Fe $2p$ spectra

To quantify the $[Fe^{2+}]/[Fe^{3+}]$ ratio, the Fe $2p_{3/2}$ spectra were fitted, as shown in Figure 5.14. To fit the spectra, a Shirley-type background was subtracted. Six Voight functions were used to fit the Fe $2p_{3/2}$ peak and the Fe^{2+} satellite. Three Voight functions (1-3) were used for Fe^{3+} $2p_{3/2}$ and two Voight functions (5 and 6) for the Fe^{2+} $2p_{3/2}$ peak. As a result, the observed multiplet splitting could

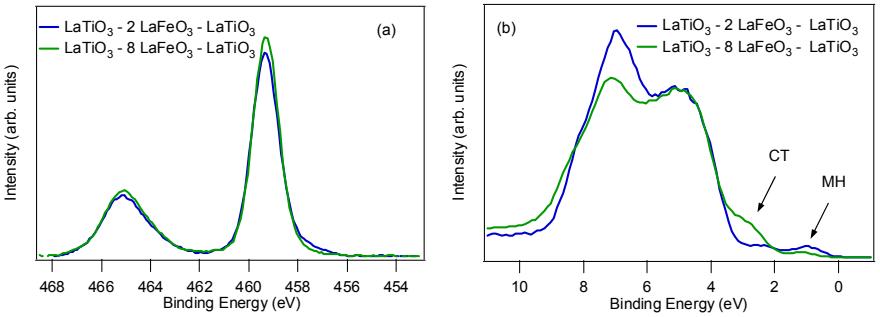

Figure 5.13: *In situ* XPS spectra of $LaTiO_3$-$LaFeO_3$ heterostructures grown on $SrTiO_3$. (a) Ti $2p$ and (b) valence band spectra. In the valence band spectra, CT points to the oxygen p band of $LaFeO_3$, MH points to the lower Hubbard band of $LaTiO_3$. The measurements were performed at an emission angle of 39°.

be taken into account.[166] One Voight function (4) was used to fit the remained area at higher binding energy. This area has been suggested to originate from Fe ions located near the surface or interface due to decreased crystal field energy.[171] Moreover, this Voight function included the spectral weight of the Fe^{2+} satellite. After optimizing, the separation between the multiplet peaks was fixed at 1 eV for all samples as well as the separation between Fe^{2+} and Fe^{3+} at 2.1 eV. The Lorentzian and Gaussian fit parameters were optimized for the heterostructures on $LaAlO_3$-$SrTiO_3$ and applied to all heterostructures. As a result, only the area below each Voight function could be varied. Note that function (4) was allowed to vary in peak position, as the position was expected to vary with Fe^{2+} concentration and $LaFeO_3$ thickness.

Figure 5.14 shows the Fe fits of thick $LaFeO_3$ and $LaTiO_3$-2 $LaFeO_3$ on $LaAlO_3$-$SrTiO_3$. Only four Voight functions (1-4) were used in the optimized fit for $LaFeO_3$, pointing to the absence of Fe^{2+}. In $LaTiO_3$-2 $LaFeO_3$, the saturated $[Fe^{2+}]$ was approximately 26%. An overview of $[Fe^{2+}]/[Fe^{3+}]$ ratios, obtained from the optimized fits, are shown in Table 5.2.

It has to be mentioned that the given fit parameters were not well applicable for highly electron doped heterostructures on $SrTiO_3$. According to Gupta *et al.*, the Fe^{2+} $2p_{3/2}$ should be split in three peaks.[166] The fit parameters were optimized for relatively low Fe^{2+} concentrations. Having a relatively low $[Fe^{2+}]$, it was hard to determine the multiplet splitting of Fe^{2+} properly and, therefore, it was chosen to use only two Voight functions for Fe^{2+}. For high Fe^{2+} concentrations, three Voight functions should be used to obtain proper fits. However, the multiplet splitting was hard to determine properly due to low statistics. Furthermore, no pure Fe^{2+}-perovskite-type oxide is known, to my knowledge, which could be used as reference. The given $[Fe^{2+}]/[Fe^{3+}]$ ratios for highly reduced Fe in the $LaTiO_3$-$LaFeO_3$ heterostructures are most likely below the actual value.

In Table 5.2, a small, but distinct Fe^{2+} concentration is given for the $LaAlO_3$-$LaFeO_3$ heterostructure, while no Fe^{2+} was expected. It has to be mentioned

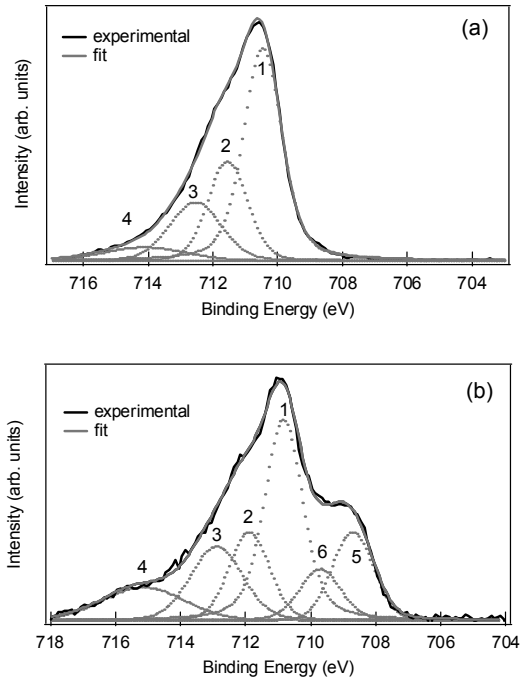

Figure 5.14: Experimental Fe $2p_{3/2}$ XPS spectra and their corresponding fits. (a) $LaFeO_3$ and (b) $LaTiO_3$-2 $LaFeO_3$-$LaTiO_3$ on $LaAlO_3$-$SrTiO_3$. The dotted lines show the results of individual Voight functions. The labels 1-6 correspond to the numbers given in the text.

that Fe ions with a reduced oxidation state could be formed by the production of defects in neighboring sites, which would result in spectral weight at lower binding energy.[171] It has been suggested that this can be fitted by a single Voight function.[171] For the optimized fit of $LaAlO_3$-2 $LaFeO_3$, only one Voight function (6) was necessary to fit the spectral weight at lower binding energy; the area below (5) was negligible. In $LaAlO_3$-2 $LaFeO_3$, each Fe ion was adjacent to a $LaAlO_3$ layer. As a consequence, symmetry changes are expected to have a significant influence on the Fe spectrum. Therefore, the spectral weight at lower binding energy is proposed not to originate from electron transfer of $LaAlO_3$ to $LaFeO_3$. In $LaFeO_3$-$LaTiO_3$ heterostructures, the spectral weight at lower binding energy could not be fitted by a single Voight function. For these heterostructures, it is suggested that the effect of symmetry breaking is negligible in comparison to the proposed electron transfer. For thick $LaFeO_3$, the influence of symmetry breaking at the surface is expected to have a negligible influence, as the $LaFeO_3$ film was 30 monolayers thick and measured by hard XPS.

The $[Fe^{2+}]/[Fe^{3+}]$ ratios, given in Table 5.2, are shown in Figure 5.15 as function of the [Ti]/[Fe] ratio. The clear differences indicate that the template as

Table 5.2: An overview of the fitted $[Fe^{2+}]/[Fe^{3+}]$ ratios of $LaTiO_3$-$LaFeO_3$ heterostructures on different templates. All results are of saturated Fe $2p_{3/2}$ spectra. The [Ti]/[Fe] ratios were determined by growth analysis.

	[Ti]/[Fe]	$[Fe^{2+}]/[Fe^{3+}]$
Reference samples		
Thick $LaFeO_3$	-	0
$LaAlO_3$-2 $LaFeO_3$	-	0.05
On $LaAlO_3$-$SrTiO_3$		
$LaTiO_3$-2 $LaFeO_3$	2	0.35
$LaTiO_3$-4 $LaFeO_3$	1	0.15
$LaTiO_3$-8 $LaFeO_3$	0.5	0.10
On $SrTiO_3$		
$LaTiO_3$-2 $LaFeO_3$	2	1.7
$LaTiO_3$-4 $LaFeO_3$	1	0.96
$LaTiO_3$-8 $LaFeO_3$	0.5	0.11
On $LaAlO_3$-LSAT		
$LaTiO_3$-2 $LaFeO_3$	2	0.54

well as the [Ti]/[Fe] ratio determine the observed $[Fe^{2+}]$ concentration. The heterostructures on $LaAlO_3$-substrate showed a significant lower $[Fe^{2+}]$ than the heterostructures on $SrTiO_3$. This suggests that $LaAlO_3$ suppressed the formation of Fe^{2+}. Also the influence of the substrate can not be neglected. The $[Fe^{2+}]$ on $LaAlO_3$-LSAT is significantly higher than on $LaAlO_3$-$SrTiO_3$. The difference may be caused by the electrical behavior of the substrate.

If each Ti^{3+} ion would donate one electron to an Fe^{3+} ion, the $[Fe^{2+}]/[Fe^{3+}]$ ratio should be equal to 1 for 2 $LaTiO_3$-8 $LaFeO_3$-2 $LaTiO_3$ heterostructures. This is clearly not in agreement with the experimental results. This implies that not each Ti^{3+} ion donated an electron to Fe^{3+}, which also clarifies the spectral weight in the valence band spectra originating from the Ti d^1 (see Fig. 5.13b).

5.4 Physical Properties

5.4.1 Magnetic properties

The magnetic properties of several heterostructures on $LaAlO_3$-LSAT and $SrTiO_3$ were measured with a vibrating sample magnetometer (VSM) option of a Quantum Design PPMS. The temperature dependent magnetization was measured at a fixed field of 2500-5000 Oe. Moreover, the magnetization versus field (up to 10,000 Oe) was measured at different temperatures. According to Hund's coupling, all spins within a single Fe cation are aligned parallel. As a result, the number of unpaired spins for Fe^{3+} is 5 and for Fe^{2+} 4.

On $LaAlO_3$-LSAT, the heterostructure showed diamagnetic or ferromagnetic behavior at room temperature. Cooling down to 5 K, the magnetic moment of the heterostructures increased gradually. Comparing the heterostructures with a

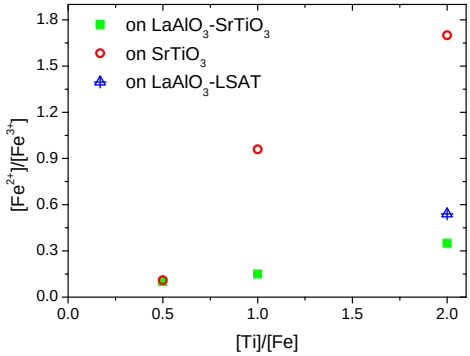

Figure 5.15: The $[Fe^{2+}]/[Fe^{3+}]$ as function of the [Ti]/[Fe] for $LaTiO_3$-$LaFeO_3$ heterostructures on different templates.

bare LSAT substrate, similar magnetic behavior was observed for both kind of samples (see also ref. [172]). In addition, Khalid *et al.* reported that LSAT crystals can show ferromagnetic, diamagnetic or paramagnetic behavior, depending on the impurities.[172] As the observed saturated magnetic signal was too high to originate only from the heterostructure, it is expected that the observed magnetic moment originated mainly from the LSAT substrate; signal from $LaFeO_3$ is expected to be negligible. On $SrTiO_3$, the samples showed paramagnetic behavior with a magnetic moment which was too high to originate only from $LaFeO_3$. In addition, the signal was comparable with a damaged sample holder.[6]

From the VSM measurements, no magnetic signal could be clearly pointed to the $LaTiO_3$-$LaFeO_3$ heterostructures. The total magnetic moment of the heterostructures was very small or $LaFeO_3$ and $LaTiO_3$ remained antiferromagnetic. A decrease in T_N of $LaFeO_3$ may occur in the heterostructures. However, this is hard to measure in the current setup. The paramagnetic to antiferromagnetic transition of bulk $LaFeO_3$ is at 740 K, which is outside the range of the used PPMS.[156]

The lack of clear changes in magnetic behavior may be explained by several scenarios. First of all, the $LaFeO_3$ films were very thin, $\leq$8 unit cells. For many ferromagnetic materials, a minimum film thickness is necessary before turning ferromagnetic.[7, 173] Secondly, it has been shown that the T_N of $LaFeO_3$ changes by doping, for example by Sr. In $La_{1-x}Sr_xFeO_3$, T_N decreases gradually with increase of doping, but remains antiferromagnetic.[158] A similar effect may be present in electron depod $LaFeO_3$. In the current setup, however, it hard to detect a possible change of T_N since the system is limited to temperatures up to 350 K. Finally, the reduced Fe appeared to be instable in air. Fe was completely reoxidized to Fe^{3+} after exposure to air. As a result, possible changes in the magnetic behavior are also eliminated.

[6] Bended or cut plastic colorless drinking straws, used as sample holder, gave a paramagnetic signal.

5.4.2 Electronic properties

$LaTiO_3$ and $LaFeO_3$ are both insulators, but $LaTiO_3$ can become metallic as a result of off-stoichiometry.[174] By charge transfer from $LaTiO_3$ to $LaFeO_3$, the filling of the $LaTiO_3$ and $LaFeO_3$ Hubbard bands is changed. The change in band filling could induce variations in the electronic behavior. The electronic transport properties were measured using a 4-probe Van der Pauw method with ultrasonically wire-bonded aluminum wires as electrodes. The electrical transport and Hall-effect measurements were performed in a Quantum Design PPMS in the temperature range from 300 K down to 2 K with magnetic fields up to 9 T.

Growing the heterostructures at 10^{-6} mbar on $SrTiO_3$ and $LaAlO_3$-$SrTiO_3$, the samples showed metallic behavior which was dominated by $SrTiO_{3-\delta}$. Increasing the growth pressure of the heterostructures on $LaAlO_3$-$SrTiO_3$ to 10^{-3} mbar oxygen, the electronic behavior was comparable to the electronic behavior of a thick $LaAlO_3$-$SrTiO_3$ interface.[66] To cancel the influence of the template on the electronic behavior, the heterostructures on $LaAlO_3$-LSAT were studied. Here, the influence of the template is expected to be negligible since $LaAlO_3$ and LSAT are highly insulating. It appeared that the$LaFeO_3$-$LaTiO_3$ heterostructures were insulating as well. The resistance at room temperature was above the detection limit, even when $LaFeO_3$ and $LaTiO_3$ were grown at 10^{-6} mbar oxygen. This suggests that both $LaFeO_3$ and $LaTiO_3$ films were insulating, which is comparable to their bulk behavior. This indicates that the oxygen stoichiometry of $LaTiO_3$ is close to 1.

5.5 Conclusions and Outlook

In this chapter, electron transfer from the lower Hubbard band of $LaTiO_3$ to the upper Hubbard band of $LaFeO_3$ is suggested to occur in $LaFeO_3$-$LaTiO_3$ heterostructures as a result of oxygen p band alignment. XPS measurements have shown that iron is indeed reduced to Fe^{2+} when being adjacent to $LaTiO_3$, while Fe ions remained oxidized (Fe^{3+}) in bulk $LaFeO_3$ and $LaFeO_3$-$LaAlO_3$ heterostructures. In addition, the valence band spectra indicated that the extra electrons on the Fe-site originated from the partially filled Ti d band. The electron transfer hypothesis was strengthened by the dependence of the $[Fe^{2+}]/[Fe^{3+}]$ ratio on the [Ti]/[Fe] ratio.

It appeared that Fe reduced during X-ray exposure to Fe^{2+} up to a certain $[Fe^{2+}]/[Fe^{3+}]$ equilibrium and Fe^{2+} was unstable in air. The reduction process could be tuned by changing the template and [Ti]/[Fe] ratio. Since the reduction was also observed *in situ* directly after growth, the influence of adsorbates is expected to be negligible. No changes in the Al, Ti and La spectra were observed. This indicated that oxygen migration or electron transfer occurred. As the reduction was independent of growth pressure and cool-down procedure, electron transfer is most likely. The heterostructures were insulating and no clear magnetic signal was observed. The absence of variations in the magnetic and electronic behavior could be clarified by the instability of Fe^{2+} in air.

Below, several suggestions for follow-up studies are given. First of all, the reduced $LaFeO_3$ state should be stabilized, i.e. reoxidation of Fe in air has to be avoided. This might be achieved by capping the heterostructure with, e.g., Al_2O_3. It has been shown that Al_2O_3 capping can prevent reactions between air and film.[175] Having a stabilized heterostructure, changes in the magnetic and electronic properties are expected to be present and can be explored in more detail.

The $[Fe^{2+}]/[Fe^{3+}]$ equilibrium depended on both the [Ti]/[Fe] ratio and the template. The dependence on the [Ti]/[Fe] ratio can be explained by the proposed charge transfer. The influence of the template is less understood, so far. Preliminary results indicated a decrease of $[Fe^{2+}]$ when a $LaAlO_3$ buffer layer was adjacent to the heterostructure. Moreover, the use of $SrTiO_3$ or LSAT resulted in different doping concentrations of $LaFeO_3$. It is expected that the influence of the template can be controlled by variations of substrate and buffer layer material, buffer layer thickness and substrate crystal orientation. Their exact influence has to be investigated. Here, heterostructures were fabricated in the $[001]_{pc}$. Variation of the growth direction, e.g. $[110]_{pc}$ and $[111]_{pc}$, may increase the charge transfer and, as a consequence, influence the physical properties of the heterostructure. The ferromagnetic ordering may occur in a specific crystal direction. Note that bulk $LaFeO_3$ does not show any direction preference as it is G-type antiferromagnetic; each ion has six antiparallel nearest neighbors.[154]

Up to now, the valence band spectra are not well understood. Due to the alignment of the oxygen p bands, a change in the valence band spectra should be observed, like variations in spectral weight, shifts or broadening of the bands. XPS measurements on a larger diversity of $LaTiO_3$ and $LaFeO_3$ thickness combinations may show a clear trend in these possible variations.

According to the proposed charge transfer from MH to CT insulator, the system can be expanded to $LaVO_3$ and $LaCrO_3$, a MH insulator and CT insulator respectively. The advantage of $LaVO_3$ is its extensively studied V $2p$ XPS spectra.[64] Therefore, $LaVO_3$ is expected to give more insight in the behavior of the MH insulator in the MH-CT heterostructures. Replacing $LaFeO_3$ by $LaCrO_3$ is expected to be helpful for investigation of the physical properties. In comparison to $LaFeO_3$, $LaCrO_3$ has a much lower T_N ($\sim$300 K).[156, 176] Consequently, a decrease of T_N, as a result of electron doping, can easily be investigated by VSM measurements. Furthermore, ferromagnetic behavior has been observed in chemically doped $LaCrO_3$, which is not the case for chemically doped $LaFeO_3$.[176]

Finally, beside experimental studies, density functional theory (DFT) calculations can give more insight in the charge transfer model. For example, calculations on exact band alignment at the interface versus thickness of the MH and CT insulator are useful. The outcome can be used to optimize the [MH]/[CT] ratio to increase the total charge transfer.

Bibliography

[1] E. B. Johnson, "Hearing on nanotechnology: The state of nano-science and its prospects for the next decade," http://ftp.resource.org/gpo.gov/hearings/106h/60678.txt.

[2] R. P. Feynman, "There's plenty of room at the bottom," http://www.its.caltech.edu/∼feynman/plenty.html.

[3] D. M. Eigler and E. K. Schweizer, "Positioning single atoms with a scanning tunnelling microscope," Nature **344**, 524–526 (1990).

[4] J. Kanamori, "Superexchange interaction and symmetry properties of electron orbitals," Journal of Physics and Chemistry of Solids **10**, 87–98 (1959).

[5] K. Ueda, H. Tabata, and T. Kawai, "Ferromagnetism in $LaFeO_3$-$LaCrO_3$ superlattices," Science **280**, 1064–1066 (1998).

[6] G. Rijnders and D. H. A. Blank, "Materials science: Build your own superlattice," Nature **433**, 369–370 (2005).

[7] J. Xia, W. Siemons, G. Koster, M. R. Beasley, and A. Kapitulnik, "Critical thickness for itenerant ferromagnetism in ultrathin films of $SrRuO_3$," Physical Review B **79**, 140 407(R) (2009).

[8] J. H. Haeni, P. Irvin, W. Chang, R. Uecker, P. Reiche, Y. L. Li, S. Choudhury, W. Tian, M. E. Hawley, B. Craigo, A. K. Tagantsev, X. Q. Pan, S. K. Streiffer, L. Q. Chen, S. W. Kirchoefer, J. Levy, and D. G. Schlom, "Room-temperature ferroelectricity in strained $SrTiO_3$," Nature **430**, 758–761 (2004).

[9] E. Bousquet, M. Dawber, N. Stucki, C. Lichtensteiger, P. Hermet, S. Gariglio, J.-M. Triscone, and P. Ghosez, "Improper ferroelectricity in perovskite oxide artificial superlattices," Nature **452**, 732–736 (2008).

[10] A. Ohtomo and H. Y. Hwang, "A high-mobility electron gas at the $LaAlO_3$/$SrTiO_3$ heterointerface," Nature **427**, 423–426 (2004).

[11] Y. Segal, J. H. Ngai, J. W. Reiner, F. J. Walker, and C. H. Ahn, "X-ray photoemission studies of the metal-insulator transition in $LaAlO_3$/$SrTiO_3$ structures grown by molecular beam epitaxy," Physical Review B **80**, 241 107 (2009).

[12] C. L. Jia, S. B. Mi, M. Faley, U. Poppe, J. Schubert, and K. Urban, "Oxygen octahedron reconstruction in the $SrTiO_3$/$LaAlO_3$ heterointerfaces investigated using aberration-corrected ultrahigh-resolution transmission electron microscopy," Physical Review B **79**, 081 405 (2009).

[13] N. Nakagawa, H. Hwang, and D. Muller, "Why some interfaces cannot be sharp," Nature Materials **5**, 204–209 (2006).

[14] J. E. Kleibeuker, G. Koster, W. Siemons, D. Dubbink, B. Kuiper, J. L. Blok, C.-H. Yang, J. Ravichandran, R. Ramesh, J. E. ten Elshof, D. H. A. Blank, and G. Rijnders, "Atomically defined rare-earth scandate crystal surfaces," Advanced Functional Materials **20**, 3490–3496 (2010).

[15] J. G. Bednorz and K. A. Müller, "Possible high Tc superconductivity in the Ba-La-Cu-O system," Zeitschrift für Physik B Condensed Matter **64**, 189–193 (1986).

[16] J. H. Park, E. Vescovo, H. J. Kim, C. Kwon, R. Ramesh, and T. Venkatesan, "Direct evidence for a half-metallic ferromagnet," Nature **392**, 794–796 (1998).

[17] W. J. Merz, "The electric and optical behavior of $BaTiO_3$ single-domain crystals," Physical Review **76**, 1221 (1949).

[18] H. N. Lee, H. M. Christen, M. F. Chisholm, C. M. Rouleau, and D. H. Lowndes, "Strong polarization enhancement in asymmetric three-component ferroelectric superlattices," Nature **433**, 395–399 (2005).

[19] D. P. Norton, B. C. Chakoumakos, J. D. Budai, D. H. Lowndes, B. C. Sales, J. R. Thompson, and D. K. Christen, "Superconductivity in $SrCuO_2$-$BaCuO_2$ superlattices: Formation of artificially layered superconducting materials," Science **265**, 2074–2077 (1994).

[20] M. Kawasaki, K. Takahashi, T. Maeda, R. Tsuchiya, M. Shinohara, O. Ishiyama, T. Yonezawa, M. Yoshimoto, and H. Koinuma, "Atomic control of the $SrTiO_3$ crystal surface," Science **266**, 1540–1542 (1994).

[21] G. Koster, B. L. Kropman, G. J. H. M. Rijnders, D. H. A. Blank, and H. Rogalla, "Quasi-ideal strontium titanate crystal surfaces through formation of strontium hydroxide," Applied Physics Letters **73**, 2920–2922 (1998).

[22] J. Chang, Y.-S. Park, and S.-K. Kim, "Atomically flat single-terminated $SrTiO_3$ (111) surface," Applied Physics Letters **92**, 152 910 (2008).

[23] A. Biswas, P. B. Rossen, C.-H. Yang, W. Siemons, M.-H. Jung, I. K. Yang, R. Ramesh, and Y. H. Jeong, "Universal Ti-rich termination of atomically flat $SrTiO_3$ (001), (110), and (111) surfaces," Applied Physics Letters **98**, 051 904 (2011).

[24] J. H. Ngai, T. C. Schwendemann, A. E. Walker, Y. Segal, F. J. Walker, E. I. Altman, and C. H. Ahn, "Achieving A-site termination on $La_{0.18}Sr_{0.82}Al_{0.59}Ta_{0.41}O_3$ substrates," Advanced Materials **22**, 2945–2948 (2010).

[25] D. G. Schlom, L.-Q. Chen, C.-B. Eom, K. M. Rabe, S. K. Streiffer, and J.-M. Triscone, "Strain tuning of ferroelectric thin films," Annual Review of Materials Research **37**, 589–626 (2007).

[26] S. J. May, J. W. Kim, J. M. Rondinelli, E. Karapetrova, N. A. Spaldin, A. Bhattacharya, and P. J. Ryan, "Quantifying octahedral rotations in strained perovskite oxide films," Physical Review B **82**, 014 110 (2010).

[27] J. He, A. Borisevich, S. V. Kalinin, S. J. Pennycook, and S. T. Pantelides, "Control of octahedral tilts and magnetic properties of perovskite oxide heterostructures by substrate symmetry," Physical Review Letters **105**, 227 203 (2010).

[28] K. J. Choi, M. Biegalski, Y. L. Li, A. Sharan, J. Schubert, R. Uecker, P. Reiche, Y. B. Chen, X. Q. Pan, V. Gopalan, L.-Q. Chen, D. G. Schlom, and C. B. Eom, "Enhancement of ferroelectricity in strained $BaTiO_3$ thin films," Science **306**, 1005–1009 (2004).

[29] C. Adamo, X. Ke, H. Q. Wang, H. L. Xin, T. Heeg, M. E. Hawley, W. Zander, J. Schubert, P. Schiffer, D. A. Muller, L. Maritato, and D. G. Schlom, "Effect of biaxial strain on the electrical and magnetic properties of (001) $La_{0.7}Sr_{0.3}MnO_3$ thin films," Applied Physics Letters **95**, 112 504 (2009).

[30] R. Uecker, B. Veličkov, D. Klimm, R. Bertram, M. Bernhagen, M. Rabe, M. Albrecht, R. Fornari, and D. G. Schlom, "Properties of rare-earth scandate single crystals (Re=Nd-Dy)," Journal of Crystal Growth **310**, 2649–2658 (2008).

[31] S.-i. Karimoto and M. Naito, "Electron-doped infinite-layer thin films with T_C over 40 K grown on $DyScO_3$ substrates," Applied Physics Letters **84**, 2136–2138 (2004).

[32] S. Venkatesan, B. J. Kooi, J. T. M. D. Hosson, A. H. G. Vlooswijk, and B. Noheda, "Substrate influence on the shape of domains in epitaxial $PbTiO_3$ thin films," Journal of Applied Physics **102**, 104 105 (2007).

[33] R. Dirsyte, J. Schwarzkopf, G. Wagner, R. Fornari, J. Lienemann, M. Busch, and H. Winter, "Thermal-induced change in surface termination of $DyScO_3(110)$," Surface Science **604**, L55–L58 (2010).

[34] B. Veličkov, V. Kahlenberg, R. Bertram, and M. Bernhagen, "Crystal chemistry of $GdScO_3$, $DyScO_3$, $SmScO_3$ and $NdScO_3$," Zeitschrift für Kristallographie **222**, 466–473 (2007).

[35] A. H. G. Vlooswijk, *Structure and domain formation in ferroelectric thin films*, Ph.D. thesis, University of Groningen (2009).

[36] M. D. Biegalski, J. H. Haeni, S. Trolier-McKinstry, D. G. Schlom, C. D. Brandle, and A. J. Ven Graitis, "Thermal expansion of the new perovskite substrates $DyScO_3$ and $GdScO_3$," Journal of Material Research **20**, 952–958 (2005).

[37] D. Taylor, "Thermal expansion data VIII. Complex oxides, ABO_3, the perovskites," Transactions and Journal of the British Ceramic Society **84**, 181–188 (1985).

[38] M. Raekers, K. Kuepper, S. Bartkowski, M. Prinz, A. V. Postnikov, K. Potzger, S. Zhou, A. Arulraj, N. Stüßer, R. Uecker, W. L. Yang, and M. Neumann, "Electronic and magnetic structure of $R ScO_3$ (R=Sm, Gd, Dy) from x-ray spectroscopies and first-principles calculations," Physical Review B **79**, 125 114 (2009).

[39] X. Ke, C. Ademo, D. G. Schlom, M. Bernhagen, R. Uecker, and P. Schiffer, "Low temperature magnetism in the perovskite substrate $DyScO_3$," Applied Physics Letters **94**, 152 503 (2009).

[40] C. Zhao, T. Witters, H. Brijs, H. Bender, M. Richard, O. Caymax, T. Heeg, J. Schubert, V. V. Afanas'ev, A. Stesmans, and D. G. Schlom, "Ternary rare-earth metal oxide high-k layers on silicon oxide," Applied Physics Letters **86**, 132 903 (2005).

[41] D. Lide, *CRC Handbook of Chemistry and Physics CD-ROM Version 2010* (Taylor and Francis, 2009).

[42] L. Pauling, *The nature of the chemical bond* (Cornell University press, 1960), 3rd edn.

[43] T. Ohnishi, K. Shibuya, M. Lippmaa, D. Kobayashi, H. Kumigashira, M. Oshima, and H. Koinuma, "Preparation of thermally stable TiO_2-terminated $SrTiO_3(100)$ substrate surfaces," Applied Physics Letters **85**, 272–274 (2004).

[44] B. Kuiper, J. L. Blok, H. J. W. Zandvliet, D. H. A. Blank, G. Rijnders, and G. Koster, "Self-organization of $SrRuO_3$ nanowires on ordered oxides," MRS Communications **1**, 17–21 (2011).

[45] J. E. Kleibeuker, B. Kuiper, P. Tinnemans, P. B. Rossen, S. Harkema, W. Siemons, G. Portale, J. Ravichandran, J. M. Szepieniec, R. Ramesh, E. Vlieg, D. H. A. Blank, G. Koster, and G. Rijnders, "Structure of singly terminated polar $DyScO_3$ (110) surfaces," (Submitted).

[46] E. Vlieg, "A (2+3)-type surface diffractometer: Mergence of the z-axis and (2+2)-type geometries," Journal of Applied Crystallography **31**, 198–203 (1998).

[47] E. Vlieg, "*ROD*: a program for surface X-ray crystallography," Journal of Applied Crystallography **33**, 401–405 (2000).

[48] J. Rabalais, *Principles and applications of ion scattering spectrometry: surface chemical and structural analysis* (Wiley, 2003).

[49] G. Rijnders, D. H. A. Blank, J. Choi, and C.-B. Eom, "Enhanced surface diffusion through termination conversion during epitaxial $SrRuO_3$ growth," Applied Physics Letters **84**, 505–507 (2004).

[50] R. Bachelet, F. Sanchez, J. Santiso, C. Munuera, C. Ocal, and J. Fontcuberta, "Self-assembly of $SrTiO_3$ (001) chemical-terminations: A route for oxide-nanostructure fabrication by selective growth," Chemistry of Materials **21**, 2494–2498 (2009).

[51] W. Siemons, *Nanoscale properties of complex oxide films*, Ph.D. thesis, University of Twente (2008).

[52] J. Choi, C. B. Eom, G. Rijnders, H. Rogalla, and D. H. A. Blank, "Growth mode transition from layer by layer to step flow during the growth of heteroepitaxial $SrRuO_3$ on (001) $SrTiO_3$," Applied Physics Letters **79**, 1447–1449 (2001).

[53] W. Hong, H. N. Lee, M. Yoon, H. M. Christen, D. H. Lowndes, Z. Suo, and Z. Zhang, "Persistent step-flow growth of strained films on vicinal substrates," Physical Review Letters **95**, 095 501 (2005).

[54] P. Jakob and Y. J. Chabal, "Chemical etching of vicinal Si(111): Dependence of the surface structure and the hydrogen termination on the pH of the etching solutions," Journal of Chemical Physics **95**, 2897–2909 (1991).

[55] J. Broekmaat, *In-situ growth monitoring with Scanning Force Microscopy during pulsed laser deposition*, Ph.D. thesis, University of Twente (2008).

[56] G. Koster and G. Rijnders, *Reflection High Energy Electron Diffraction* in *In situ* characterization of thin film growth (Woodhead Publishing, 2012).

[57] A. Gozar, G. Logvenov, V. Y. Butko, and I. Bozovic, "Surface structure analysis of atomically smooth $BaBiO_3$ films," Physical Review B **75**, 201 402(R) (2007).

[58] I. K. Robinson, "Crystal truncation rods and surface roughness," Phys. Rev. B **33**, 3830–3836 (1986).

[59] R. Feidenhans'l, "Surface structure determination by X-ray diffraction," Surface Science Reports **10**, 105 – 188 (1989).

[60] E. Vlieg, "Understanding crystal growth in vacuum and beyond," Surface Science **500**, 458 – 474 (2002).

[61] R. P. Liferovich and R. H. Mitchell, "A structural study of ternary lanthanide orthoscandate perovskites," Journal of Solid State Chemistry **177**, 2188 – 2197 (2004).

[62] P. T. Tinnemans, S. Harkema, H. Graafsma, A. Janssens, G. Portale, and E. Vlieg, "Annealed (110) $DyScO_3$ surface morphology and initial growth dynamics upon thin film growth," (To be published).

[63] Y. Chen, N. Pryds, J. E. Kleibeuker, G. Koster, J. Sun, E. Stamate, B. Shen, G. Rijnders, and S. Linderoth, "Metallic and insulating interfaces of amorphous $SrTiO_3$-based oxide heterostructures," Nano letters **11**, 3774–3778 (2011).

[64] A. Müller, H. Boschker, F. Pfaff, S. Glawion, G. Berner, G. Koster, G. Gorgoi, W. Drube, G. Rijnders, M. Kamp, D. H. A. Blank, M. Sing, and R. Claessen, "Electrostatic doping of a Mott insulator: Electronic reconstruction in $LaVO_3/SrTiO_3$," Submitted.

[65] A. D. Caviglia, S. Gariglio, C. Cancellieri, B. Sacépé, A. Fête, N. Reyren, M. Gabay, A. F. Morpurgo, and J.-M. Triscone, "Two-dimensional quantum oscillations of the conductance at $LaAlO_3/SrTiO_3$ interfaces," Physical Review Letters **105**, 236 802 (2010).

[66] A. Brinkman, M. Huijben, M. van Zalk, J. Huijben, U. Zeitler, J. C. Maan, W. G. van der Wiel, G. Rijnders, D. H. A. Blank, and H. Hilgenkamp, "Magnetic effects at the interface between non-magnetic oxides," Nature Materials **6**, 493–496 (2007).

[67] Y. Xie, C. Bell, T. Yajima, Y. Hikita, and H. Y. Hwang, "Charge writing at the $LaAlO_3/SrTiO_3$ surface," Nano Letters **10**, 2588–2591 (2010).

[68] Y. Z. Chen, J. L. Zhao, J. R. Sun, N. Pryds, and B. G. Shen, "Resistance switching at the interface of $LaAlO_3/SrTiO_3$," Applied Physics Letters **97**, 123 102–3 (2010).

[69] H. Ohta, S. Kim, Y. Mune, T. Mizoguchi, K. Nomura, S. Ohta, T. Nomura, Y. Nakanishi, Y. Ikuhara, M. Hirano, H. Hosono, and K. Koumoto, "Giant thermoelectric Seebeck coefficient of a two-dimensional electron gas in $SrTiO_3$," Nature Materials **6**, 129–134 (2007).

[70] J. García-Barriocanal, A. Rivera-Calzada, M. Varela, Z. Sefrioui, E. Iborra, C. Leon, S. J. Pennycook, and J. Santamaria, "Colossal ionic conductivity at interfaces of epitaxial ZrO_2:$Y_2O_3/SrTiO_3$ heterostructures," Science **321**, 676–680 (2008).

[71] Y. Hotta, T. Susaki, and H. Hwang, "Polar discontinuity doping of the $LaVO_3/SrTiO_3$ interface," Physical Review Letters **99**, 236 805 (2007).

[72] J. Mannhart and D. G. Schlom, "Oxide interfaces - An opportunity for electronics," Science **327**, 1607–1611 (2010).

[73] S. A. Chambers, "Epitaxial growth and properties of doped transition metal and complex oxide films," Advanced Materials **22**, 219–248 (2010).

[74] H. W. Jang, D. A. Felker, C. W. Bark, Y. Wang, M. K. Niranjan, C. T. Nelson, Y. Zhang, D. Su, C. M. Folkman, S. H. Baek, S. Lee, K. Janicka, Y. Zhu, X. Q. Pan, D. D. Fong, E. Y. Tsymbal, M. S. Rzchowski, and C. B. Eom, "Metallic and insulating oxide interfaces controlled by electronic correlations," Science **331**, 886–889 (2011).

[75] P. R. Willmott, S. A. Pauli, R. Herger, Schlep, uuml, C. M. tz, D. Martoccia, B. D. Patterson, B. Delley, R. Clarke, D. Kumah, C. Cionca, and Y. Yacoby, "Structural basis for the conducting interface between $LaAlO_3$ and $SrTiO_3$," Physical Review Letters **99**, 155 502 (2007).

[76] A. Kalabukhov, R. Gunnarsson, J. Börjesson, E. Olsson, T. Claeson, and D. Winkler, "Effect of oxygen vacancies in the $SrTiO_3$ substrate on the electrical properties of the $LaAlO_3$ / $SrTiO_3$ interface," Physical Review B **75**, 121 404 (2007).

[77] W. Siemons, G. Koster, H. Yamamoto, W. A. Harrison, G. Lucovsky, T. H. Geballe, D. H. A. Blank, and M. R. Beasley, "Origin of charge density at $LaAlO_3$ on $SrTiO_3$ heterointerfaces: possibility of intrinsic doping," Physical Review Letters **98**, 196 802 (2007).

[78] M. Huijben, G. Rijnders, D. H. A. Blank, S. Bals, S. van Aert, J. Verbeeck, G. van Tendeloo, A. Brinkman, and H. Hilgenkamp, "Electronically coupled complementary interfaces between perovskite band insulators," Nature Materials **5**, 556–560 (2006).

[79] A. Müller, Private communication.

[80] A. Kalabukhov, Y. A. Boikov, I. T. Serenkov, V. I. Sakharov, J. Börjesson, N. Ljustina, E. Olsson, D. Winkler, and T. Claeson, "Improved cationic stoichiometry and insulating behavior at the interface of $LaAlO_3/SrTiO_3$ formed at high oxygen pressure during pulsed-laser deposition," Europhysics Letters **93**, 37 001 (2011).

[81] K. A. Müller, W. Berlinger, and F. Waldner, "Characteristic structural phase transition in perosvkite-type compounds," Physical Review Letters **21**, 814–817 (1968).

[82] S. Thiel, G. Hammerl, A. Schmehl, C. W. Schneider, and J. Mannhart, "Tunable quasi-two-dimensional electron gases in oxide heterostructures," Science **313**, 1942–1945 (2006).

[83] V. E. Henrich, G. Dresselhaus, and H. J. Zeiger, "Surface defects and the electronic structure of $SrTiO_3$ surfaces," Physical Review B **17**, 4908 (1978).

[84] M. Sing, G. Berner, K. Goß, A. Müller, A. Ruff, A. Wetscherek, S. Thiel, J. Mannhart, S. A. Pauli, C. W. Schneider, P. R. Willmott, M. Gorgoi, F. Schäfers, and R. Claessen, "Profiling the interface electron gas of $LaAlO_3/SrTiO_3$ heterostructures with hard X-Ray photoelectron spectroscopy," Physical Review Letters **102**, 176 805 (2009).

[85] S. Amoruso, C. Aruta, R. Bruzzese, D. Maccariello, L. Maritato, F. Miletto Granozio, P. Orgiani, U. Scotti di Uccio, and X. Wang, "Optimization of $La_{0.7}Ba_{0.3}MnO_{3-\delta}$ complex oxide laser ablation conditions by plume imaging and optical emission spectroscopy," Journal of Applied Physics **108**, 043 302 (2010).

[86] A. Gupta, "Gas-phase oxidation chemistry during pulsed laser deposition of $YBa_2Cu_3O_{7-\delta}$ films," Journal of Applied Physics **73**, 7877–7886 (1993).

[87] K. Shibuya, T. Ohnishi, M. Lippmaa, and M. Oshima, "Metallic conductivity at the $CaHfO_3/SrTiO_3$ interface," Applied Physics Letters **91**, 232 106–3 (2007).

[88] D. W. Reagor and V. Y. Butko, "Highly conductive nanolayers on strontium titanate produced by preferential ion-beam etching," Nature Materials **4**, 593–596 (2005).

[89] D. M. Hill, H. M. Meyer, and J. H. Weaver, "Y, Ba, Cu, and Ti interface reactions with $SrTiO_3$ (100) surfaces," Journal of Applied Physics **65**, 4943–4950 (1989).

[90] Q. Fu and T. Wagner, "Interaction of nanostructured metal overlayers with oxide surfaces," Surface Science Reports **62**, 431–498 (2007).

[91] Q. Fu and W. T., "Metal-oxide interfacial reactions: Oxidation of metals on TiO_2(110) and $SrTiO_3$(100)," Journal of Physical Chemistry B **109**, 11 697–11 705 (2005).

[92] K. Shibuya, T. Ohnishi, T. Uozumi, H. Koinuma, and M. Lippmaa, "An in situ transport measurement of interfaces between $SrTiO_3$(100) surface and an amorphous wide-gap insulator," Applied Surface Science **252**, 81478150 (2005).

[93] C. T. Campbell, "Ultrathin metal films and particles on oxide surfaces: structural, electronic and chemisorptive properties," Surface Science Reports **27**, 1–111 (1997).

[94] H. B. Michaelson, "The work function of the elements and its periodicity," Journal of Applied Physics **48**, 4729–4733 (1977).

[95] C. Aruta, S. Amoruso, R. Bruzzese, X. Wang, D. Maccariello, F. Miletto Granozio, and U. Scotti di Uccio, "Pulsed laser deposition of $SrTiO_3/LaGaO_3$ and $SrTiO_3/LaAlO_3$: Plasma plume effects," Applied Physics Letters **97**, 252 105 (2010).

[96] C. W. Schneider, S. Thiel, G. Hammerl, C. Richter, and J. Mannhart, "Microlithography of electron gases formed at interfaces in oxide heterostructures," Applied Physics Letters **89**, 122 101 (2006).

[97] C. W. Schneider, M. Esposito, I. Marozau, K. Conder, M. Doebeli, Y. Hu, M. Mallepell, A. Wokaum, and T. Lippert, "The origin of oxygen in oxide thin films: Role of substrate," Applied Physics Letters **97**, 192 107 (2010).

[98] M. Basletić, J. L. Maurice, C. Carrétéro, G. Herranz, O. Copie, M. Bibes, E. Jacquet, K. Bouzehouane, S. Fusil, and A. Barthélémy, "Mapping the spatial distribution of charge carriers in $LaAlO_3/SrTiO_3$ heterostructures," Nature Materials **7**, 621–625 (2008).

[99] T. Fix, F. Schoofs, J. L. MacManus-Driscoll, and M. G. Blamire, "Charge confinement and doping at $LaAlO_3/SrTiO_3$ interfaces," Physical Review Letters **103**, 166 802 (2009).

[100] G. Herranz, M. Basletić, M. Bibes, C. Carrétéro, E. Tafra, E. Jacquet, K. Bouzehouane, C. Deranlot, A. Hamzić, J. M. Broto, A. Barthélémy, and A. Fert, "High mobility in $LaAlO_3/SrTiO_3$ heterostructures: origin, dimensionality, and perspectives," Physical Review Letters **98**, 216 803 (2007).

[101] N. Reyren, S. Thiel, A. D. Caviglia, L. F. Kourkoutis, G. Hammerl, C. Richter, C. W. Schneider, T. Kopp, A.-S. Ruetschi, D. Jaccard, M. Gabay, D. A. Muller, J.-M. Triscone, and J. Mannhart, "Superconducting interfaces between insulating oxides," Science **317**, 1196–1199 (2007).

[102] H. Boschker, *Perovskite oxide heteroepitxay: strain and interface engineering*, Ph.D. thesis, University of Twente (2011).

[103] M. Takizawa, S. Tsuda, T. Susaki, H. Y. Hwang, and A. Fujimori, "Electronic charges and electric potential at $LaAlO_3/SrTiO_3$ interfaces studied by core-level photoemission spectroscopy," Physical Review B **84**, 245 124 (2011).

[104] P. R. Willmott, S. A. Pauli, R. Herger, C. M. Schlepuetz, D. Martoccia, B. D. Patterson, B. Delley, R. Clarke, D. Kumah, C. Cionca, and Y. Yacoby, "Structural basis for the conducting interface between $LaAlO_3$ and $SrTiO_3$," Physical Review Letters **99**, 155 502 (2007).

[105] S. A. Pauli, S. J. Leake, B. Delley, M. Bjrck, C. W. Schneider, C. M. Schlepütz, D. Martoccia, S. Paetel, J. Mannhart, and P. R. Willmott, "Evolution of the interfacial structure of $LaAlO_3$ on $SrTiO_3$," Physical Review Letters **106**, 036 101 (2011).

[106] H. Boschker, A. Brinkman, A. Müller, J. E. Kleibeuker, G. Hassink, M. Sing, R. Claessen, M. Huijben, G. Koster, D. H. A. Blank, and G. Rijnders, "Modelling conductivity at the $LaAlO_3/SrTiO_3$ interface based on the induced polarization in $SrTiO_3$," (2011), submitted.

[107] J. L. Maurice, C. Carrétéro, M. J. Casanove, K. Bouzehouane, S. Guyard, E. Larquet, and J. P. Contour, "Electronic conductivity and structural distortion at the interface between insulators $SrTiO_3$ and $LaAlO_3$," Physica Status Solidi A - Applications and Material Science **203**, 2209–2214 (2006).

[108] V. Vonk, M. Huijben, K. J. I. Driessen, P. Tinnemans, A. Brinkman, S. Harkema, and H. Graafsma, "Interface structure of $SrTiO_3/LaAlO_3$ at elevated temperatures studied in situ by synchrotron x-rays," Physical Review B **75**, 235 417 (2007).

[109] A. Savoia, D. Paparo, P. Perna, Z. Ristic, M. Salluzzo, F. M. Granozio, U. S. di Uccio, C. Richter, S. Thiel, J. Mannhart, and L. Marrucci, "Polar catastrophe and electronic reconstructions at the $LaAlO_3/SrTiO_3$ interface: Evidence from optical second harmonic generation," Physical Review B **80**, 075 110 (2009).

[110] R. Pentcheva, M. Huijben, K. Otte, W. E. Pickett, J. E. Kleibeuker, J. Huijben, H. Boschker, D. Kockmann, W. Siemons, G. Koster, H. J. W. Zandvliet, G. Rijnders, D. H. A. Blank, H. Hilgenkamp, and A. Brinkman, "Parallel electron-hole bilayer conductivity from electronic interface reconstruction," Physical Review Letters **104**, 166 804 (2010).

[111] M. Huijben, G. Koster, H. J. A. Molegraaf, M. K. Kruize, S. Wenderich, J. E. Kleibeuker, A. McCollam, V. K. Guduru, A. Brinkman, H. Hilgenkamp, U. Zeitler, J. C. Maan, D. H. A. Blank, and G. Rijnders, "High mobility interface electron gas by defect scavenging in a modulation doped oxide heterostructure," arXiv 1008.1896 (2010).

[112] H. Unoki and T. Sakudo, "Electron spin resonance of Fe^{3+} in $SrTiO_3$ with special reference to the 110°K phase transition," Journal of the Physical society of Japan **23**, 546–552 (1967).

[113] G. W. Berkstresser, A. J. Valentino, and C. D. Brandle, "Growth of single crystals of lanthanum aluminate," Journal of Crystal Growth **109**, 457–466 (1991).

[114] B. C. Chakoumakos, D. G. Schlom, M. Urbanik, and J. Luine, "Thermal expansion of $LaAlO_3$ and $(La,Sr)(Al,Ta)O_3$, substrate materials for superconducting thin-film device applications," Physical Review B **79**, 081 405 (2009).

[115] S. Geller, "Crystallographic studies of perovskite-like compounds. IV. Rare earth scandates, vanadites, galliates, orthochromites," Acta Crystallographica **10**, 243–248 (1957).

[116] J. M. Rondinelli and N. A. Spaldin, "Structure and properties of functional oxide thin films: Insights from electronic-structure calculations," Advanced Materials **23**, 33633381 (2011).

[117] V. Leca, *Heteroepitaxial growth of copper oxide superconductors by pulsed laser deposition*, Ph.D. thesis, University of Twente (2003).

[118] P. Brinks, W. Siemons, J. E. Kleibeuker, G. Koster, G. Rijnders, and M. Huijben, "Anisotropic electrical transport properties of a two-dimensional electron gas at $SrTiO_3$ $LaAlO_3$ interfaces," Applied Physics Letters **98**, 242 904 (2011).

[119] T. Ohnishi, K. Takahashi, M. Nakamura, M. Kawasaki, M. Yoshimoto, and H. Koinuma, "A-site layer terminated perovskite substrate: $NdGaO_3$," Applied Physics Letters **74**, 2531–2533 (1999).

[120] B. Jalan, R. Engel-Herbert, N. J. Wright, and S. Stemmer, "Growth of high-quality $SrTiO_3$ films using hybrid molecular beam epitaxy approach," Journal of Vacuum Science and Technology A **27**, 461–464 (2009).

[121] J. M. LeBeau, R. Engel-Herbert, B. Jalan, J. Cagnon, P. Moetakef, S. Stemmer, and G. B. Stephenson, "Stoichiometry optimization of homoepitaxial oxide thin films using x-ray diffraction," Applied Physics Letters **95**, 142 905 (2009).

[122] B. Jalan, P. Moetakef, and S. Stemmer, "Molecular beam epitaxy of $SrTiO_3$ with a growth window," Applied Physics Letters **95**, 032 906 (2009).

[123] A. J. H. M. Rijnders, *The initial growth of complex oxides: study and manipulation*, Ph.D. thesis, University of Twente (2001).

[124] L. van Rees, *Electronic effects at interfaces between complex oxides*, Master's thesis, University of Twente (2008).

[125] D.-W. Oh, J. Ravichandran, C.-W. Liang, W. Siemons, B. Jalan, C. M. Brooks, M. Huijben, D. G. Schlom, S. Stemmer, L. W. Martin, A. Majumdar, R. Ramesh, and D. G. Cahill, "Thermal conductivity as a metric for the crystalline quality of $SrTiO_3$ epitaxial layers," Applied Physics Letters **98**, 221 904 (2011).

[126] J. Ravichandran, W. Siemons, H. Heijmerikx, M. Huijben, A. Majumdar, and R. Ramesh, "An epitaxial transparent conducting perovskite oxide: double-doped $SrTiO_3$," Chemistry of Materials **22**, 39833987 (2010).

[127] K. Szot, W. Speier, J. Herion, and C. Freiburg, "Restructuring of the surface region in $SrTiO_3$," Applied Physics A **64**, 55–59 (1997).

[128] Y. Kozuka, Y. Hikita, C. Bell, and H. Y. Hwang, "Dramatic mobility enhancements in doped $SrTiO_3$ thin films by defect management," Applied Physics Letters **97**, 012 107 (2010).

[129] A. Müller, H. Boschker, F. Pfaff, G. Berner, S. Thiess, W. Drube, G. Koster, G. Rijnders, D. H. A. Blank, M. Sing, and R. Claessen, "Growth pressure control of electronic interface properties in $LaAlO_3/SrTiO_3$ heterostructures: new insights from high-energy spectroscopy," To be publsihed.

[130] S. A. Chambers, M. H. Engelhard, V. Shutthanandan, Z. Zhu, T. C. Droubay, L. Qiao, P. V. Sushko, T. Feng, H. D. Lee, T. Gustafsson, E. Garfunkel, A. B. Shah, J. M. Zuo, and Q. M. Ramasse, "Instability, intermixing and electronic structure at the epitaxial $LaAlO_3/SrTiO_3$ heterojunction," Surface Science Reports **65**, 317–352 (2010).

[131] M. Warusawithana, J. Ludwig, P. Roy, A. A. Pawlicki, T. Heeg, D. Schlom, C. Richter, S. Paetel, J. Mannhart, L. Fitting Kourkoutis, J. Mundy, D. A. Muller, M. Zheng, B. Mulcahy, J. N. Eckstein, W. Zander, and J. Schubert, "Effect of stoichiometry on the interface conductivity of MBE-grown $LaAlO_3/SrTiO_3$ heterostructures," http://meetings.aps.org/link/BAPS.2011.MAR.A34.4 (2011).

[132] S. A. Chambers, "Understanding the mechanism of conductivity at the $LaAlO_3/SrTiO_3$(001) interface," Surface Science **605**, 1133–1140 (2011).

[133] I. M. Dildar, D. B. Boltje, M. H. S. Hesselberth, Q. Xu, H. W. Zandbergen, and S. Harkema, "Conductivity of $LaAlO_3/SrTiO_3$ interfaces made by sputter deposition," arXiv 1111.5047v1 (2011).

[134] C. M. Brooks, L. Fitting Kourkoutis, T. Heeg, J. Schubert, D. A. Muller, and D. G. Schlom, "Growth of homoepitaxial $SrTiO_3$ thin films by molecular-beam epitaxy," Applied Physics Letters **94**, 162 905 (2009).

[135] F. Gunkel, S. Hoffmann-Eifert, R. Dittmann, S. B. Mi, C. L. Jia, P. Meuffels, and R. Waser, "High temperature conductance characteristics of $LaAlO_3/SrTiO_3$-heterostructures under equilibrium oxygen atmospheres," Applied Physics Letters **97**, 012 103 (2010).

[136] T. Bieger, J. Maier, and R. Waser, "Kinetics of oxygen incorporation in $SrTiO_3$ (Fe-doped): an optical investigation," Sensors and Actuators B: Chemical **7**, 763–768 (1992).

[137] I. Denk, W. Mnch, and J. Maier, "Partial conductivities in $SrTiO_3$: Bulk polarization experiments, oxygen concentration cell measurements, and defect-chemical modeling," Journal of the American Ceramic Society **78**, 3265–3272 (1995).

[138] W. Gong, H. Yun, Y. B. Ning, J. E. Greedan, W. R. Datars, and C. V. Stager, "Oxygen-deficient $SrTiO_{3-x}$, x = 0.28, 0.17, and 0.08. Crystal growth, crystal structure, magnetic, and transport properties," Journal of Solid State Chemistry **90**, 320–330 (1991).

[139] D. M. Smyth, *The defect chemistry of metal oxides* (Oxford University Press, New York, 2000).

[140] F. Gunkel, P. Brinks, S. Hoffmann-Eifert, R. Dittmann, M. Huijben, J. E. Kleibeuker, G. Koster, G. Rijnders, and R. Waser, "Influence of charge compensation mechanisms on the sheet electron density at conducting $LaAlO_3/SrTiO_3$-interfaces," Applied Physics Letters **100**, 052 103 (2012).

[141] A. J. Hatt and N. A. Spaldin, "Structural phases of strained $LaAlO_3$ driven by octahedral tilt instabilities," Physical Review B **82**, 195 402 (2010).

[142] C. W. Bark, D. A. Felker, Y. Wang, Y. Zhang, H. W. Jang, C. M. Folkman, J. W. Park, S. H. Baek, H. Zhouf, D. D. Fong, X. Q. Pan, E. Y. Tsymbal, M. S. Rzchowski, and C. B. Eom, "Tailoring a two-dimensional electron gas at the $LaAlO_3/SrTiO_3$ (001) interface by epitaxial strain," Proceedings of the National Academy of Sciences of the United States of America **108**, 4720–4724 (2011).

[143] J. Nishimura, A. Ohtomo, A. Ohkubo, Y. Murakami, and M. Kawasaki, "Controlled carrier generation at a polarity-discontinued perovskite heterointerface," Japanese Journal of Applied Physics **43**, L1032 (2004).

[144] C. W. Bark, Private communication (2010).

[145] D. D. Sarma, N. Shanthi, S. R. Barman, N. Hamada, H. Sawada, and K. Terakura, "Band theory for ground-state properties and excitation spectra of perovskite $LaMO_3$ (M = Mn, Fe, Co, Ni)," Physical Review Letters **75**, 11261129 (1995).

[146] R. Spinicci, A. Tofanari, M. Faticanti, I. Pettiti, and P. Porta, "Hexane total oxidation on LaMO_3 (M = Mn, Co, Fe) perovskite-type oxides," Journal of Molecular Catalysis A: Chemical **176**, 247–252 (2001).

[147] M. Imada, A. Fujimori, and Y. Tokura, "Metal-insulator transitions," Reviews of Modern Physics **70**, 1039–1263 (1998).

[148] T. Arima, Y. Tokura, and J. B. Torrance, "Variation of optical gaps in perovskite-type $3d$ transition-metal oxides," Physical Review Letters **48**, 17 006–17 009 (1993).

[149] J. Zaanen, G. A. Sawatzky, and J. W. Allen, "Band gaps and electronic structure of transition metal compounds," Physical Review Letters **55**, 418–421 (1985).

[150] J. B. Torrance, P. Lacorre, C. Asavaroengchai, and R. M. Metzger, "Why are some oxides metallic, while most are insulating?" Physica C **182**, 351–364 (1991).

[151] A. Y. Borisevich, H. J. Chang, M. Huijben, M. P. Oxley, S. Okamoto, M. K. Niranjan, J. D. Burton, E. Y. Tsymbal, Y. H. Chu, P. Yu, R. Ramesh, S. V. Kalinin, and S. J. Pennycook, "Suppression of octahedral tilts and associated changes in electronic properties at epitaxial oxide heterostructure interfaces," Physical Review Letters **105**, 087 204 (2010).

[152] M. Cwik, T. Lorenz, J. Baier, R. Müller, G. André, F. Bourée, F. Lichtenberg, A. Freimuth, R. Schmitz, E. Müller-Hartmann, and M. Braden, "Crystal and magnetic structure of $LaTiO_3$: Evidence for nondegenerate t_{2g} orbitals," Physical Review B **68**, 060 401(R) (2003).

[153] D. B. Rogers, A. Ferretti, D. H. Ridgley, R. J. Arnott, and J. B. Goodenough, "Single-Crystal growth and properties of the perovskites $LaVO_3$ and YVO_3," Journal of Applied Physics **37**, 1431 – 1432 (1996).

[154] W. C. Koehler and E. O. Wollan, "Neutron-diffraction study of the magnetic properties of perovskite-like compounds $LaBO_3$," Journal of Physics and Chemistry of Solids **2**, 100–106 (1957).

[155] J. F. Bringley, B. A. Scott, S. J. La Placa, T. R. McGuire, F. Mehran, M. W. McElfresh, and D. E. Cox, "Structure and properties of the $LaCuO_{3-d}$ perovskites," Physical Review B **47**, 15 26915 275 (1993).

[156] W. C. Koehler, E. O. Wollan, and M. K. Wilkinson, "Neutron diffraction study of the magnetic properties of rare-earth-iron perovskites," Physical Review **118**, 58–70 (1960).

[157] K. Ueda, H. Tabata, and T. Kawai, "Atomic arrangement and magnetic properties of $LaFeO_3$-$LaMnO_3$ artificial superlattices," Physical Review B **60**, 561–564 (1999).

[158] J.-C. Grenier, N. Ea, M. Pouchard, and M. Abou-Sekkina, "Properties electriques et magnetiques des ferrites oxydes $La_{1-x}Sr_xFeO_{3-y}$," Materials Research Bulletin **19**, 1301–1309 (1984).

[159] M. Descostes, F. Mercier, N. Thromat, C. Beaucaire, and M. Gautier-Soyer, "Use of XPS in the determination of chemical environment and oxidation state of iron and sulfur samples: constitution of a data basis in binding energies for Fe and S reference compounds and applications to the evidence of surface species of an oxidized pyrite in a carbonate medium," Applied Surface Science **165**, 288–302 (2000).

[160] A. Ohtomo, D. A. Muller, J. L. Grazul, and H. Y. Hwang, "Epitaxial growth and electronic structure of $LaTiO_x$ films," Applied Physics Letters **80**, 3922–3924 (2002).

[161] C. ollaboration authors and editors of the volumes III/17H-17I-41E, *$LaFeO_3$ crystal structure, physical properties*. O. Madelung, U. Rössler, M. Schulz (ed) (SpringerMaterials).

[162] V. V. Atuchin, V. G. Kesler, N. V. Pervukhina, and Z. Zhang, "Ti 2p and O 1s core levels and chemical bonding in titanium-bearing oxides," Journal of Electron Spectroscopy **152**, 18–24 (2006).

[163] G. W. J. Hassink, *Tow-dimensional electron layers in perovskite oxides*, Ph.D. thesis, University of Twente (2009).

[164] H. Boschker, Private communication.

[165] T. Fujii, F. M. F. d. Groot, G. A. Sawatzky, F. C. Voogt, T. Hibma, and K. Okada, "*In situ* XPS analysis of various iron oxide films grown by NO_2-assisted molecular-beam epitaxy," Physical Review B **59**, 3195–3202 (1999).

[166] R. P. Gupta and S. K. Sen, "Calculation of multiplet structure of core *p*-vacancy levels. II," Physical Review B **12**, 15–19 (1975).

[167] T. H. Fleisch and G. J. Mains, "Reduction of copper oxides by UV radiation and atomic hydrogen studied by XPS," Applications of Surface Science **10**, 51–62 (1982).

[168] S. Poulston, P. M. Parlett, P. Stone, and M. Bowker, "Surface oxidation and reduction of CuO and Cu_2O studied using XPS and XAES," Surface and Interface Analysis **24**, 811–820 (1996).

[169] Y. Iijima, N. Niimura, and K. Hiraoka, "Prevention of the Reduction of CuO during X-ray Photoelectron Spectroscopy Analysis," Surface and Interface Analysis **24**, 193–197 (1996).

[170] T. H. Fleisch and G. J. Mains, "An XPS study on the UV reduction and photochromism of MoO_3 and WO_3," Journal of Chemical Physics **76**, 780–786 (1982).

[171] A. P. Grosvenor, B. A. Kobe, M. C. Biesinger, and N. S. McIntyre, "Investigation of multiplet splitting of Fe 2p XPS spectra and bonding in iron compounds," Surface and Interface Analysis **36**, 1564–1574 (2004).

[172] M. Khalid, A. Setzer, M. Ziese, P. Esquinazi, D. Spemann, A. Pöppl, and E. Goering, "Ubiquity of ferromagnetic signals in common diamagnetic oxide crystals," Physical Review B **81**, 214 414 (2010).

[173] M. Huijben, L. W. Martin, Y.-H. Chu, M. B. Holcomb, P. Yu, G. Rijnders, D. H. A. Blank, and R. Ramesh, "Critical thickness and orbital ordering in ultrathin $La_{0.7}Sr_{0.3}MnO_3$ films," Physical Review B **78**, 094 413 (2008).

[174] Y. Okada, T. Arima, Y. Tokura, C. Murayama, and N. Môri, "Doping- and pressure-induced change of the electrical and magnetic properties in the Mott-Hubbard insulator $LaTiO_3$," Physical Review B **48**, 9677–9683 (1993).

[175] P. Brinks, H. Heijmerikx, T. A. Hendriks, G. Rijnders, and M. Huijben, "Chemical stability and thermoelectric properties of Na_xCoO_2," (2012), submitted.

[176] J. J. Neumeier and H. Terashita, "Magnetic, thermal, and electrical properties of $La_{1-x}Ca_xCrO_3$ ($0 \leq x \leq 0.5$)," Physical Review B **70**, 214 435 (2004).

Summary

Perovskite-type oxides, ABO_3, are of high interest since they exhibit a wide variety of properties. Having comparable oxygen backbone structures, perovskite-type oxides can easily be stacked on top of each other with atomic precision. This may result in advanced materials with new or enhanced functionalities. Moreover, near the interface, interplay between the different materials occurs, which may lead to interesting functionalities confined at the interface. For the devolpment of device applications, it is important to understand the origin of the functionalities near the interface of oxide heterostructures. In this thesis, the interface behavior of perovskite-type oxide heterostructures was studied for four different cases. Electronic, structural and chemical reconstructions were taken into account.

The first topic concerned the interface between a perovskite-type oxide crystal surface and vacuum. A chemical surface treatment for $REScO_3$ (110) single crystals is developed to achieve single terminated crystal surfaces, which are important for studies on heteroepitaxial interfaces. Here, ScO_2 terminated surfaces were achieved after selective wet etching, as shown by angle resolved mass spectroscopy of recoiled ions (AR-MSRI). Furthermore, a study on $SrRuO_3$ growth and nucleation was introduced to determine whether the $REScO_3$ surface was perfect singly terminated, since $SrRuO_3$ is sensitive to differences in surface diffusivity. Complete single termination has been proven for $DyScO_3$ (110). The $REScO_3$ (110) atomic planes (REO^+ and ScO_2^-) are polar. Therefore, perfect singly terminated $REScO_3$ surfaces were expected to be energetically unfavorable and surface reconstructions were suggested to occur. Surface reconstructions of ScO_2 terminated $DyScO_3$ (110) were determined by reflection high energy electron diffraction (RHEED), surface X-ray diffraction (SXRD) and AR-MSRI. No indications for ordered cation displacements as well as ordered cation vacancies were observed. Therefore, it was suggested that oxygen vacancies were most likely to occur to overcome the polarity difference between bulk $DyScO_3$ and vacuum.

The next part focused on the chemical driving forces between complex oxides. Heterostructures of an amorphous oxide on crystalline $SrTiO_3$ substrates have been taken as a model system. It has been shown that redox reactions may occur at the interface during growth, resulting in oxygen diffusion from the $SrTiO_3$ single crystal to the amorphous film. As a result, oxygen vacancies are created in the $SrTiO_3$ near the interface and the interface may become conducting. A minimum film thickness was necessary to achieve conductivity. The critical thickness

depended on the film material and oxygen growth pressure.

The third case is based on the interface between two crystalline wide band gap insulators, $LaAlO_3$ and $SrTiO_3$. An important difference between the two materials is the total charge of the atomic planes. $SrTiO_3$ consists of charge neutral atomic planes (SrO and TiO_2), while $LaAlO_3$ consists of alternating positively and negatively charged planes (LaO^+ and AlO_2^-). As a result, a polar discontinuity is present at a perfect $LaAlO_3$-$SrTiO_3$ interface. Depending on the atomic interface stacking, the interface can become metallic. In previous studies, several models were proposed to clarify the properties of the $LaAlO_3$-$SrTiO_3$ interface. These models were based on intrinsic electronic reconstruction, intermixing, oxygen vacancies or polarization discontinuity, but none of these models are conclusive. Up to now, studies on $LaAlO_3$-$SrTiO_3$ interfaces were mainly focused on the $LaAlO_3$ layer and the $LaAlO_3$ surface. Since the conducting layer is in the $SrTiO_3$ near the interface, the $SrTiO_3$ template is expected to have a significant influence on the interface behavior. Understanding of this influence is expected to give information on the origin of the metallic behavior near the interface. In chapter 4, the influence of the $SrTiO_3$ template on $LaAlO_3$-$SrTiO_3$ interfaces has been investigated. The $SrTiO_3$ template has been modified by applying strain and octahedral rotations using various oxide substrates and by varying the defect density using various deposition techniques. The $LaAlO_3$-$SrTiO_3$ interfaces remained insulating on $NdGaO_3$ and $DyScO_3$ substrates, while the interface became conducting on $(LaSr)(AlTa)O_3$. Moreover, the introduction of a $SrTiO_3$ film grown by pulsed laser deposition (PLD) or hybrid molecular beam epitaxy (H-MBE) between $LaAlO_3$ film and $SrTiO_3$ (001) substrate resulted in insulating heterostructures. Scanning transmission electron microscopy (STEM) and X-ray photoelectron spectroscopy (XPS) measurements implied that the oxygen content in $SrTiO_3$ films is increased compared to $SrTiO_3$ substates. On the other hand, similar cation intermixing was observed by STEM at the interface of artificially grown and standard $LaAlO_3$-$SrTiO_3$. Based on the results shown in this chapter, it has been suggested that both octahedral rotations and oxygen vacancies are important for achieving conducting interfaces.

The final topic focusses on the interface between two iso-polar insulating materials, $LaFeO_3$ and $LaTiO_3$. Both materials are insulators, but their charge gaps are defined differently. $LaTiO_3$ is a Mott-Hubbard insulator; its charge gap is determined by the splitting of its Hubbard subbands (d-d gap). $LaFeO_3$ is a charge-transfer insulator; its charge gap is determined by the oxygen p band and the empty upper Hubbard band. In $LaFeO_3$-$LaTiO_3$ heterostructures, it is proposed that their oxygen p bands align near the interface since they share their oxygen octahedra at the interface. As a result, the empty upper Hubbard band of $LaFeO_3$ is pulled below the energy level of the partially filled lower Hubbard band of $LaTiO_3$. This would result in electron transfer from $LaTiO_3$ to $LaFeO_3$. Electron doped $LaFeO_3$ has been observed by XPS in $LaFeO_3$-$LaTiO_3$ heterostructures, while it was absent in $LaFeO_3$ and $LaFeO_3$-$LaAlO_3$. Moreover, the valence band spectra of $LaFeO_3$-$LaTiO_3$ indicate that the extra electrons on the Fe site originated from the lower Hubbard Ti $3d$ band. This is consistent with the charge

transfer hypothesis. Charge modulation of $LaTiO_3$ and $LaFeO_3$ was expected to result in variations of the magnetic and electronic properties. However, no clear changes have been observed so far.

The four different topics discussed the manipulation of perovskite-type oxide interfaces at an atomic scale using different methods, chemically as well as physically. As a result, variations in composition, structure and charge were achieved near the interface leading to differences in the interfacial behavior. It has been shown that the behavior of perovskite-type oxide interfaces is very sensitive to small variations near the interface. For follow-up studies, it is valuable to focus on the oxygen in oxide heterostructures. The structure of the oxygen octahedra and the oxygen stoichiometry influence the behavior of the oxide materials significantly. Moreover, oxygen band alignment near the oxide interface may be utilized in other material systems than described in this thesis to induce variations in their physical behavior.

Samenvatting

Vanwege de grote variëteit aan eigenschappen is er veel interesse in perovskiet-type oxides (ABO_3). Deze oxiden hebben allemaal een vergelijkbare zuurstofstructuur en kunnen daarom gestapeld worden met atomaire precisie. Hierdoor zijn deze materialen zeer geschikt voor het bestuderen van oxidische heterostructuren. In deze kunstmatige heterostructuren is het mogelijk om nieuwe of verbeterde functionaliteiten te verkrijgen. Daarnaast is het mogelijk om functionaliteiten specifiek aan het grensvlak te creëeren door gebruik te maken van de interactie tussen de verschillende materialen. Om de kunstmatige heterostructuren te kunnen toepassen is het van belang om de oorsprong van deze nieuwe functionaliteiten te begrijpen. In dit proefschrift worden de eigenschappen van het grensvlak voor vier verschillende perovskiet-type oxidische heterostructuren bestudeerd. Zowel elektronsiche, structurele als chemische reconstructies zijn in acht genomen.

Allereerst wordt het grensvlak tussen een perovskiet-type oxide oppervlak en vacuum besproken. Oppervlaktes met slechts één type kation aan het oppervlak, oftewel enkel getermineerde oppervlaktes, zijn essentieel voor het bestuderen van heteroepitaxiale structuren. In hoofdstuk 2 wordt een chemische oppervlakte behandeling voor zeldzame aarde scandaten, $REScO_3$ (110), gepresenteerd. Gebruikmakend van het verschil in chemische reactiviteit tussen REO and ScO_2 vlakken, kon het oppervlak selectief geetst worden. Middels hoek afhankelijke massaspectroscopie van teruggestoten ionen (AR-MSRI) is bepaald dat voornamelijk Sc aanwezig was aan het oppervlak na behandeling. De enorme gevoeligheid van $SrRuO_3$ dunne laag groei voor verschillende kation terminaties is gebruikt om aan te tonen dat het oppervlak geheel ScO_2 getermineerd was. De atomaire vlakken van $REScO_3$ (110) (REO^+ en ScO_2^-) zijn polair. Het wordt aangenomen dat enkelvoudig getermineerde $REScO_3$ oppervlaktes energetisch ongunstig zijn. Daarom wordt geopperd dat oppervlakte reconstructies plaats vinden. Met behulp van reflectieve hoge energie elektronen diffractie (RHEED), oppervlaktegevoelige Röntgendiffractie (SXRD) en AR-MSRI zijn mogelijke reconstructies aan $DyScO_3$ (110) oppervlaktes onderzocht. Deze metingen gaven geen indicatie voor geordende kation verplaatsingen en geordende kation vacatures. Daarom is voorgesteld dat zuurstof vacatures aan een ScO_2 getermineerd oppervlak aanwezig zijn om de polaire discontinuiteit tussen vacuüm en bulk op te heffen.

Het volgende onderdeel focust op de chemische interacties tussen verschillende complexe oxides. Hiervoor waren heterostructuren van amorfe oxides op kris-

tallijne $SrTiO_3$ substraten genomen als modelsysteem. Het is aangetoond dat gedurende de groei redox reacties plaats kunnen vinden aan het grensvlak. Zuurstof diffundeert uit het $SrTiO_3$ substraat naar de amorfe laag. Hierdoor worden zuursof vacatures gevormd in het $SrTiO_3$ nabij het grensvlak. Hierdoor kan het grensvlak geleidend worden. Voor deze heterostructuren is een minimum dikte van de amorfe laag noodzakelijk om geleiding te verkrijgen. De minimum dikte hangt af van de compositie van het amorfe materiaal en de zuurstofdruk tijdens de fabricatie.

Het onderzoek gepresenteerd in hoofdstuk 4 is gebaseerd op het grensvlak tussen twee verschillende kristallijne isolerende oxides, $LaAlO_3$ en $SrTiO_3$. Een belangrijk verschil tussen deze twee materialen is de totale lading van hun afzonderlijke atomaire vlakken. $SrTiO_3$ bestaat uit ladings neutrale vlakken (SrO en TiO_2) en $LaAlO_3$ uit alternerende positief en negatief geladen atomaire vlakken (LaO^+ en ScO_2^-). Hierdoor is aan een niet-gereconstrueerd grensvlak een polaire discontinuïteit aanwezig. De eigenschappen van het grensvlak worden sterk bepaald door de atomaire stapeling aan het grensvlak, van isolerend (SrO-AlO_2) tot metallisch (TiO_2-LaO). Verscheidene modellen zijn in voorafgaande onderzoeken geopperd om de eigenschappen van deze grensvlakken te verklaren. Deze modellen waren gebaseerd op intrinsieke elektronische reconstructie, uitwisseling van kationen, zuurstof vacatures en polarizatie discontinuïteit. Echter geen van de modellen is afdoende. In veel $LaAlO_3$-$SrTiO_3$ studies lag de focus voornamelijk op de invloed van de $LaAlO_3$ laag en het $LaAlO_3$ oppervlak op de eigenschappen van het grensvlak. Daarentegen zit de geleidende laag juist in $SrTiO_3$. Daarom wordt verwacht dat ook de $SrTiO_3$ laag nabij het grensvlak een significante invloed heeft op de eigenschappen van het grensvlak. Door de invloed van $SrTiO_3$ te bestuderen wordt er inzicht in $LaAlO_3$-$SrTiO_3$ grensvlakken verkregen. In hoofdstuk 4 wordt de invloed van $SrTiO_3$ bediscusieerd. Door dunne lagen van $SrTiO_3$ te groeien op andere oxidische substraten kon de structuur van de $SrTiO_3$ eenheidscel worden veranderd en zuurstof octahedra rotaties worden geïntroduceerd. Daarnaast is de defect dichtheid van het $SrTiO_3$ gevarieerd door verschillende groei technieken te gebruiken voor $SrTiO_3$. De $LaAlO_3$-$SrTiO_3$ grensvlakken bleven isolerend wanneer ze waren gecreëerd op $NdGaO_3$ en $DyScO_3$ substraten. Daarentegen werden ze geleidend op (LaAl)(SrTa)O_3 substraten. Door een gegroeide $SrTiO_3$ laag aan te brengen tussen $LaAlO_3$ en een $SrTiO_3$ substraat door middel van gepulseerde laserdepositie (PLD) of hybride moleculaire straal epitaxy (H-MBE) werd geleiding aan het $LaAlO_3$-$SrTiO_3$ grensvlak tegen gegaan. Resultaten verkregen met scanning transmissie elektronenmicroscopie (STEM) en Röntgen foto-elektronenspectroscopie (XPS) suggereren een toename aan zuurstof in gegroeide $SrTiO_3$ lagen ten opzichte van $SrTiO_3$ kristallen. De kation uitwisseling aan kunstmatig gegroeide en standaard $LaAlO_3$-$SrTiO_3$ grensvlakken was vergelijkbaar. In dit hoofdstuk wordt geopperd dat zowel specifieke zuurstof octahedra rotaties als zuurstof vacatures van groot belang zijn voor het verkrijgen van geleidende $LaAlO_3$-$SrTiO_3$ grensvlakken.

De laatste casus behandelt het grensvlak tussen twee isopolaire materialen, $LaFeO_3$ en $LaTiO_3$. Beide materialen zijn isolerend, maar hebben een verschil-

lende bandenstructuur rond het Fermi niveau. $LaTiO_3$ is een Mott-Hubbard isolator: de bandkloof wordt bepaald door de gevulde d band en de lege d band van Ti. $LaFeO_3$ is een *charge-transfer* isolator; de bandkloof wordt bepaald door de volle p band van zuurstof en de lege d band van Fe. Hier wordt de hypothese gesteld dat de zuurstof p banden van $LaTiO_3$ en $LaFeO_3$ op gelijk niveau komen aan een $LaTiO_3$-$LaFeO_3$ grensvlak aangezien de zuurstof octahedra gedeeld worden. Bijgevolg komt de lege d band van Fe onder het energie niveau van de gevulde d band van Ti. Hierdoor kan elektronen overdracht van $LaTiO_3$ naar $LaFeO_3$ plaatsvinden. Elektron gedoteerd $LaFeO_3$ is waargenomen in $LaTiO_3$-$LaFeO_3$ heterostructuren met behulp van XPS. Daarentegen was gedoteerd $LaFeO_3$ afwezig in bulk $LaFeO_3$ en $LaFeO_3$-$LaAlO_3$ heterostructuren. De valentieband spectra van $LaFeO_3$-$LaTiO_3$ heterostructuren wijzen erop dat de extra elektronen op de Fe positie oorspronkelijk uit de gevulde Ti $3d$ band komen. Deze observaties zijn consistent met de voorgestelde ladingsoverdracht. Als gevolg van ladingsoverdracht wordt ook een verandering in magnetische en elektronische eigenschappen verwacht. Echter, geen duidelijke veranderingen in eigenschappen zijn tot nu toe waargenomen.

De vier verschillende onderwerpen bediscussiëren het begrijpen en manipuleren van perovskiet-type oxide grensvlakken op atomaire schaal door middel van verschillende methodes, zowel chemisch als fysisch. Variatie in compositie, structuur en lading in nabijheid van het grensvlak zorgden voor veranderingen in gedrag aan het grensvlak. In alle gevallen speelde zuurstof een belangrijke rol. De eigenschappen van een grensvlak zijn zeer gevoelig voor kleine veranderingen in de zuurstof structuur en concentratie. In vervolg studies is het van belang om meer aandacht aan de zuurstofhuishouding te geven. Hierbij moet men rekening houden met octahedra rotaties, stoichiometrie, maar ook band groepering zoals in hoofdstuk 5 is beschreven. Door deze zaken gecontroleerd te manipuleren, kunnen de eigenschappen in oxidische heterostructuren systematisch geregeld worden.

Dankwoord

Dit boekje zou er nooit zijn gekomen zonder de hulp en steun van anderen gedurende de afgelopen vier jaar. Ik heb genoten van de vele samenwerkingen in binnen- en buitenland. Bij deze wil ik van de gelegenheid gebruik maken om hen te bedanken.

Om te beginnen wil ik mijn begeleiders bedanken. Guus, vanaf dag één gaf je mij het vertrouwen en liet je me vrij om mijn eigen onderzoek uit te voeren. Ondertussen zorgde je er voor dat ik de grote lijn niet uit het oog verloor. Dave, jouw enthousiasme voor onderzoek is op een positieve manier erg aanstekelijk en ontzettend motiverend. Gertjan, je vele bezoeken aan het lab waren zeer stimulerend. Hierdoor konden we meteen de meest recente resultaten bespreken. Dank voor deze zeer motiverende werkomgeving.

De afgelopen vier jaar heb ik met veel mensen samengewerkt. Veel van de resultaten zouden er niet zijn zonder deze samenwerkingen. Een goede start van het onderzoek in hoofdstuk 2 begon met het bachelor onderzoek van David, en werd vervolgd in samenwerking met Bouwe. The collaborations on SXRD (Paul, Sybolt en Elias) and AR-MSRI (Pim, Wolter, Jayakanth and Chan-Ho) were very valuable for the understanding and improvement of the surface treatment. Thanks! For chapter 3, I really enjoyed the collaboration with Yunzhong and Nini on the amorphous oxide-$SrTiO_3$ interfaces. Moreover, I want to thank the people from the EMAT centre for the STEM measurements shown in chapter 3 and 4. I'm greatly indebted to Bharat and Susanne, who gave me the possibility to use H-MBE STO samples and to Felix who did the HTEC measurements. Ook ben ik Peter erg dankbaar voor de mogelijkheid om zijn data op LSAT te gebruiken. Die Ergebnisse aus Kapitel 5 wurden vornehmlich in Würzburg und bei DESY erzielt. Vielen Dank für ihre Hilfe, Diskussionen und Interesse. Hiroaki, thanks a lot that I could join you on the MH-CT topic.

Gedurende mijn promotie heb ik vele discussies gevoerd. Speciale dank gaat uit naar de grote LAO-STO Ph.D. clan: Jeroen H., Maarten, Hans, Andreas, Gerwin, Zhicheng, Michelle, Sander en Peter (2x), en het COMAT team: Jeroen B., Hans, Andreas, Joost, Bouwe, Chris, Rik, Brian, Michelle, Nirupam en Wolter. Ik hoop dat we met het COMAT team weer snel een etentje hebben.

In meinem letzten Jahr, habe ich mehrere Monate in EP4 in Würzburg verbracht. Ralph, vielen Dank für Ihre Gastfreundschaft und das Sie mir die Möglichkeit gegeben haben in Ihrer Gruppe zu sein. Monika, Ihre Hilfe hat das Leben in

Würzburg sehr viel einfacher gemacht. Andreas, Andreas, Götz, Michael und Florian, vielen Dank für alle Diskussionen und die Zusammenarbeit im Labor. Und Markus, Sebastian (2x), Philipp, Christian (2x), Björn, Jörg, Ozan, Thomas, Franz, Kai und Christoph, vielen Dank für alle guten Momente.

Met veel verschillende mensen heb ik een kantoor gedeeld, van slechts één week tot zo'n 1,5 jaar. Met jullie allen heb ik zeer plezierige tijd gehad. Alim, Xin, Nirupam, Bouwe, Brian, Hajo, Ronald, Willem, Arjen M., Joska, Andreas (even twice!), Markus en Peter dV, dank! Daarnaast was de technische ondersteuning onmisbaar. Henk, Frank, Dick, Dominique, Gerrit en Arjen, jullie zorgden er voor dat de systemen werkten of werden gemaakt. José, heel erg bedankt voor je snelle laptop actie toen ik in Würzburg zat. Marion, dank voor de ondersteuning bij alle administratieve rompslomp.

Met veel plezier heb ik gewerkt binnen de IMS groep in nauwe samenwerking met ICE/LT, PIN en NanoElectronics. Daarom wil ik ook graag de volgende mensen bedanken: Bernard, André, Anuj, Ole, Matthijn, Minh, Debakantha, Rogier, Alexander, Evert, Gerard, Suresh, Maarten, Ruud, Sjoerd, Werner, Herman, Antony, Manon, Andreski, Kristiaan, Tomasz, Harold, Wilfred, Nicolas, Michiel, Jaap, Oktay, Suresh, Paul, Frank, Mercy, Matjaz, Gerard, Eddy, Hans, Menno, Marcel, Denise, Marieke en Cor.

Behalve onderzoek, waren er de uitjes naast het werk die zorgden voor een gezellige werkomgeving. Mijn eerste grote conferentiebezoek werd gecombineerd met een bezoek aan The Rocky Mountains National Park vergezeld met Gertjan, Mark, Wolter, Maarten, Hajo en Jeroen H.. Met Jeroen B., Joost, Bouwe, Hans en Andreas heb ik onvergetelijke uitjes naar Würzburg en Stuttgart gemaakt. Maar misschien wel het mooiste uitje was december 2010: *Rond de Wiedentocht* is en blijft een toertocht door een prachtig natuurgebied. Gelukkig zijn er een aantal collegae (Wouter, Ruud en Jeroen) net zo gek als ik en wilden ze graag mee wat slagen over het ijs maken. Bedankt voor deze gezellige, geslaagde tripjes.

Buiten het werk heb ik met veel plezier gemusiceerd bij MSO. Dit zorgde voor de aangename afwisseling van de dagelijkse werkzaamheden. Bijzonder dank gaat uit naar de cellosectie; Floris, Sander, Linda, Martine, Frederike en Milou, de cellosectiedates waren altijd zeer geslaagd.

Dank gaat ook uit naar mijn paranimfen, Esther en Joost. Esther, jouw pogingen om te begrijpen wat ik deed en vervolgens uit te leggen aan anderen waren erg bemoedigend. Ik zal ook proberen jouw onderzoek te begrijpen. Joost, wij werden aan het begin van onze promotie aan elkaar gekoppeld. Ik vond het erg leuk om met je samen te werken aan een wel heel frustrerend materiaal, EuO. Samen Thanksgiving vieren in Boston was memorabel.

Tot slot, de continue steun van mijn familie en hun aandacht wanneer ik weer eens mijn onderzoek probeerde uit te leggen was van grote waarde. Hopelijk kan ik aan de hoge verwachtigingen van Sinterklaas voldoen met mijn lekenpraatje. Marjolein, ik vind het echt geweldig dat jij mijn voorkant wilde ontwerpen. Lieve Willem, jij bent mijn grootste ontdekking die ik in Enschede heb gemaakt. Jouw geduld, steun en hulp waren onmisbaar. Ik kan me geen beter persoon bedenken met wie ik het volgende avontuur aan zou willen gaan.